Rice University

Synthesis and Applications of Inorganic/Organic-Polymer Nanocomposites

by

Anubha Goyal

A THESIS SUBMITTED IN PARTIAL FULFILLMENT OF THE

REQUIREMENTS FOR THE DEGREE

DOCTOR OF PHILOSOPHY

Approved, Thesis Committee:

Pulickel M. Ajayan, Committee Chair
Professor, Mechanical Engineering &
Materials Science

Enrique V. Barrera, Professor
Mechanical Engineering &
Materials Science

Stephan Link, Assistant Professor
Chemistry

Houston, Texas

November 2010

ABSTRACT

This research work focuses on developing new synthesis routes to fabricate polymer nanocomposites tailored towards different applications. A simple, one-step method has been devised for synthesizing free-standing, flexible metal nanoparticle-polydimethylsiloxane films. This process simplifies prevalent methods to synthesize nanocomposites, in that here nanoparticles are created *in situ* while curing the polymer. This route circumvents the need for pre-synthesized nanoparticles, external reducing agents and stabilizers, thereby significantly reducing processing time and cost. The resulting nanocomposite also demonstrates enhancement in mechanical and antibacterial properties, with other envisaged applications in biomedical devices and catalysis.

Applying the same mechanism as that used for the formation of bulk metal-siloxane nanocomposites, metal core-siloxane shell nanoparticles and siloxane nanowires were synthesized, with octadecylsilane as the precursor and *in situ* formed metal nanoparticles (gold, silver) as the catalyst. This method offers some unique advantages over the previously existing methods. This is a room temperature route which does not require high temperature refluxing or the use of pre-synthesized nanoparticles. Furthermore, this synthesis process gives a control over the shape of resulting nanocomposite structures (1-D wires or 0-D spherical particles).

High thermal stability of polydimethylsiloxane (PDMS) makes it viable to alternatively synthesize metal nanoparticles in the polymer matrix by thermal decomposition process. This technique is generic across a range of metals (palladium, iron, nickel) and results in nanoparticles with a very narrow size distribution. Membranes

with palladium nanoparticles demonstrate catalytic activity in ethylene hydrogenation reaction.

Additionally, a new nanocomposite electrode has been developed for flexible and light-weight Li-ion batteries. Flexible films were prepared by the integration of the poly(vinylidene fluoride-hexafluoropropylene (PVDF-HFP) polymer electrolyte with the three-dimensional (3D), nanostructured electrode composed of aligned carbon nanotube (CNT)-copper oxide hybrid. This hybrid electrode was fabricated by a combination of chemical vapor deposition and electrodeposition techniques. Embedding it in PVDF polymer results in a flexible system and also renders an external separator redundant. This new design shows an improvement in electrochemical performance over pure CNTs as both CNTs and Cu_2O contribute towards electrochemical activity.

Efforts have also been undertaken towards synthesizing synthetic adhesives by mimicking the design principles found in nature. Aligned patterned CNTs have been used to replicate the fibrillar structure found in geckos' toes which generates adhesion through van der Waals forces. The adhesive forces in CNTs were found to be higher than in geckos and the key to this phenomenon lies in the extensive side-wall contact obtained on compressing CNTs against a surface.

ACKNOWLEDGEMENTS

The doctoral program has been a rich learning experience for me, both professionally and personally, and I am grateful to several individuals who have supported me through my journey.

My success and growth as a researcher are largely due to the mentorship and guidance provided by my advisor, Prof. P.M. Ajayan. In addition to providing invaluable scientific inputs, he gave me freedom and abundant resources to pursue different research ideas that have been instrumental in making this work possible. I also thank the members of my doctoral committee, Prof. Enrique V. Barrera and Prof. Stephan Link for their advice and guidance.

I extend my sincere gratitude to Dr. Angelo Benedetto, Dr. Wenhua Guo, Richard Crouse, Bo Chen and Patrick Johnson from the Shared Equipment Authority for their expert training, technical advice and support that they have provided. I also thank Dr. Peter Loos for several discussions on the theories of XRD and TEM. The funding for this research work came through National Science Foundation Division of Materials Research Grant 0512156.

Gratitude is due to Dr. Ashavani Kumar and Dr. ALM Reddy; this work has benefitted greatly from their expertise. I also thank Dr. Ali Dhinojwala and Liehui Ge from the University of Akron for a fruitful collaboration on synthetic gecko-based adhesives and for several intellectually stimulating and informative discussions on the theories of adhesion. Thanks are due to Prof. Pedro J. J. Alvarez for giving me access to facilities in his laboratory and to Dr. Shaily Mahendra for training me on the protocols of anti-bacterial testing. My collaboration with Prof. Matteo Pasquali and Natnael Behabtu

has given me a deeper understanding on solubilizing CNTs in superacids and I thank them for the opportunity to work with them.

I have had a very fruitful and enjoyable time at Rice University which was made possible by all members of the Ajayan research group and several friends at Rice. My thanks to Arshad Sayyad and to Dr. Robert Vajtai for several useful discussions. I would like to specially mention Gautam Kini for various technical discussions, assistance in revising this thesis and for the constant motivation and encouragement he has provided.

I extend my appreciation to the friendly staff members of the MEMS department, Sherry Vanderslice, Linda Lerma, Alicia Contreras and Lisa Bennett and to the wonderful staff at OISS, Dr. Adria Baker, Vanessa Pena, Cory Owens and Sandra Bloem-Curtis for making my stay at Rice comfortable and memorable. Special credit is due to Dr. Janice Hewitt and Dr. Tracy Volz for their invaluable training and guidance on writing and presentation skills.

Lastly, I sincerely thank my grandparents, parents and my sister, who have provided me unwavering support and encouragement throughout the course of my life. I owe my success in life to their constant faith and support.

TABLE OF CONTENTS

ABSTRACT ii

ACKNOWLEDGEMENTS iv

LIST OF FIGURES x

LIST OF TABLES xvii

NOMENCLATURE xviii

1. Introduction 1

2. Background 4

2.1 Nanocomposites 4

2.2 Metal-Siloxane Bulk Nanocomposites 6

2.2.1 Siloxane Polymers 6

2.2.2 Synthesis Routes 9

2.2.3 Nanocomposite Properties 11

2.3 Metal-Siloxane Hybrid Nanostructures 13

2.3.1 Synthesis: Silane Polymerization to Siloxane 14

2.4 Li-ion Batteries 17

2.4.1 Configuration 20

2.4.2 Anode Material: Carbon Nanotubes 21

2.4.2.1 CNT Synthesis 22

2.4.2.2 CNT Properties 23

3. In situ synthesis of metal nanoparticle-embedded free standing multifunctional PDMS films 25

3.1 Introduction 25

3.2 Materials and Methods 25

3.2.1 Experimental 25

3.2.2 Characterization and Testing 26

3.3 Results and Discussion 28

3.3.1 Gold-PDMS Nanocomposite 28

3.3.2 Platinum-PDMS Nanocomposite 31

3.3.3 Silver-PDMS Nanocomposite 32

3.3.4 Curing Mechanism of PDMS 35

3.3.5 Synthesis Mechanism 37

3.3.6 Mechanical Properties 39

3.3.8 Antibacterial Properties 42

3.4 Conclusions 43

4. In-situ Synthesis of Metal Core-Siloxane Shell Nanoparticles and Siloxane Nanowires 44

4.1 Introduction 44

4.2 Materials and Methods 44

4.3 Results and Discussion 46

4.3.1 Gold Core-Siloxane Shell Nanoparticles 46

4.3.2 Silver Core-Siloxane Shell Nanoparticles 51

4.3.3 Hybrid Nanowires 54

4.3.4 Synthesis Mechanism 57

4.4 Conclusions 61

5. In-situ synthesis of catalytic metal nanoparticle-PDMS membranes by thermal decomposition process 62

5.1 Introduction 62

5.2 Materials and Methods 62

5.3 Results and Discussion 64

5.3.1 Palladium-PDMS Nanocomposite 64

5.3.2 Nickel-PDMS Nanocomposite 68

5.3.3 Iron-PDMS Nanocomposite 70

5.3.4 Catalytic Properties 72

5.4 Conclusions 76

6. Flexible CNT-Cu_2O hybrid electrodes for Li-ion batteries 77

6.1 Introduction 77

6.2 Materials and Methods 78

6.2.1 CNT Synthesis 79

6.2.2 Copper Oxide Electrodeposition 80

6.2.3 Fabrication of CNT-Cu_2O-PVDF electrode-electrolyte 81

6.2.4 Characterization and Testing Techniques 81

6.3 Results and Discussion 82

6.3.1 Characterization 83

6.3.2 Electrochemical Testing 89

6.4 Conclusions 92

7. Conclusions and Future work 93

References.....97

Appendices 133

LIST OF FIGURES

Figure 2.1 Structure of PDMS with the 3-D representation of the siloxane backbone. (Orange: Si, Red: O, Black: C, Blue: H) (Owens MJ, www.dowcorning.com 2005).....8

Figure 2.2 (A) Superhydrophobic siloxane nanofilament and (B) siloxane nanosheets formed using chlorosilanes. The associated graphs show the superhydrophobic nature of these surfaces. (Artus et al. *Advanced Materials* 2006, 18 (20), Ke et al. *Langmuir* 2009 26, (5)). 15

Figure 2.3 (A) SEM image of siloxane nanowires and filaments formed by refluxing gold colloid with alkylsilane. (B) TEM image shows the presence of gold nanoparticle at the tip of the wires. (Prasad et al. *J. American Chemical Society* 2003, 125, (35)) 16

Figure 2.4 SEM images of the wrinkled microspheres formed by refluxing PVP-capped silver nanoparticles with alkylsilane. (Wei et al. *J. Materials Chemistry* 2006, 16, (36)).....16

Figure 2.5 A typical configuration of Li-ion battery. Li-ions shuttle between the two electrodes during the charging (blue) and discharging cycles (red). (GM Ehrlich *Handbook of Batteries*, ed. Linden and Reddy 2002).....20

Figure 2.6 Schematic of a SWCNT. It is composed of sp^2 hybridized carbon in a hexagonal honeycomb lattice. (Ajayan et al. Reports on Progress in Physics, 1997, 60).....21

Figure 2.7 HRTEM image of a MWCNT showing the multiple layers. The interlayer distance is 0.34nm. (Ajayan et al. Reports on Progress in Physics, 1997, 60).....22

Figure 3.1 (A) Photograph of pure PDMS and Au-PDMS film showing the color change to ruby-red after the formation of nanoparticles. (B) UV spectra of the films. Pure PDMS shows no absorbance but Au-PDMS film absorbs at 530 nm.....29

Figure 3.2 TEM images of the gold nanoparticles formed in the PDMS matrix. Inset is their diffraction pattern which indicates the fcc crystalline nature.....30

Figure 3.3 Optical images of Au-PDMS film showing the homogenous spatial distribution of nanoparticles in the polymer matrix. 31

Figure 3.4 (A) and (B) TEM images of the platinum nanoparticles. Inset (A) Photograph of Pt-PDMS film and (B) Diffraction pattern of crystalline platinum nanoparticles.....32

Figure 3.5 (A) UV-Vis spectra of PDMS and Ag-PDMS film. Silver nanoparticles show an absorbance at ~ 415nm. Inset is the photograph of Ag-PDMS film which is yellowish-brown in color due to the presence of silver nanoparticles.....33

Figure 3.6 (A) and (B) TEM images of the silver nanoparticles formed in the PDMS matrix. Inset is the diffraction pattern obtained from crystalline fcc silver nanoparticles.....34

Figure 3.7 Particle size distribution of silver nanoparticles.....34

Figure 3.8 XPS spectra of Ag-PDMS film showing the binding energy of Ag3d and Si2p core levels.....35

Figure 3.9 Curing mechanism of PDMS. It involves platinum-catalyzed hydrosilylation reaction across the vinyl groups of the oligomer.[25].....36

Figure 3.10 (A) Photographs of vials containing (1) pure curing agent (2) silver benzoate solution with curing agent and (3) silver benzoate with pure elastomer. The color difference between vials 2 and 3 indicates that the nanoparticle reduction takes place only with curing agent. No reduction is observed with pure elastomer (B) FTIR spectra of solutions (1) and (2). Si-H groups are consumed during the nanoparticle synthesis causing a decrease in peak intensity.....38

Figure 3.11 (A) Comparison of stress-strain curves of pure PDMS and Ag-PDMS. Silver nanoparticles increase the mechanical strength by three times. (B) Tangent delta vs. frequency curves for PDMS and Ag-PDMS films. There is no significant change in damping properties. Inset is the comparison of their storage moduli.....40

Figure 4.1 (A) UV-Vis spectra of pure octadecylsilane and gold-siloxane nanoparticle solution in pentanone. A characteristic gold nanoparticle peak can be seen at ~ 577 nm. (B) XRD pattern of the nanoparticles showing peaks from fcc crystalline gold.....47

Figure 4.2 (A) and (B) SEM images of gold-siloxane nanoparticles. (C) High magnification TEM image revealing their spherical core-shell structure. 49

Figure 4.3 (A) Diameter distribution of the nanoparticles (B) EDS spectrum obtained from the nanoparticles confirming the presence of both gold and silicon. 50

Figure 4.4 (A) and (B) SEM images of the silver-siloxane nanoparticles. (C) Particle size distribution of the nanoparticles. 52

Figure 4.5 (A) UV-Vis spectrum of silver nanoparticles. The peak at 420 nm originates from the surface-plasmon resonance of the nanoparticles (B) EDS spectrum of the nanoparticles showing the presence of both silicon and silver. 53

Figure 4.6 XRD pattern of the nanoparticles corresponding to crystalline fcc silver 54

Figure 4.7 (A) and (B) SEM images showing micron-long, irregular and helical nanowires. 55

Figure 4.8 Diameter distribution of the nanowires. 55

Figure 4.9 (A) Back-scattered SEM image and (B) TEM image of the nanowires revealing the presence of gold nanoparticles at their tips. 56

Figure 4.10 Controlled experiment showing the formation of a thick siloxane layer with pure ODS in the absence of metal salt. 57

Figure 4.11 XPS spectra of the nanoparticles showing the binding energies of (A) Au4f and (B) Si2p core levels. The peak positions indicate that gold is present in metallic state. The fitting of Si2p spectrum reveals siloxane to be the major component. 58

Figure 4.12 FTIR spectra obtained from pure ODS and the nanoparticles indicating the transformation of Si-H and Si-OH groups in ODS to Si-O-Si after the reaction. 59

Figure 4.13 Schematic of the synthesis mechanism. 60

Figure 5.1 Photograph of pure transparent PDMS film, Pd-PDMS film before heating and Pd-PDMS film after heating with evident color changes. 64

Figure 5.2 TEM images of palladium nanoparticles formed in the PDMS matrix.....66

Figure 5.3 Size distribution obtained using TEM micrographs of palladium nanoparticles. 66

Figure 5.4 XRD pattern confirming the formation of crystalline fcc palladium nanoparticles. 67

Figure 5.5 XPS spectra showing the binding energies of (A) Pd3d and (B) Si2p core levels. The peak positions in Pd spectrum correspond to that of its metallic state. 68

Figure 5.6 Photograph of Ni-PDMS film before and after the heat treatment. The color changes on the formation of nickel nanoparticles. 69

Figure 5.7 TEM images of nickel nanoparticles formed in the PDMS matrix. 69

Figure 5.8 EDS spectrum confirming the presence of nickel. 70

Figure 5.9 Photograph of Fe-PDMS film before and after the heat treatment. The color change indicates the formation of iron nanoparticles.....71

Figure 5.10 TEM images of iron nanoparticles formed in the PDMS matrix. 71

Figure 5.11 EDS spectrum confirming the presence of iron. 72

Figure 5.12 TGA measurement of PDMS membrane containing 2 wt% palladium. The degradation starts at about 400°C.....74

Figure 5.13 Schematic of the catalytic experiment set-up. (Courtesy: Robert Remias) 74

Figure 5.14 TOR and Activation energy of ethylene on (A) 1% Pd-PDMS and (B) 2% Pd-PDMS. 75

Figure 6.1 Fabrication schematic for Cu_2O coated CNT electrodes. The CVD-grown CNTs were coated with copper oxide using electrodeposition. After polymer infiltration, the CNTs were peeled off the substrate to obtain free-standing electrodes on which a thin layer of gold was sputter-coated. 79

Figure 6.2 Photograph of the three electrode instrumental set-up used for electrodeposition.....80

Figure 6.3 Current vs. Time curve for the cathodic deposition of Cu_2O. 81

Figure 6.4 The custom-fabricated Swagelok-type cell for battery testing. 82

Figure 6.5 (A) and (B) SEM images of as-grown aligned CNTs. (C) and (D) HRTEM images confirming the multi-wall nature of the tubes. 84

Figure 6.6 (A) and (B) SEM images of copper oxide coated CNTs. The inset shows a good conformal coverage of copper oxide on CNTs. 85

Figure 6.7 EDS spectrum obtained from coated CNTs after electrodeposition that confirms the presence of copper on CNTs. The weak iron signal is from the iron catalyst used for CNT growth. 86

Figure 6.8 XRD pattern obtained from Cu_2O-CNT hybrids showing the crystalline nature of Cu_2O coating. Peaks at 2Θ values of 44°, 50.9° & 74.7° originate from the steel substrate used for CNT growth. 87

Figure 6.9 XPS spectrum of Cu_2O-CNT hybrid. The peak positions establish the presence of copper as Cu_2O.....87

Figure 6.10 (A) Photographs of pure CNTs and CNTs after polymer infiltration. (B) SEM image revealing the porous nature of the PVDF-HFP-SiO_2 film after phase inversion (C) The photograph emphasizing the good flexibility of the peeled films. 89

Figure 6.11 Charge-discharge voltage profiles of (A) pure CNTs and (B) CNT-Cu_2O hybrid between 0.02 and 3V vs Li/Li^+ 91

Figure 6.12 Comparison of the electrochemical performance of pure CNTs and CNT-Cu_2O hybrids. The hybrid shows a two times better capacity as compared to pure CNTs.....92

Figure 7.1 SEM images of SnS coated CNTs.....96

Figure 7.2 XRD spectrum confirming the formation of crystalline orthorhombic SnS ...96

LIST OF TABLES

Table 3.1 Percentage Degree of Swelling. Pure PDMS films have a better tolerance to organic solvents as compared to Ag-PDMS films.....41

Table 3.2 Confirmation of antibacterial activity of Ag-PDMS towards *E. coli* and *B. subtilis*. Statistically significant decrease in the number of colony forming units (cfu) of both the strains in the presence of Ag-PDMS indicates its antibacterial activity. 42

NOMENCLATURE

PDMS	Polydimethylsiloxane
ODS	Octadecylsilane
PVDF-HFP	Poly(vinylidene fluoride-hexafluoropropylene)
CNT	Carbon Nanotube
TEM	Transmission Electron Microscopy
SEM	Scanning Electron Microscopy
EDS	Energy Dispersive X-Ray Spectroscopy
XRD	X-Ray Diffraction
XPS	X-Ray Photoelectron Spectroscopy
FTIR	Fourier Transform Infrared Spectroscopy
TGA	Thermogravimetric Analysis
CVD	Chemical Vapor Deposition

Chapter 1

Introduction

The field of nanocomposites has drawn attention of researchers across various disciplines. This wide-spread interest stems from the multi-phasic nature of nanocomposites wherein, myriad properties can be incorporated in a single system, a combination not usually possible to attain through conventional materials. One or more of the phases in a nanocomposite has dimensions below 100nm, a feature which significantly assists in obtaining many novel material properties. Nanocomposites provide unique flexibility in tailoring properties of materials and offer unmatched freedom in the design of new materials, thereby opening avenues to synthesize advanced materials.[1] The choice of the constituent phases and their synergistic interactions help attain a key material characteristic – that of multi-functionality. On account of these several advantages offered by nanocomposites, there has been sustained interest in the development of new routes to synthesize novel composite variants.

This dissertation focuses on (i) formulating simple processing routes to synthesize nanocomposites along with identifying the underlying reaction mechanism(s) (ii) characterizing the physical and chemical properties of the resulting nanocomposites, and (iii) exploring applications of custom synthesized nanocomposites as antibacterial membranes, catalytic membrane reactors and as new generation battery electrodes. Nanocomposites that have been successfully synthesized include metal nanoparticle-embedded polydimethylsiloxane (PDMS) polymer matrices, metal-siloxane

nanostructures, and carbon nanotube (CNT)-metal oxide hybrids embedded in poly(vinylidene fluoride-hexafluoropropylene) (PVDF-HFP) polymer.

This thesis is organized in 7 chapters. Chapters 1 and 2 provide pertinent introduction and background on nanocomposites. Chapters 3 and 4 discuss new synthesis strategies developed for in-situ formation of metal nanoparticle-PDMS bulk composites and metal-siloxane nanostructures respectively. Chapter 3 elucidates methods used in characterizing enhancements in physicochemical properties of metal-polymer matrices and prevalent reaction mechanisms that result in these materials. A range of nanoparticles (gold, silver and platinum) were synthesized in the PDMS matrix; silver-PDMS composite was evaluated for mechanical properties and antibacterial efficacy. When compared to pure PDMS, the composite demonstrated improvements in both properties. Chapter 4 discusses controlled synthesis of metal core-siloxane shell nanoparticles or nanowires, using in-situ synthesized gold and silver nanoparticles as the catalyst.

In Chapter 5, an alternative approach is proposed for in-situ formation of metal nanoparticle-PDMS composites. Transition metal nanoparticles (palladium, iron and nickel) were synthesized in the polymer matrix by the thermal decomposition process. Also demonstrated is the enhancement in catalytic activity of palladium-PDMS membranes through a test case of the ethylene hydrogenation reaction.

Chapter 6 explores applications of advanced nanocomposites in the field of energy storage. A co-axial CNT-copper oxide composite anode was designed for Li-ion batteries. This anode was subsequently incorporated into a porous PVDF-HFP-SiO_2 matrix to obtain a flexible, free-standing electrode. The light-weight composite anode showed enhanced electrochemical capacities when compared with pure CNTs. Finally

Chapter 7, summarizes the results of this dissertation and recommends directions for future research.

The appendix section discusses bio-inspired synthetic adhesives fabricated using patterned CNTs which are based on the design principles of hierarchical architecture found in geckos. The CNTs tape shows a better adhesion than gecko and this adhesion was found to increase with preload due to an increase in side-wall contact.

Chapter 2

Background

2.1 Nanocomposites

Nanocomposites are multiphase materials with at least one constituent phase in the nanoscale i.e. having dimension of 100 nm or lower.[1] The presence of multiple phases in a single system and their synergistic effects endows the resulting nanocomposites with new and improved properties. It also equips the nanocomposites with multi-functionality, a highly desired feature in materials. The stimulus for the study of nanocomposites therefore stems from the possibility of achieving advanced properties that are unattainable through conventional materials and from the freedom to tailor the properties by manipulation of the constituent phases. The resultant properties of nanocomposites are governed by the composition, physical and chemical characteristics of the constituents and their mutual interactions. There is an active interest in controlling these factors to design and synthesize nanocomposites at various length scales, aimed towards a diverse range of applications.

This thesis is focused in particular on polymer nanocomposites as they have attracted significant attention by enabling technological developments across diverse areas such as biosensors,[2] optical devices,[3] micromechanical devices[4] and advanced catalytic membranes.[5] Based on the dimensions of the nanoscale phase, polymer nanocomposites can be categorized as zero-dimensional (eg nanoparticles), one-dimensional (eg carbon nanotubes) and two dimensional (eg clay). The presence of these inclusions can bring forth changes in several polymer properties. For example, mechanical and thermal properties of polymer matrices have been enhanced by

encapsulating various fillers like carbon nanotubes, clay or graphene.[6-11] In a similar manner, catalytic and optical features have been introduced in an otherwise inactive polydimethylsiloxane polymer matrix by incorporating palladium and gold nanoparticles respectively.[12, 13] Metal nanoparticles, in particular, have been highly instrumental in influencing nanocomposite properties and thus constitute an important class of fillers.

Metal nanoparticles are known to exhibit size-dependent physical and chemical properties which are significantly different from those of their bulk counterpart.[14-16] This makes metal nanoparticles highly desirable for a broad range of applications such as catalysis, gas-sensing, drug-delivery, optics and microelectronics.[17-21] A steep challenge in realizing size-dependent properties of nanoparticles for applications is in preventing their natural tendency to aggregate/degrade on account of an intrinsically high surface energy of the nanoparticle surface. Loss in nanoscale properties occurs from an increase in effective size of the nanoparticle from aggregation or through a change in the material property, when surface degradation takes place through pathways such as oxidation. As a method to lower nanoparticle surface energy, surface stabilizing molecules such as surfactants and ligands have been used that safeguard the nanoparticles from aggregating/degrading. Another alternative approach involves the incorporation of nanoparticles in a continuous polymer matrix or shell which also extends their point-of-use applications.

In addition to safeguarding nanoparticle properties, the polymer can serve multiple functions. It alters surface charge, reactivity and functionality, thus imparting additional properties to the nanoparticles.[17-19] For example, the presence of polymer shells have been shown to reduce toxicity of the metal core, thus resulting in

biocompatible material.[22, 23] Surface modifications can also protect the core from detrimental physical and chemical effects of the environment such as oxidation and moisture. Nanoparticles also introduce additional properties in the polymer matrix. Motivated by these advantages, diverse polymers have been explored towards forming nanocomposite with siloxane polymers (particularly polydimethylsiloxane) emerging as a popular candidate. Thus, extensive efforts have gone into developing synthesis routes for metal-siloxane nanocomposites and that is also an important focus area of this thesis.

2.2 Metal-Siloxane Bulk Nanocomposites

The following section provides a brief overview on siloxane polymers, the various synthesis schemes used for siloxane nanocomposites and documents the mechanical properties of these nanocomposites.

2.2.1 Siloxane Polymers

Polydimethylsiloxane (PDMS) belongs to the family of siloxane polymers. Historically, this class of polymers was discovered in 1901 by Frederic Stanley Kipping who coined the name "silicones" considering them (incorrectly) to be analogues of carbonaceous ketones.[24] In later years, advancements in characterization techniques revealed silicones to have a Si-O-Si linkage and thus, the polymer family was renamed "polysiloxanes" (or siloxanes).

The discovery of silicones opened a fascinating field of materials at the interface of organic and inorganic chemistry.[25] Silicones have a Si-O-Si backbone to which, different organic groups can be attached through Si-C linkage giving silicones the general formula $[–OSiR'R–]_n$ (where R and R' refer to the organic side groups and "n" is an

integer denoting the number of repeating units). The presence of both the organic and inorganic components in a single molecule gives silicones unique properties.[25] The Si-O bond renders silicones to be a highly flexible material because of its long bond length (1.63 Å) and large bond angle (130°) that allows for easy changes in conformation. In addition, silicones are non-toxic, chemically inert and gas permeable. Silicones have other highly desirable properties such as electrical and temperature insulation. Thus, they can be used in applications such as lubrication and defoaming agents, where most organic materials would either melt or decompose.[25] A low surface tension makes them useful as mold-release agents, anti-fouling materials, fiber lubricants and water repellants. The low heat of vaporization and smooth texture of silicone fluids make them excellent base ingredients to build cosmetic products. The physical and chemical properties of silicones depend on the number of repeating units in the polymer chain and the degree of cross-linking. Depending on these factors, silicones can exist in various forms such as elastomers, fluids, emulsions, compounds, lubricants and resin.

The most widely used silicone polymer is polydimethylsiloxane (PDMS) which has two methyl groups attached to each silicon atom (Figure 2.1). PDMS is manufactured by reaction between silicon and methyl chloride at temperatures of 250-350°C and pressures of 1-5 bars.[25] This reaction yields a mixture of methyl chlorosilanes. For obtaining PDMS, dimethyldichlorosilane is hydrolyzed, followed by polymerization of the oligomers obtained on hydrolysis.

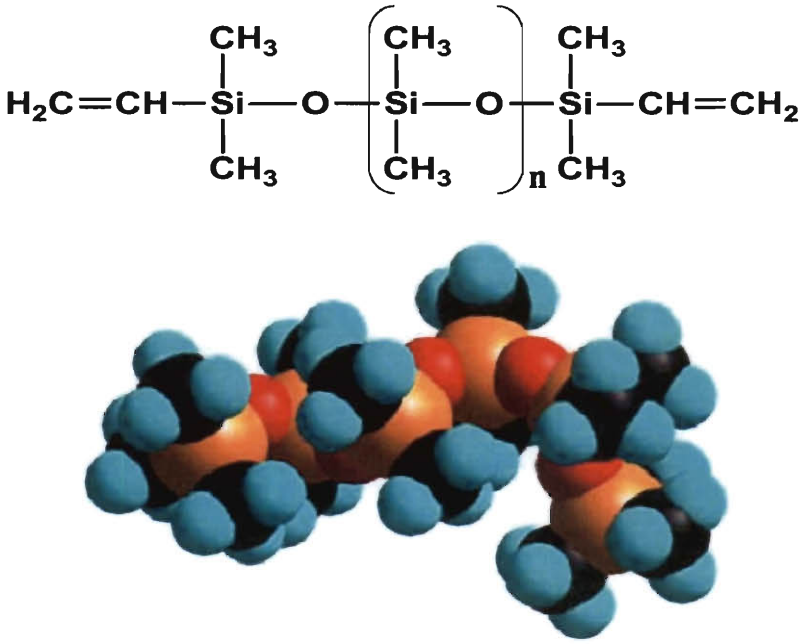

Figure 2.1 Structure of PDMS with the 3-D representation of the siloxane backbone. (Orange: Si, Red: O, Black: C, Blue: H) (Owens MJ, www.dowcorning.com 2005)

All the findings reported in this thesis are based upon a commercially available PDMS which is marketed under the brand name "Sylgard 184" from Dow Corning and is available as a two component kit. The kit contains the base elastomer (a vinyl termintated high molecular weight oligomer) and the companion curing agent which is constituted of a mixture of a platinum complex and copolymers of methylhydrosiloxane and dimethylsiloxane. Sylgard 184 PDMS has a large thermal stability range and a high dielectric constant (2.65 at 100 Hz).[25] It has a dynamic viscosity of 3900 centipoise and a long working time of up to two hours. These properties along with its flexibility, transparency, chemical inertness and gas permeability have made PDMS, the undisputed driver behind soft lithography which in turn has been instrumental in creating the fields of micro and optofluidics.[26, 27]

In spite of its wide use and attractive properties, PDMS has some inherent drawbacks such as poor mechanical properties, low tensile strength and intolerance to organic solvents.[28] A high surface inertness also restricts certain biological applications in microfluidic chips, since it is difficult to immobilize bio-molecules onto its surface.[29] Addition of metal nanoparticles to the PDMS polymer matrix can aid in overcoming some of these drawbacks. For example, Lou et al. successfully detected protein immunoassay in a microfludic device by using the antigen coated gold nanoparticles.[30] In other reports, PDMS films with metal nanoparticles were used to make optical and thermochromic devices, surface-enhanced Raman substrates and were also used in other multi-functional applications such as catalysis and gas separation.[5, 31] Motivated by such diverse applications possible through nanocomposites, numerous efforts have been directed towards developing novel synthesis strategies. But there are some limitations associated with these existing methods and this has acted as a motivation behind this research work.

2.2.2 Synthesis Routes

In synthesizing metal-PDMS nanocomposites, popular approaches include incorporating pre-made nanoparticles into a PDMS matrix with the use of a common blending solvent or reducing metal salts dispersed in PDMS by an external reducing agent to result in nanoparticles.[32, 33] However, these approaches involve two or more processing steps and require either an external reducing agent or pre-synthesized nanoparticles. As a result, these methods lead to an increased processing time and cost which makes them economically unfeasible. To illustrate the point, Mendes et al. synthesized PDMS membranes containing palladium nanoparticles by mixing palladium

acetate with PDMS in THF solvent and reducing the metal salt with $NaBH_4$.[12] While the use of expensive pre-synthesized palladium nanoparticles was avoided, the use of a reducing agent was necessary. Pre-synthesized nanoparticles have often been embedded into polymers to circumvent the requirement of external reducing agents. For this, physical and chemical vapor deposition, ion-implantation and sol-gel synthesis routes have been employed.[34-37] Other alternative techniques have also been explored to synthesize PDMS nanocomposites. Gao and co-workers have reported chitosan, a biopolymer assisted gold nanoparticle deposition on PDMS surfaces.[38] Chen and co-workers synthesized gold nanoparticle-PDMS composite films by immersing cured PDMS films in gold chloride solution and used it for enzyme immobilization and as a chemical reactor.[29] However, these synthesis methods involve multiple steps and the nanoparticle concentration is localized to the surface only. Thermal decomposition of metal salts is a popular synthesis method to get bulk dispersion, wherein a mixture of metal precursor and polymer is heated to the decomposition temperature of the salt, resulting in the formation of metal nanoparticles in a polymer matrix.[39-41] Various metal salts have been used such as oxalates, carbonyls, alkoxides, acetates and formiates have been used with this technique. For example, Rutnakornpituk et al. synthesized cobalt nanoparticles by thermal decomposition of cobalt carbonyls in the presence of polysiloxane block copolymers as a steric stabilizer.[42]

Though most of the above discussed techniques are well-explored, there are some process limitations which dictate the choice of the synthesis routes. Chemical intolerance of PDMS to the solvent used and interference with its ability to polymerize in the presence of a metal precursor present major challenges.[43] Additionally, metal loading in

the polymer matrix is governed by the solubility of metal-precursors in the polymer and also by the solubility of both components in the common solvent. PDMS is insoluble in polar solvents which is a common category of solvent for dissolving many metal salts. The physical properties of the polymer such its melting point and glass transition temperature can add further constraints. Furthermore, the curing process of PDMS is inhibited in the presence of chemicals such as sulfur, amines and amides. These process limitations call for the development of new synthesis routes for PDMS nanocomposites. There has been sustained effort towards this end with the desire to obtain enhanced and advanced properties from the resulting nanocomposite.

2.2.3 Nanocomposite Properties

The studies reported in this thesis have shown enhancements in the mechanical, anti-bacterial and catalytic properties of PDMS on introducing metal nanoparticles in the polymer membranes. Because PDMS intrinsically is a weak polymer, incorporating nanoparticles in a polymer matrix could improve its mechanical properties.[44] The effect of nanosized inclusions on the mechanical properties of polymer matrices have been studied in detail. Mechanical properties of the nanocomposite are dependent on the shape, size and distribution of the filler. The properties of fillers plays a significant role in affecting mechanical properties through filler-filler interactions and filler-matrix interactions.[45] The latter interactions can be tuned by controlling surface characteristics of the filler and the functional groups present on its surface. For effective reinforcement, the filler needs to be homogeneously dispersed in the matrix and must not be aggregated. High surface energy fillers like nanoparticles are expected to have good adhesion with the PDMS matrix. This has been tested extensively and found to be true across various

fillers including both organic and inorganic type.

Recently, Ci *et al.* improved the mechanical properties of PDMS by dispersing carbon nanotubes in the polymer.[7] They found that the longitudinal modulus and damping capability of carbon nanotube reinforced PDMS matrices improved by an order of magnitude over pure PDMS. Inorganic materials such as Al_2O_3, $CaCO_3$ and SiO_2 have also been used as fillers in PDMS polymer.[46-48] $CaCO_3$-PDMS composites containing filler particles of different size distribution were tested for mechanical properties under tensile and oscillatory bending stresses.[47] Both the storage and the loss moduli were found to increase with the filler loading. Silica particles are known to enhance the mechanical properties of PDMS through hydrogen bonding between the silanol group on the silica surface and the oxygen atoms of PDMS which ensures a good bonding at the interface. Chen and co-workers have introduced superhydrophobic nanosilica in PDMS matrix and tested the matrix for the tensile and dynamic mechanical properties. They obtained a better performance from the nanocomposite as compared to pure polymer matrix.[49] Besides these, layered fillers such as clay or porous fillers like zeolites have also proven to be very effective as reinforcing agents for polymer matrices.[50, 51]

PDMS is a widely studied polymer for catalytic reactions as it has good diffusivity for gases besides the before-mentioned attributes of good chemical and mechanical properties.[12] The dense PDMS membranes can be made catalytically active to serve the dual purpose of separation and reaction in a single step.[52] As an example, Kopinke and co-workers have synthesized non-porous, thin (3-7μm) PDMS membranes containing palladium nanoparticles supported on titania and silica.[19] These membranes are effective for hydrodechlorination of organic chlorobenzene contaminant present in

ground water. In another study based on a similar system, PDMS membranes with 9 nm palladium nanoparticles, synthesized by chemical reduction, were used for propylene hydrogenation.[53]

2.3 Metal-Siloxane Hybrid Nanostructures

In previously discussed siloxane metal nanocompsites, the resulting structures were metal nanoparticles dispersed in a continuum siloxane polymer matrix. Beyond nanocomposites, it is also possible to synthesize hybrid metal-polymer structures of the core-shell and nanowire varieties, a new route for which has been discussed as a part of this thesis. In such hybrid structures, nanoparticles exist as discrete entitites where the polymer ceases to exist as a continuum. In core-shell structures, metal nanoparticles comprise the core and are encapsulated by a polymer shell. These core-shell structures can serve as building blocks to form higher ordered structures that have greater complexity to their architecture. Core-shell structures open up the possibility to tailor material so that the physical and chemical properties can be controlled. Applications of these structures have been demonstrated in a wide breadth of fields such as of photonics,[54] catalysis[55] and drug-delivery.[56]

Various routes have been developed to synthesize metal-polymer nanostructures in desired shape, size and morphology. Some of the techniques include adsorption of the monomer on the core particle followed by polymerization,[57] emulsion polymerization,[58] sol-gel,[59] layer-by-layer deposition[60] and direct attachment of functionalized polymers to the surface of nanoparticles.[61] The technique of adsorbing monomer followed by its polymerization is widely used. The polymerization reaction can be catalyzed by an external initiator, or by the core if catalytically active.[57] Using another popular approach

of sol-gel, silica coatings were formed on the surface of vitreophillic gold nanoparticles by the hydrolysis and condensation of tetraethoxysilane (TEOS).[59] An alternative route which has been used in this research work to achieve siloxane shells on metal nanoparticles involves the use of silane precursors which convert to siloxanes on hydrolysis and subsequent polymerization.

2.3.1 Synthesis: Silane Polymerization to Siloxane

Silanes with a general formula $Si_nH_{(2n+2)}$ are silicon analogues of alkane hydrocarbons. Silanes, particularly those with chloride or alkoxide groups, hydrolyze easily to form silanols. Silanols undergo polycondensation reactions to form siloxanes.[62,63] The polycondensation scheme has been widely used to form superhydrophobic siloxane coatings. Seeger and co-workers synthesized siloxane nanofilaments by polycondensation of trichloromethylsilane (CH_3SiCl_3) and water in gas phase through chemical vapor deposition (CVD).[62] Further, they measured high contact angles of water on a substrate coated with siloxane filaments, thus demonstrating the preparation of a superhydrophobic surface (Figure 2.2(A)). The contact angle along the water phase was seen to remain consistently high across a wide range of pH and over several days. In another study, Li and co-workers assembled nanosheets of octadecylsiloxane using octadecyltrichlorosilane as the starting material (Figure 2.2(B)).[64] The resulting ensemble was also superhydrophobic and demonstrated changes in contact and sliding angle with a variation in relative humidity. It is worth mentioning that preparation of superhydrophobic substrates requires intrinsic hydrophobicity of the constituent material (offered by siloxanes) in conjunction with surface roughness (rendered by its form as nanowires). In another application, trimethoxysilane was used to

form siloxane coatings on gold nanoparticles and stabilize them for surface-enhanced Raman spectroscopy (SERS) studies.[63]

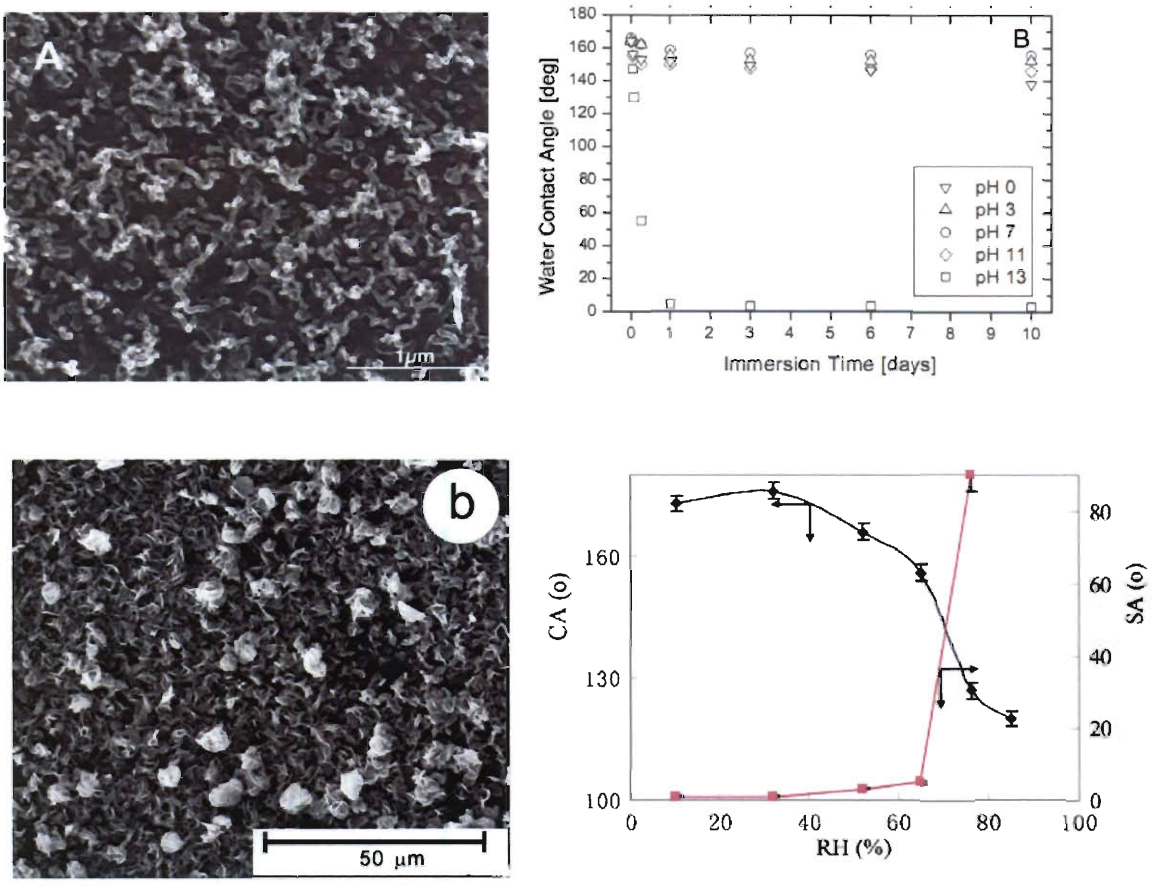

Figure 2.2 (A) Superhydrophobic siloxane nanofilament and (B) siloxane nanosheets formed using chlorosilanes. The associated graphs show the superhydrophobic nature of these surfaces. (Artus et al. *Advanced Materials* 2006, 18 (20), Ke et al. *Langmuir* 2009 26, (5)).

Beyond nanosheets and filaments, other hybrid siloxane structures have also been synthesized. Prasad et al. synthesized nanowires, tubes and filaments of siloxane during the digestive ripening process to prepare gold nanoparticles stabilized by octadecylsilane ($C_{18}H_{37}SiH_3$, ODS).[65] Interestingly, the various forms of siloxane nanostructures were a serendipitous outcome of the aqueous medium in which digestive ripening was carried

out. It was rationalized that the presence of water was responsible for polycondensation of ODS to form the myriad siloxane nanostructures (Figure 2.3). These nanostructures were amorphous and could be easily isolated in powder form. Adopting a similar methodology, Yang et al. formed spherical microstructures (diameter up to 200 μm) using PVP-capped silver nanoparticles as a catalyst.[66] As can be seen in Figure 2.4 these microspheres have a wrinkled or fibrous surface topography.

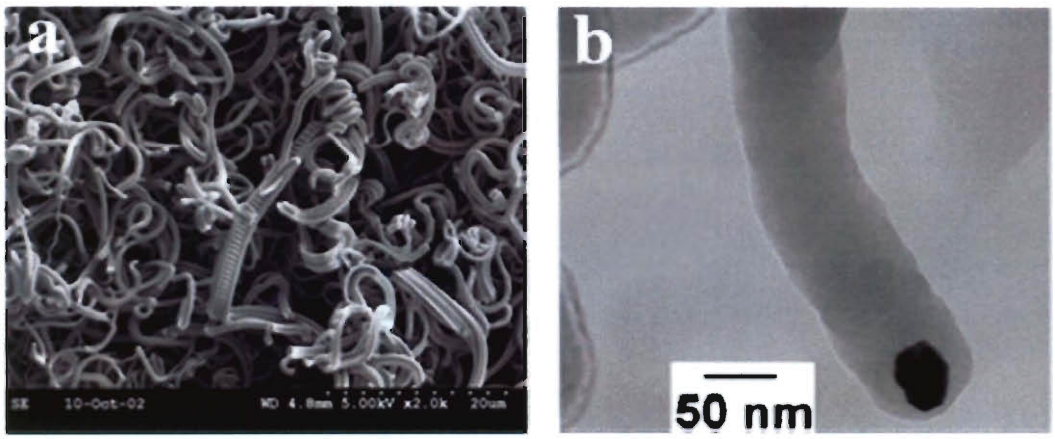

Figure 2.3 (A) SEM image of siloxane nanowires and filaments formed by refluxing gold colloid with alkylsilane. (B) TEM image shows the presence of gold nanoparticle at the tip of the wires. (Prasad et al. *J. American Chemical Society* 2003, 125, (35))

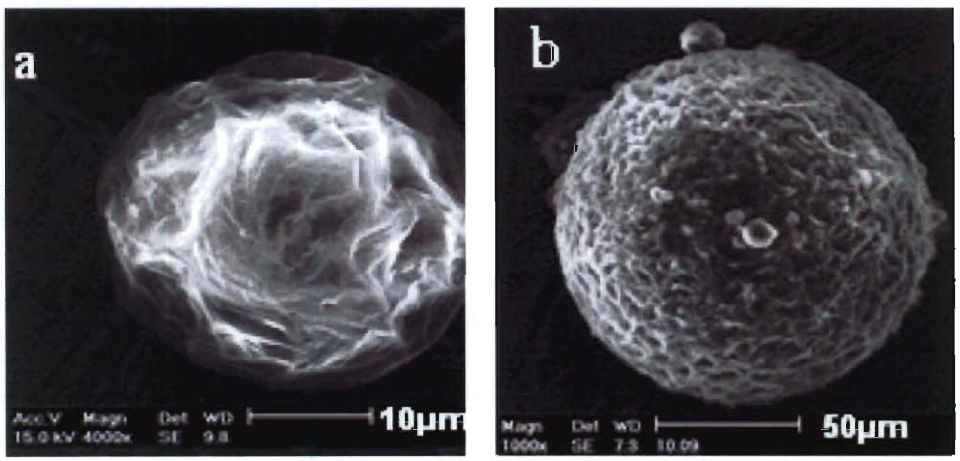

Figure 2.4 SEM images of the wrinkled microspheres formed by refluxing PVP-capped silver nanoparticles with alkylsilane. (Wei et al. *J. Materials Chemistry* 2006, 16, (36))

The scheme used by Prasad et al. and Yang et al. suffers from certain drawbacks. The most prominent is the use of pre-synthesized nanoparticles as a catalyst which adds to the processing cost and time. This route also requires high temperature from a refluxing step, further adding to processing cost. Further, both reports did not show control over the shape and topography of the resulting structures. There is limited available literature on the formation of other nanostructures such as siloxane nanowires by silane polymerization. Using this synthesis scheme, Prasad et al. have shown the nanowire synthesis through solution processing[65] while Artus et al. have formed siloxane nanofilaments in the gas-phase.[62] Chapter 4 of this thesis reports a new room temperature synthesis method based on silane reduction and polymerization, which offers flexibility in obtaining core-shell structures and nanowires. This method also overcomes several of the limitations that constrain the existing methods, particularly those involving high temperature requirements and the use of pre-synthesized nanoparticles.

2.4 Li-ion Batteries

Besides the conventional applications, nanocomposites also find use in the advanced area of electrochemical storage. In Chapter 6, a free-standing flexible nanocomposite composed of hybrid CNT-Cu_2O structures embedded in a polymer matrix has been explored as an anode material for Li-ion batteries. This novel design makes use of the unique 1-dimensional geometry of CNTs and the 3-dimensional scaffold provided by them for the integration of other materials.

Lithium ion batteries command a major presence among all rechargeable battery systems, owing to their higher energy density and a better efficiency and battery life as compared to other alternatives.[67] There have been constant efforts towards further

improving the performance and life of these batteries. Concurrently, research attempts have also been directed towards developing thin, flexible and light-weight batteries.[67-69] These endeavors are stimulated by a growing societal demand for portable and miniaturized electronics. A successful and commercially viable solution would require both structural and compositional changes in the existing battery technology.

Reviewing the historical developments, the pioneering work for lithium batteries was undertaken by American chemist Gilbert Newton Lewis in 1912. But the first commercial demonstration was possible only in the 1970s when Sony introduced the primary, non-rechargeable Li cells.[70] Later, Exxon proposed a new configuration for rechargeable batteries which involved a Li metal anode (negative electrode), TiS_2 cathode (positive electrode) and lithium perchlorate in dioxolane as the electrolyte.[71] The layered chalocegenide TiS_2 was efficient for a fast Li diffusion, but the instability of metallic lithium posed a major safety issue, especially during charging. Lithium reacted with the electrolyte solution resulting in the formation of a passivating layer of lithium alkyl carbonates which subsequently led to the deposition of insulating dendrites on the electrode. This problem could be solved by using an alloy of Li with aluminum, but the alloy was plagued with limited cycling capacity due to large volume changes.[72] These failed attempts shifted the research focus towards rechargeable batteries based on Li-ion, which were safe to use though they were slightly lower in energy density as compared to Li metal batteries.

The first commercial Li-ion battery was released by Sony in 1991. It was based on John Goodenough's seminal work in which he proposed the new family of layered cathode materials spinels Li_xMO_2 (where M is Co, Ni or Mn).[73, 74] The groundbreaking

stage in battery technology came with the advent of 'rocking chair' or 'swing' technology. This scheme uses Li insertion materials as electrodes, thereby eliminating the use of hazardous lithium metal. During the charging and discharging, Li-ion intercalates and de-intercalates into the anode and the cathode. The cell voltage originates from the free energy difference between Li ion when it is intercalated in the crystal structures of the two electrode materials. Based on this technology, Sony devised rechargeable batteries with a carbon anode and the layered hexagonal $LiCoO_2$ anode, which continues to be the most prevalent configuration to date for use in laptops, camcorders, cell phones and other portable electronics.[75] These batteries are equipped with an excellent cycle life (1000 cycles), a higher average operating voltage and energy density than that of nickel-cadmium batteries and have an intrinsically high level of safety.

The next significant advancement came in the form of Li solid polymer electrolyte (Li-SPE) battery in which the liquid electrolyte was replaced by a dry polymer.[76] These batteries are devoid of any organic electrolyte and the polymer itself assists in the movement of Li ion, but the operating temperatures are high, up to 80°C which poses a severe limitation. The other feasible and more popular variant is the gel-polymer electrolyte battery, which has also been used in Chapter 6, where the liquid electrolyte is entrapped in the polymer matrix. In the successful demonstration of this concept, Bellcore Laboratories fabricated batteries using PVDF-HFP polymer (copolymer of vinylidene difluoride with hexafluoropropylene) swollen with a liquid electrolyte.[77] In a further modification of the process, fillers and plasticizers were added to the polymer to form membranes which are mechanically stronger and are better ionic conductors, thereby helping in designing better batteries.[78-80]

2.4.1 Configuration

The fundamental design of a Li-ion battery incorporates the two electrodes (anode and cathode), the electrolyte, separator and the current collector. The system operates by shuttling of the Li ions between the electrodes during alternate charge and discharge cycles. The mechanism can be understood more clearly from Figure 2.5 which is a schematic of a rocking chair battery based on $LiCoO_2$ and graphitic carbon electrodes. Li-ions get intercalated in these layered electrodes; there is a simultaneous Li-ion insertion and de-insertion at the two electrodes with a concomitant addition and removal of electrons.[81] The reaction can be represented as:

Anode: $C + xLi^+ + xe^- \rightleftarrows Li_xC$

Cathode: $LiCoO_2 \rightleftarrows Li_{1-x}CoO_2 + xLi^+ + xe^-$

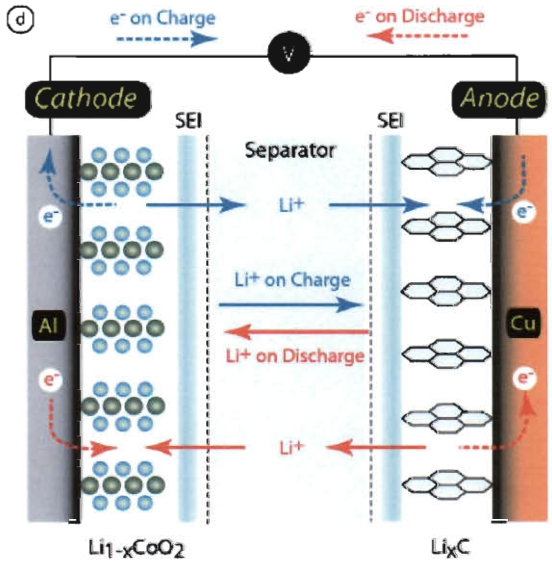

Figure 2.5 A typical configuration of Li-ion battery. Li-ions shuttle between the two electrodes during the charging (blue) and discharging cycles (red). (GM Ehrlich *Handbook of Batteries*, ed. Linden and Reddy 2002)

For anodes, a range of carbonaceous materials have been explored ranging from ordered graphite to disordered carbon. Graphite, the most popularly used material is limited by the intercalation of only one Li ion per 6 carbon atoms which translates to a maximum theoretical capacity of 372 mAh/g.[82] Another carbon form which is demonstrating a significant potential as an anode is carbon nanotubes (CNTs).

2.4.2 Anode Material: Carbon Nanotubes

Carbon nanotubes are one-dimensional allotropes of carbon with sp^2 hybridization which were first reported by Iijima in 1991 using an arc-discharge method.[83] Structurally, CNTs can be envisioned as rolled-up graphene sheets with the diameter of a few nanometers (Figure 2.6 and 2.7). Depending on the number of walls, CNTs can be classified as multi-walled carbon nanotubes (MWCNTs), which have a number of walls arranged concentrically at 0.34 nm distance or as single-walled carbon nanotubes (SWCNTs) with a singular graphene cylindrical wall.

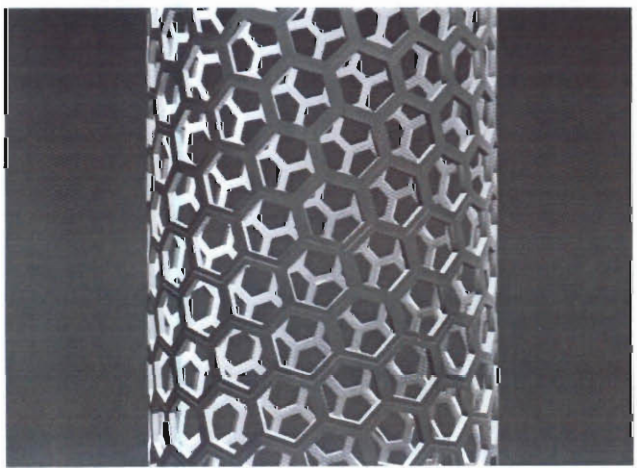

Figure 2.6 Schematic of a SWCNT. It is composed of sp^2 hybridized carbon in a hexagonal honeycomb lattice. (Ajayan et al. Reports on Progress in Physics, 1997, 60)

Figure 2.7 HRTEM image of a MWCNT showing the multiple layers. The interlayer distance is 0.34nm. (Ajayan et al. Reports on Progress in Physics, 1997, 60)

2.4.2.1 CNT Synthesis

CNTs can be grown using a variety of techniques such as laser ablation,[84] arc-discharge[85] and chemical vapor deposition (CVD).[86, 87] Of the various possible methods, CVD is assigned the highest importance due to the ease of scaling-up and the ability to tailor the system which helps in attaining the desired architectures, the features which have made it the chosen process for CNT growth in the studies shown in Chapter 6 and Appendix A. CVD process requires the presence of hydrocarbons which act as a carbon source and a catalyst which promotes the growth of the CNTs. The growth temperatures are generally maintained at 600-1000°C. The processing conditions (pressure, temperature, gas flow rates etc.) and the choice of catalyst and hydrocarbon all influence the final characteristics of CNTs. The tube diameter is primarily controlled by the size of the catalyst; larger catalyst size results in the formation of MWCNT or carbon fibers. Contrary to other techniques like laser ablation[84] and arc-discharge,[85] the CVD process gives the option of aligned and selective growth of nanotubes.[86] This method also offers the flexibility of growing CNTs on a substrate which is a requisite for the experimental

protocol followed in Chapter 6. Though the silicon wafer is the most commonly used substrate, it is possible to carry out growth on conducting substrates also. Ajayan and co-workers have shown the growth of CNTs on Inconel 600.[88] In another report, Wei and Co-workers have shown CNT growth on chemically treated stainless steel using the vapor-phase catalyst delivery.[89] This method involves the passage of catalyst and hydrocarbon in a gas phase over the substrate. A range of transition metals such as iron, nickel, cobalt and molybdenum have been explored as catalysts.[86, 90, 91] At high temperatures carbon dissolves in the catalyst particle and after getting supersaturated, the catalyst starts precipitating out carbon in the form of nanotubes. In an alternative growth technique used in the studies in Chapter 6 and the appendix, instead of introducing in the gas phase, the catalyst is pre-deposited on the wafer. Once the catalyst is activated at high temperatures, hydrocarbons are flowed through the furnace.[86] This method can also be employed to grow CNTs on silicon wafer or on conducting substrates such as metal foils and steel.[92, 93]

2.4.2.2 CNT Properties

The unique structure and strong covalent bonding in CNTs gives it remarkable physical and chemical properties, some of which have been used explored towards various applications shown in Chapter 6 and Appendix A.[94] CNTs are known to be one of the most mechanically robust structures; the axial elastic modulus of isolated nanotubes has been measured to be around 1.8 TPa which is significantly higher than 0.1TPa in-plane modulus of single-crystal graphite.[95] Experimentally, the tensile strength of CNTs has been found to lie in the range of 30-60GPa. CNTs also possess excellent electronic and thermal properties which vary with the chairality, diameter and morphology of the

tubes. The one-dimensional, long-range crystalline structure of nanotubes makes it easier for the phonons to propagate along the CNT surface, resulting in thermal conductivities as high as 3000W/m.k.[96] For electronic applications CNTs can be metallic or semi-conducting with the current densities (10^9A/cm^2) exceeding those of metals. Also, as compared to their other carbon counterpart, graphite, the hollow structure of CNTs gives them a low-density, therefore making CNT composites very light-weight.

Taking advantage of the exceptional intrinsic properties, CNTs have been used for a range of applications in electrochemical storage systems such as batteries, supercapacitors and fuel cells.[81, 97-102] The high surface area and porosity make them particularly viable as electrode material as it increases the interfacial stability. As compared to conventional carbon additives, CNTs can reach the percolation threshold at lower loadings and there is also no requirement of a binder, factors which lead to a significant reduction in the electrode mass. A further weight reduction is possible by using free-standing CNT frame-works which makes an external metal collector redundant. Arrays of CNTs are particularly promising for flexible batteries as the 3-D architecture combines offers both flexibility and mechanical robustness. It can also act as a physical support for the integration of other high capacity materials. This property has been utilized in Chapter 6, where high capacity transition metal oxides has been used in conjunction with CNTs to fabricate a novel hybrid electrode which possesses better capacity than pure CNTs.

Chapter 3

In situ synthesis of metal nanoparticle-embedded free standing multifunctional PDMS films

3.1 Introduction

Polydimethylsiloxane (PDMS) is a widely used polymer due to its extensive set of attractive properties. It has a unique combination of many desirable characteristics such as transparency, flexibility, workability, chemical and thermal stability and low cost.[26] Inclusion of metal nanoparticles can impart additional properties to the polymer and can thereby, expand the existing area of applications. This chapter describes an in-situ route to embed noble metal nanoparticles (gold, silver, platinum) in polydimethylsiloxane (PDMS) matrix. PDMS being a viscoelastic material, dynamic mechanical testing was employed for separately examining the elastic and viscous components of its mechanical properties. The enhancement in properties by nanoparticle inclusion is evident through the improved mechanical and anti-bacterial characteristics displayed by silver nanoparticle-PDMS films. The advantages of this method are apparent in the simplicity of the synthesis protocol and the ability to form a range of nanoparticles in the matrix.

3.2 Materials and Methods

3.2.1 Experimental

PDMS elastomer kit (Sylgard 184, Dow Corning), chloroauric acid, chloroplatinic acid and silver benzoate (Sigma Aldrich) were used as received. The polymer kit contains the oligomer (PDMS) and the curing agent which is composed of

dimethyl,methylhydrogen siloxane, dimethyl siloxane, dimethylvinylated and trimethylated silica, tetramethyl-tetravinyl cyclotetrasiloxane and ethyl benzene. The oligomer (8 grams) was mixed thoroughly with the curing agent in the weight ratio of 10:1 and then degassed under vacuum to remove entrapped air bubbles. Silver benzoate (3 ml, 2×10^{-2}M solution in hexane) was added to this polymer and the mixture was sonicated for 15 minutes for homogenization. The choice of metal salt and solvent was dictated by the ability of the solvent to dissolve both the salt and PDMS. Subsequent to the mixing, the color of the mixture changed to yellowish-brown. It was then cast on glass slides and cured under vacuum at room temperature resulting in free-standing films which were about 1mm thick. For the preparation of gold and platinum nanoparticles, 10^{-4} M chloroauric acid and 2×10^{-5} M chloroplatinic acid solution in methanol was prepared. 4 ml of the solution was added to 8 grams PDMS dissolved in methylene chloride. As methanol and methylene chloride are mutually soluble, it was possible to carry out the subsequent mixing and curing procedure as that used for silver and obtain gold and platinum nanoparticles containing PDMS films.

3.2.2 Characterization and Testing

Various techniques such as UV-Visible spectroscopy, transmission electron microscopy (TEM), X-ray photoemission spectroscopy (XPS), optical imaging and dynamic mechanical testing were used to characterize the films. UV-Visible spectroscopy measurements were performed on the films using a spectrophotometer (Shimadzu UV-3600) operated in the range of 200- 1000 nm at a resolution of 1 nm. The morphology of the nanoparticles was studied using transmission electron microscope (JEOL 2010) operated at 100 kV accelerating beam voltage. Optical imaging (CytoViva) was done to

determine the particle distribution of the nanoparticles in the matrix. The Olympus BX-41 microscope with 100x magnification oil objective was used to get the images. X-ray photoelectron spectroscopy measurements (PHI Quantera SXM) were carried out using monochromatic Al K_α radiation (1486.6 eV) at an incident beam angle of 45° to the sample. Mechanical properties of the nanocomposite films were studied by Dynamic Mechanical Analyzer (TA Instruments Q800). Leaching of silver ions from silver-PDMS films was determined by immersing the films in deionized water (pH 6 ± 0.2) for 2 months at room temperature, and analyzing the supernatant using an Inductively Coupled Plasma Optical Emission Spectrometer (ICP-OES, Perkin Elmer Optima 4300 DV) which has a detection limit of 1 ppb at a wavelength of 328 nm.

For antibacterial studies, the films were carefully sterilized by autoclaving at 121°C for 30 minutes and then incubated overnight (16-18 hr) with microorganisms. Antimicrobial activity was tested on *Bacillus subtilis* 168 (ATCC 31578; Gram positive) and *Escherichia coli* K12 (ATCC 25404; Gram negative) to evaluate antibacterial efficacy for different bacterial cell wall morphological properties. The strains were grown on Luria-Bertani broth at 37°C while shaking at 150 rpm, harvested during exponential growth, and resuspended in minimal Davis media for the experiments.[103] Bacterial growth was monitored in the presence of the films. Cultures exposed to pure PDMS films without silver nanoparticles were used as controls. Growth of cells in suspensions was measured in terms of absorbance at 600 nm, and converted to colony forming units (CFU/mL) using strain specific standard curves. Bacterial mortality was also determined by viable plate counts after 24 hours' growth.

3.3 Results and Discussion

The following sections discuss the characterization results of the polymer nanocomposite films and elaborate on the improvement in mechanical properties and anti-bacterial efficacy obtained by the inclusion of silver nanoparticles. The discussions also include the possible synthesis mechanism which is supported by the experimental results and the existing literature reports.

3.3.1 Gold-PDMS Nanocomposite

The nanocomposite films were formed by mixing the metal salt solution to PDMS elastomer. Gold chloride solution in methanol is yellow-orange in color. On mixing it with the transparent PDMS elastomer, the color of the mixture changes to ruby-red. This change is visible in Figure 3.1(A) which is the photograph of pure PDMS and gold nanoparticle embedded PDMS (Au-PDMS) film. Pure PDMS film is transparent; however, the gold nanoparticle containing film is ruby red which is a well-known, characteristic color of gold nanoparticles Figure 3.1(B) is the UV-Visible spectra obtained from these films. Pure PDMS does not show any absorbance in the visible region whereas Au-PDMS has an absorbance centered at~530 nm. This absorbance originates from the surface plasmon excitation of gold nanoparticles as explained by the Mie theory.[29]

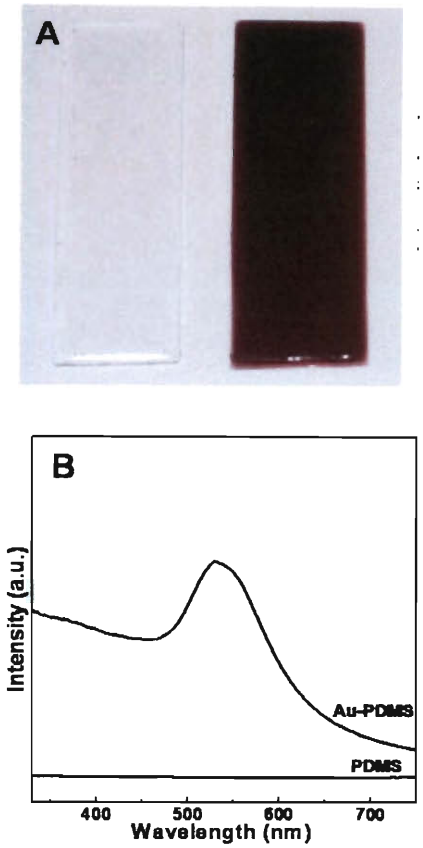

Figure 3.1 (A) Photograph of pure PDMS and Au-PDMS film showing the color change to ruby-red after the formation of nanoparticles. (B) UV spectra of the films. Pure PDMS shows no absorbance but Au-PDMS film absorbs at 530 nm.

For TEM analysis of the nanoparticles, they were extracted from the films using diisopropylamine. In a study on the swelling behavior of PDMS in different solvents, Whitesides and co-workers have found that PDMS swells maximum in the presence of diisopropylamine.[28] Therefore, it was chosen as the medium for extraction. The solvent was added in excess to the mixture of PDMS and metal salt while it was still uncured and viscous. Upon centrifugation, the nanoparticles settle down. The mixture was given repeated wash cycles with diisopropylamine to get rid of the entire polymer. After washing, the centrifuged nanoparticles were sonicated and then drop-cast on a carbon coated copper grid for TEM analysis. Figure 3.2 shows the TEM images of gold

nanoparticles which clearly reveal their discrete nature. The selected area electron diffraction (SAED) pattern obtained from the nanoparticles is shown in the inset. The pattern reveals that the nanoparticles are crystalline in nature; the spots are indexed according to the face centered cubic (fcc) structure of gold.

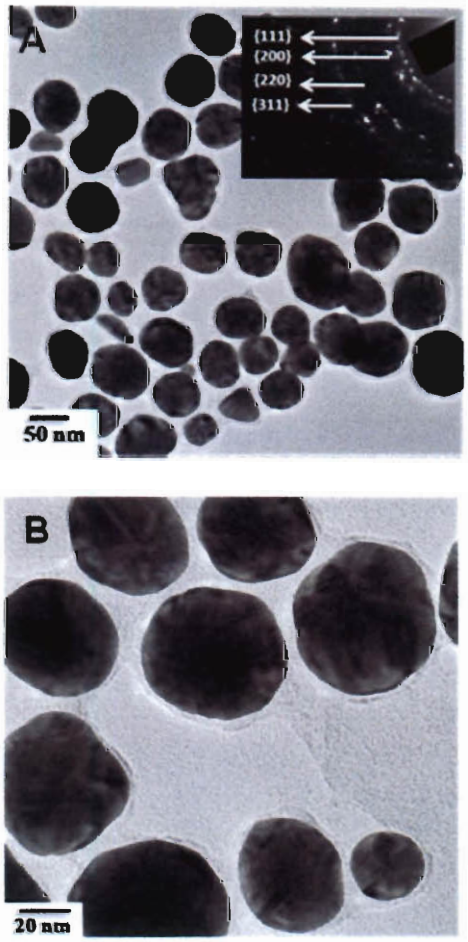

Figure 3.2 TEM images of the gold nanoparticles formed in the PDMS matrix. Inset is their diffraction pattern which indicates the fcc crystalline nature.

The properties of a nanocomposite, such as the present system are strongly governed by the spatial distribution of the nanoparticles in the polymer matrix. To determine this, optical images (Figure 3.3) were taken at different regions of the film

using a high resolution and high contrast condenser (CytoViva). Gold nanoparticles appear as bright spots in these images. As seen from the presence of these spots, the nanoparticles are uniformly distributed over a large area without any significant aggregation.

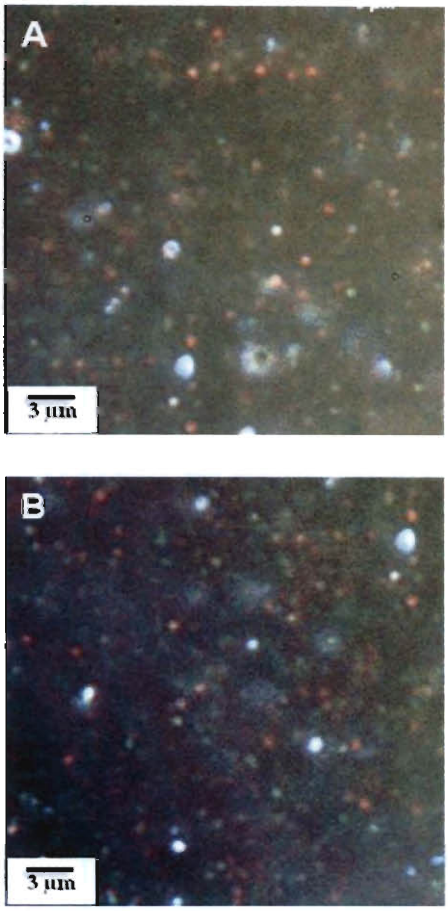

Figure 3.3 Optical images of Au-PDMS film showing the homogenous spatial distribution of nanoparticles in the polymer matrix.

3.3.2 Platinum-PDMS Nanocomposite

Using the same methodology as that used for gold, platinum nanoparticles were also synthesized in-situ in the PDMS matrix using chloroplatinic acid as the metal precursor. The inset of Figure 3.4 shows the Pt-PDMS film after curing where the color

originates from the platinum nanoparticles. TEM studies were carried out to determine the size and morphology of the nanoparticles. The nanoparticles have an irregular shape and are polydispersed with an average particle size of 50 nm (Figure 3.4). The diffraction of platinum nanoparticles (inset) indicates their fcc crystalline nature.

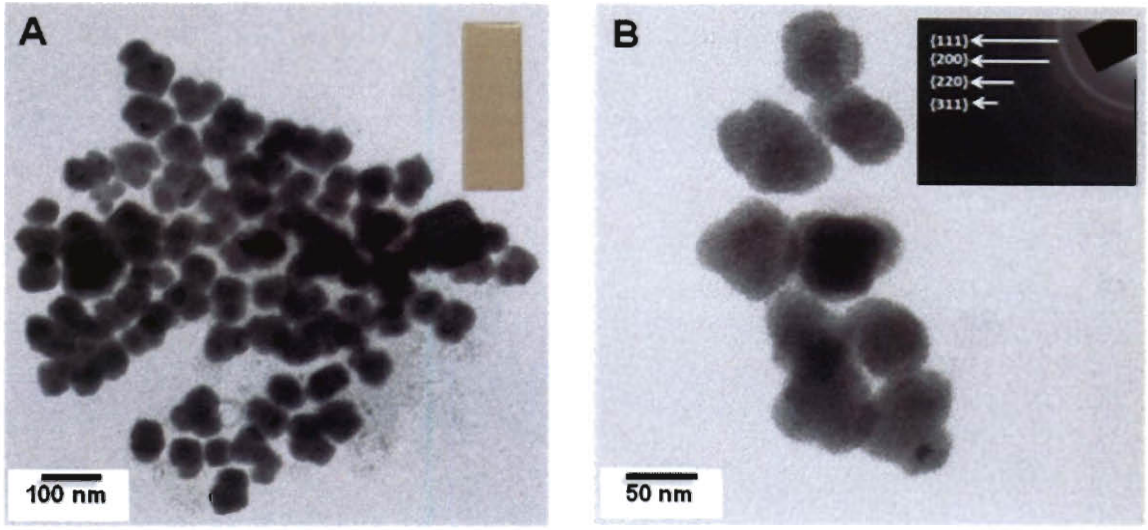

Figure 3.4 (A) and (B) TEM images of the platinum nanoparticles. Inset (A) Photograph of Pt-PDMS film and (B) Diffraction pattern of crystalline platinum nanoparticles.

3.3.3 Silver-PDMS Nanocomposite

The presence of the various nanoparticles in PDMS matrix significantly extends the possible applications of these nanocomposites. Besides gold and platinum, silver was also introduced as it is well known for its antimicrobial activity and has also been used in polymers for other applications such as olefin gas separation.[104] As visible in the photograph in Figure 3.5, silver containing film (Ag-PDMS) is yellowish-brown in color. This characteristic color indicates the formation of silver nanoparticles, which was confirmed by UV-Vis spectroscopy. Ag-PDMS shows a broad peak centered at ~ 415 nm

arising from the absorbance by the nanoparticles. The surface plasmon band is broader and shifted to a higher wavelength as ompared to silver nanoparticles dispersed in a solvent which is in good agreement with the past reports.[105] The nanoparticles were further studied in detail by transmission electron microscopy. Figure 3.6 shows the low and high magnification TEM images of drop-cast film of nanoparticles extracted from the Ag-PDMS film. These images indicate that the nanoparticles are discrete and polydispersed. The inset of Figure 3.6(A) shows the electron diffraction pattern obtained from the nanoparticles. It is evident from the pattern that the nanoparticles are crystalline and have a fcc structure. The particle size was calculated from the TEM micrographs. The size distribution measurement (Figure 3.7) gives the particle diameter to lie in the range of 5-20 nm.

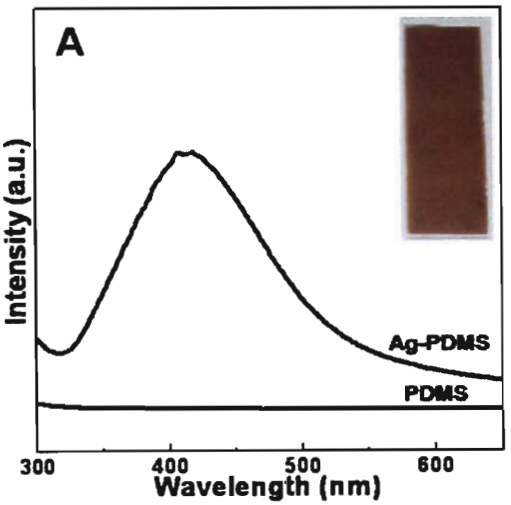

Figure 3.5 (A) UV-Vis spectra of PDMS and Ag-PDMS film. Silver nanoparticles show an absorbance at ~ 415nm. Inset is the photograph of Ag-PDMS film which is yellowish-brown in color due to the presence of silver nanoparticles.

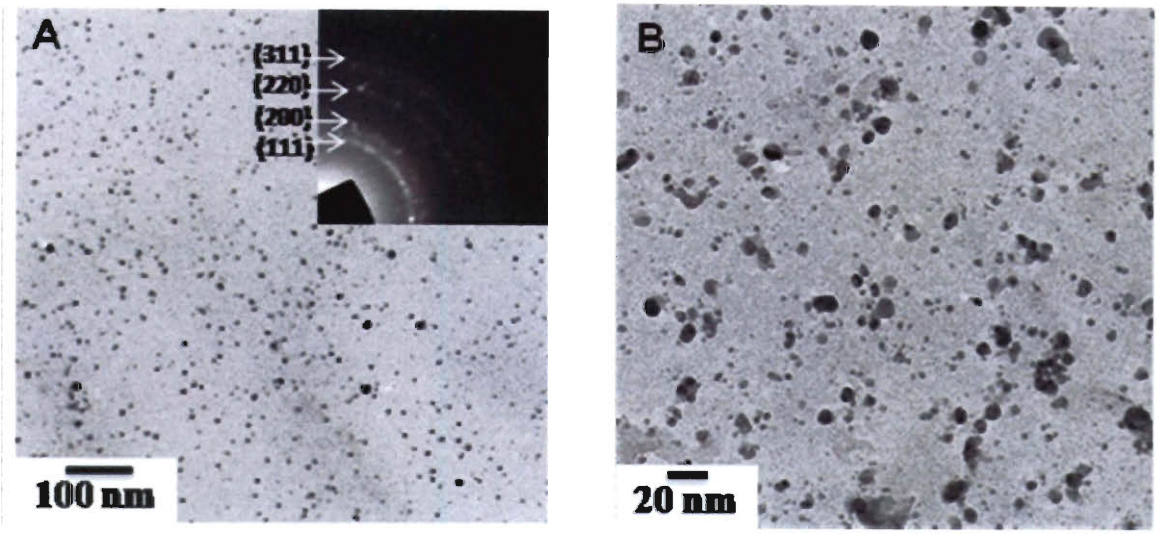

Figure 3.6 (A) and (B) TEM images of the silver nanoparticles formed in the PDMS matrix. Inset is the diffraction pattern obtained from crystalline fcc silver nanoparticles.

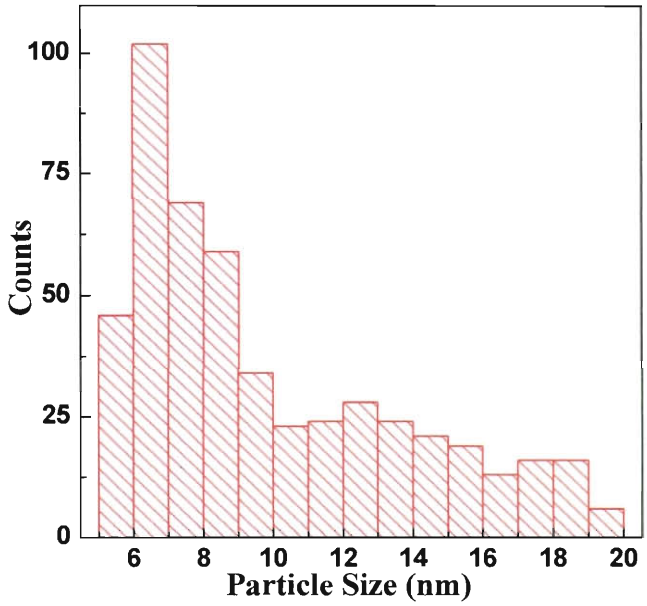

Figure 3.7 Particle size distribution of silver nanoparticles.

In order to understand the chemical interactions of nanoparticles with the PDMS matrix, XPS was performed on a fractured surface of Ag-PDMS film. The general scan spectrum showed C1s, Si2p, O1s and Ag3d core levels. The binding energy of 284.5 eV

for adventitious carbon (C1s) was used as the internal standard. Figure 3.8 shows the Ag3d core level spectrum recorded from the Ag-PDMS film. The spectrum could be resolved into one spin-orbit pairs with the two chemically shifted components, 3d5/2 and 3d3/2 binding energies (BEs) centered at 368.24 eV and 374.25 eV respectively. The peak positions correspond to the electron emission from Ag(0) state and confirm the presence of silver in metallic state.[106] The Si2p spectrum shows a single chemically distinct peak centered at 102.5 eV (Figure 3.8) which is in good agreement with the reported value in the literature.[107]

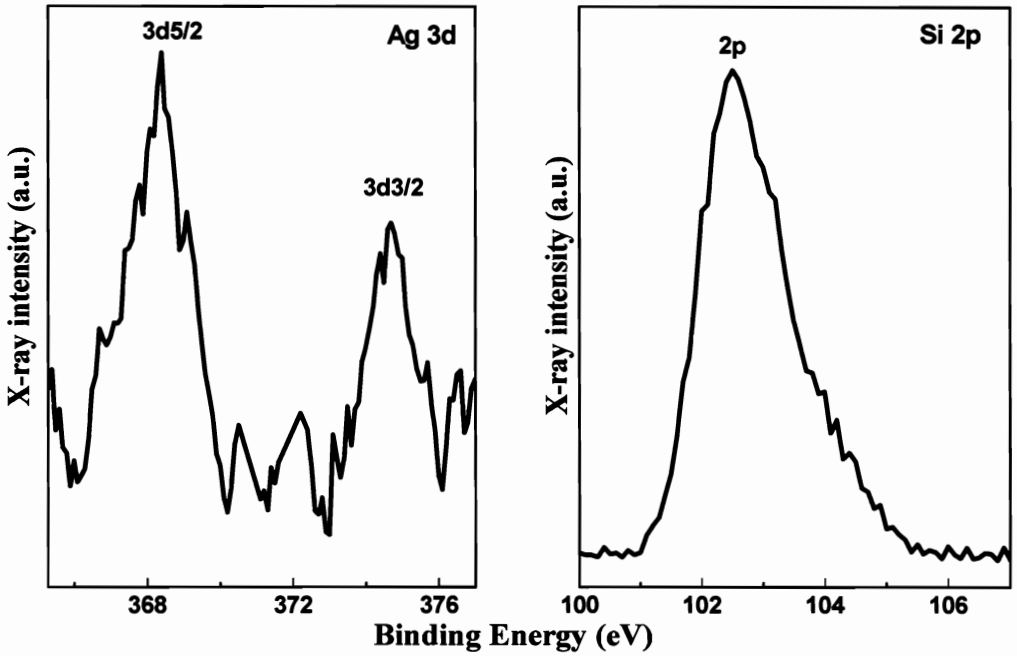

Figure 3.8 XPS spectra of Ag-PDMS film showing the binding energy of Ag3d and Si2p core levels.

3.3.4 Curing Mechanism of PDMS

The PDMS oligomer is vinyl termintated and has a high molecular weight while the curing agent/cross-linker has shorter siloxane chains with several hydride groups. Curing proceeds through an organometallic, platinum-catalyzed hydrosilylation

reaction.[25] The curing agent contains a proprietary platinum-based catalyst that catalyzes the addition of the Si-H bond across the vinyl groups through a series of steps involving oxidative addition of Si-H group of curing agent on Pt, H transfer on the double bond followed by the reductive elimination of the product (Figure 3.9). This curing procedure can be accelerated by heat treatment and results in no by-products in the end. Multiple Si-CH_2-CH_2-Si linkages are formed between the oligomer and the curing agent, leading to a three-dimensional cross-linking as shown in Figure 3.9.

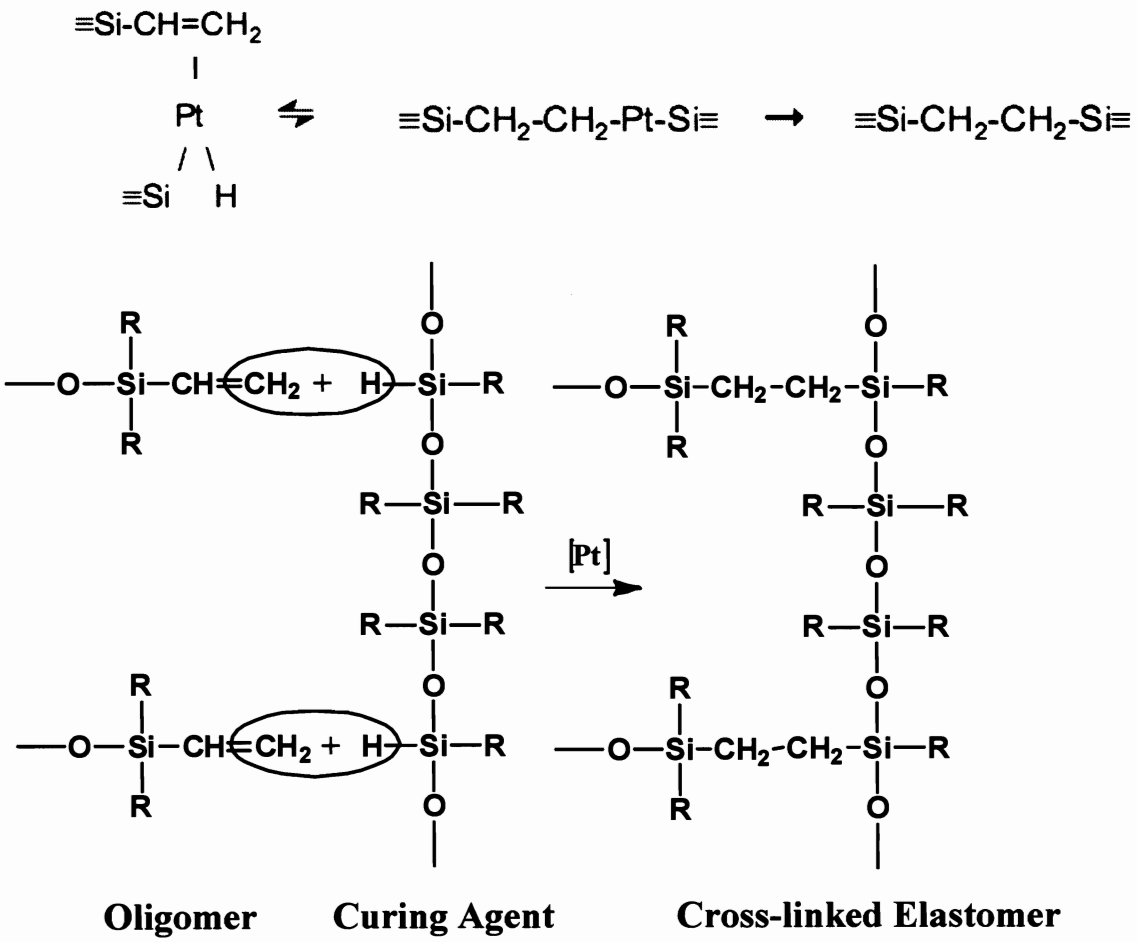

Figure 3.9 Curing mechanism of PDMS. It involves platinum-catalyzed hydrosilylation reaction across the vinyl groups of the oligomer.[25]

3.3.5 Synthesis Mechanism

Controlled experiments were performed to confirm the mechanism of formation of nanoparticles. Silver benzoate solution was mixed separately with pure PDMS elastomer and curing agent. Pure curing agent solution is transparent (Figure 3.10(A), vial 1) but transforms to the yellowish-brown color (Figure 3.10(A), vial 2), similar to that observed in the Ag-PDMS films, after the addition of curing agent. The pure elastomer displayed no color change as visible from the last vial numbered 3. Similarly gold and platinum salts were also reduced by the curing agent but did now show any reduction with pure elastomer. This controlled test is a strong preliminary indicator that the curing agent is responsible for the reduction of metal salt.

To corroborate this hypothesis and understand the exact mechanism of reduction, FTIR spectra of pure curing agent (CA) solution and of the same solution after the formation of nanoparticles (brown colored, CA+AgB) were compared (Figure 3.10 B). The peak at 1586 cm^{-1} arises from the carboxylic group present in silver benzoate. The curing agent has Si-H groups which are IR active. The absorbance peak at 2162 cm^{-1} in both spectra corresponds to stretching vibration of these groups.[108] The comparison of peak intensities shows that the peak intensity of Si-H group gets reduced after the formation of silver nanoparticles. It is well-known in literature that Si-H bond can reduce the metal salts to form nanoparticles and in exchange it gets oxidized to Si-O-Si.[29] The feasibility of metal reduction is clear by the lower reduction potential of silanes (0.34 to 0.54 V)[109] as compared to that of metals (gold, 1.5 V and silver, 0.7 V). Silanes have been reportedly used to reduce metal salts and deposit them in a pre-defined pattern.[109] Silanes are also known to reduce the metal catalyst, platinum, palladium and rhodium

during the hydrosilylation reaction of alkenes.[110] FTIR studies confirm the occurrence of a similar reduction mechanism by the Si-H group present in the curing agent, leading to the formation of metal nanoparticles.

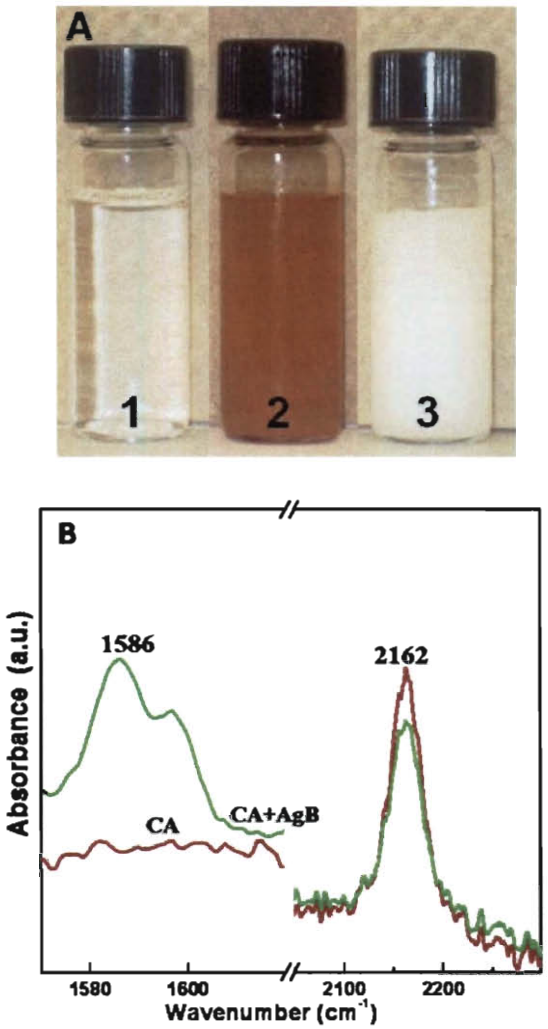

Figure 3.10 (A) Photographs of vials containing (1) pure curing agent (2) silver benzoate solution with curing agent and (3) silver benzoate with pure elastomer. The color difference between vials 2 and 3 indicates that the nanoparticle reduction takes place only with curing agent. No reduction is observed with pure elastomer (B) FTIR spectra of solutions (1) and (2). Si-H groups are consumed during the nanoparticle synthesis causing a decrease in peak intensity.

3.3.6 Mechanical Properties

Mechanical properties of the composite were accessed using DMA. Stress-strain curves were recorded for films containing 0.1 weight% silver (Figure 3.11(A)). Dynamic mechanical analyzer was used in the tension mode at 1 Hz frequency and 0.01 N preload. The quasi-static Young's modulus was calculated using the slope of the best-fit line to the linear part of the curve extending till 20% strain. Overlay of the stress-strain curves shows that the Young's modulus for the nanoparticle containing films is 1.64 MPa which is approximately 3 times higher than 0.56 MPa for pure PDMS. The average modulus was found to be 1.7±0.2 MPa for Ag-PDMS and 0.5±0.1 MPa for PDMS. The values for PDMS are comparable to those reported earlier.[111] The increase in modulus for Ag-PDMS indicates that the nanoparticles form a good interface with the polymer. The high surface to volume ratio of nanoparticles further results in a substantially large interface for polymer-nanoparticle interactions. This serves to improve load transfer within the nanocomposite network, resulting in a higher modulus. The presence of a secondary phase in the polymer matrix also tends to restrict the free mobility of polymer chains.

In order to evaluate differences in the energy damping properties, storage and loss moduli were measured at room temperature as a function of frequency (1-15 Hz) under an oscillatory load. The phase shift, tan delta indicates the damping effectiveness of a material. The dynamic frequency sweep plot (Figure 3.11(B)) for the tangent delta values demonstrates that there is no significant difference between the damping capabilities of the two systems. Like any characteristic viscoelastic material, the storage modulus (E') increases with frequency as shown in the inset. The restraining effect of the inorganic component such as silver on the chain mobility of the PDMS depends on the extent of

chain confinement caused by silver nanoparticles at the interface. Owing to very high specific surface area of extremely small silver particles, a good interface is formed between the particles and PDMS which increases the storage modulus reasonably. The friction between relatively less mobile PDMS chains at the interface also increased leading to an increase in the loss modulus also. However, the ratio of the two moduli does not change significantly, thereby keeping tan delta same.

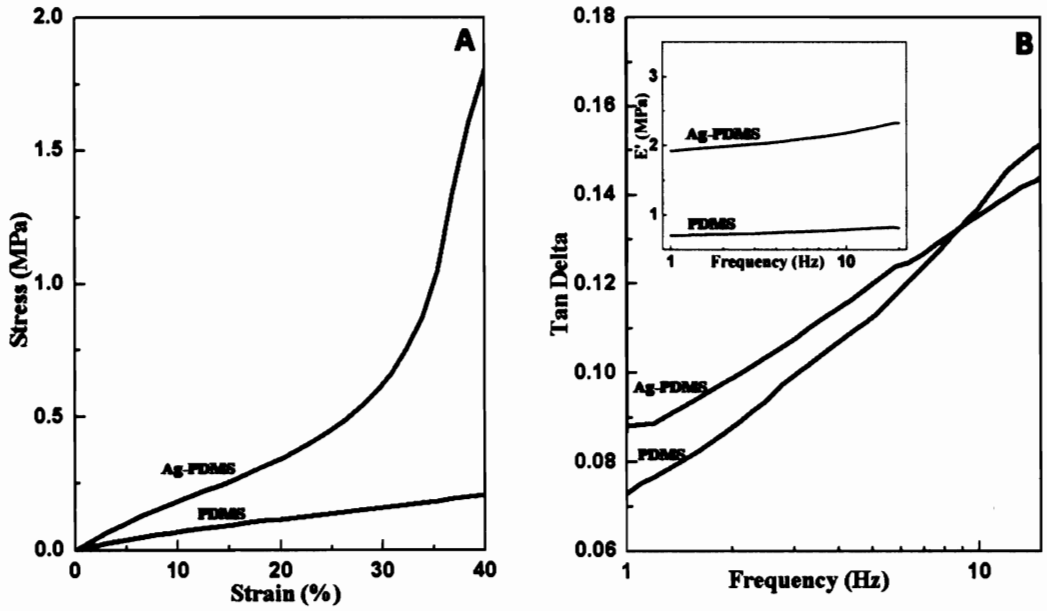

Figure 3.11 (A) Comparison of stress-strain curves of pure PDMS and Ag-PDMS. Silver nanoparticles increase the mechanical strength by three times. (B) Tangent delta vs. frequency curves for PDMS and Ag-PDMS films. There is no significant change in damping properties. Inset is the comparison of their storage moduli.

3.3.7 Swelling Properties

Poor chemical compatibility of PDMS with organic solvents poses a major restriction on its applications including its use in microfluidics where studies in PDMS channels are restricted to non-wetting polar liquids. Thus, it is important to study the

behavior of Ag-PDMS films in organic solvents. To quantify the organic solvent tolerance of Ag-PDMS films, pre-weighed films (W_i) were immersed in different solvents at room temperature. The films were weighed at different time intervals (W_o) till no change in weight was seen and the films reached an equilibrium swelling. The degree of swelling (SD) was calculated based on the difference between the two readings:

$$\mathbf{SD(\%)} = \left(\frac{\mathbf{w_o - w_i}}{\mathbf{w_i}} \right) \times \mathbf{100}$$

Solvent	Ag-PDMS Film	PDMS Film
THF	218	175
Toluene	195	132
Methylene Chloride	225	152
Acetone	16	17
Water	0	0

Table 3.1 Percentage Degree of Swelling. Pure PDMS films have a better tolerance to organic solvents as compared to Ag-PDMS films.

Comparison of the degree of swelling for Ag-PDMS and PDMS is shown in Table 3.1 which reveals that in organic medium Ag-PDMS swells more as compared to pure PDMS. However, there is no significant difference in the swelling for polar solvents. The lesser resistance of Ag-PDMS to organic solvents may be due to a lower degree of cross-linking.[111] Some of the curing agent gets consumed in the reduction of the silver

salt and hence the available curing agent for cross-linking in Ag-PDMS is less than in pure PDMS which may result in greater swelling.

3.3.8 Antibacterial Properties

The antibacterial activity of Ag-PDMS was studied by incubating *B. subtilis* and *E. coli* bacterial strains with the films. In the study, both (Gram-positive) *B. subtilis* and (Gram-negative) *E. coli* bacteria experienced decreased growth in the presence of Ag-PDMS membranes. Viable plate counts were carried out to distinguish bactericidal from bacteriostatic effects. We found that 80% *E. coli* and 52% *B. subtilis* were inactivated upon 24 hours' exposure to Ag-PDMS (Table 3.2). Bacterial growth inhibition and inactivation may be attributed to very low concentrations of silver ions (9 ppb) released from the Ag-PDMS films as measured by ICP. Although exposure to silver ions causes several orders of magnitude reduction in bacterial populations, the amounts of inhibition and inactivation obtained in this study are comparable to those previously reported for products containing silver nanoparticles.[112, 113]

	E. coli **(10^4 cfu/mL)**	***B. subtilis*** **(10^4 cfu/mL)**
Control culture	3.1 ± 0.3	2.0 ± 0.13
PDMS	3.0 ± 0.3	2.0 ± 0.44
Ag-PDMS	0.66 ± 0.1	0.96 ± 0.12

Table 3.2 Confirmation of antibacterial activity of Ag-PDMS towards *E. coli* and *B. subtilis*. Statistically significant decrease in the number of colony forming units (cfu) of both the strains in the presence of Ag-PDMS indicates its antibacterial activity.

3.4 Conclusions

A single-step in-situ process has been developed towards synthesizing metal nanoparticle embedded PDMS films. The process operates by using the curing agent for both reduction and curing purposes, thereby eliminating the need for an external reducing agent. The good dispersion and low particle size of silver nanoparticles in the polymer matrix enhances the mechanical strength and the antibacterial efficacy of PDMS but the films suffer from a lower tolerance to organic solvents. The presence of metal nanoparticles in the matrix, endows it with various properties which makes the polymer nanocomposite a strong candidate for various bio-medical, optical and catalytic applications.

Chapter 4

In-situ Synthesis of Metal Core-Siloxane Shell Nanoparticles and Siloxane Nanowires

4.1 Introduction

The previous chapter pertains to the synthesis of metal nanoparticle-siloxane polymer composite films using the reduction of metal salts by silane groups. This chapter extends the same mechanism to form in-situ metal nanoparticles which are further used to synthesize metal core-siloxane shell (gold, silver) nanoparticles and siloxane nanowires. The reduction of metal salt and the polymerization of silane take places spontaneously, resulting in the formation of composite nanostructures. Contrary to the previously existing methods, this is a simple room temperature route which does not require high temperature refluxing.[65,66] This method circumvents the use of pre-synthesized nanoparticles and renders an additional advantage in that the shape of resulting composite structures (1-D nanowires or 0-D spherical nanoparticles) can be controlled by adjusting the synthesis parameters.

4.2 Materials and Methods

Octadecylsilane ($C_{18}H_{37}SiH_3$, ODS), chloroauric acid ($HAuCl_4$, gold chloride), 3-pentanone and ethanol were purchased from Sigma Aldrich and used as received. Octadecylsilane was the preferred silane compound as it is well-known to polymerize to siloxane in the presence of water.[65, 66] Pentanone and ethanol were the chosen solvents due to their high mutual miscibility.

For the synthesis of core-shell nanoparticles, the following procedure was adopted. 18 mg of octadecylsilane was dissolved in 10 ml of pentanone, and 10^{-2} M chloroauric acid solution was prepared in ethanol. 2 ml of this metal salt solution was added at a rate of 1ml/min to 10 ml of ODS solution under constant stirring. The reaction was carried out at room temperature and under atmospheric conditions. This ensured the presence of water vapor, which is critical for the reaction to proceed. On modifying the ratio of the precursors, significantly different structures were obtained; nanowires were formed when the amount of chloroauric acid added was reduced. For the nanowire synthesis, 0.1 ml chloroauric acid solution was added to 10 ml of ODS solution, as compared to 1ml of chloroauric acid used for the synthesis of nanoparticles.

The resulting solution was analyzed by UV-Vis spectroscopy (Shimadzu UV-3600) at a resolution of 1 nm, and the as-formed nanostructures were characterized extensively by SEM, TEM, XRD, XPS and FTIR. Morphological and elemental analyses were carried out using a scanning electron microscope (FEI Quanta 400) operated at 20 kV. The crystalline nature of the products was determined by a X-ray diffractometer (Rigaku D/Max Ultima II) operated at 40 kV. Transmission Electron Microscopy (JEOL 2010) was done at 100 kV on drop-cast samples prepared on carbon coated copper grids. XPS studies were carried out on a spectrophotometer (PHI Quantera SXM) using the monochromatic Al K_α radiation (1486.6 eV). To indentify the functional groups present, samples were scanned for FTIR spectroscopy (Shimadzu FTIR 8400-S) with 2 cm^{-1} spectral resolution in the range of 700-4000 cm^{-1}.

4.3 Results and Discussion

This section documents the characterization analysis of the as-formed nanostructures. The section further provides an explanation and experimental validation for the observed effects and proposes a synthesis mechanism.

4.3.1 Gold Core-Siloxane Shell Nanoparticles

Upon the addition of gold chloride solution to ODS, the transparent ODS solution gradually transformed to a ruby-red color. This characteristic color is a strong indication of the formation of gold nanoparticles. UV-Vis studies were carried out on the solution as gold nanoparticles show a strong absorbance in the visible region of spectrum due to their surface plasmon resonance. As explained by the Mie theory, the peak characterisitics depend strongly on various factors such as the size and shape of the nanoparticles and the dielectric constant of the medium.[114] The UV-Vis spectrum of pure ODS solution in pentanone was compared with that of the ODS solution after the addition of gold chloride. The spectrum of pure pentanone was used for the background correction. Figure 4.1(A) depicts the changes in UV-Vis absorbance of the ODS solution after the addition of gold chloride. It is clear from the spectrum that the pure ODS solution did not show any absorbance in the visible region. However, a broad peak centered at ~577 nm, appeared upon the addition of gold chloride. This peak originates due to the surface plasmon absorption by gold nanoparticles formed in solution.

For XRD studies, a thick film of the same ODS solution was made on a glass slide. Figure 4.1(B) is the XRD pattern recorded from the dried film. Sharp, high-intensity peaks in the pattern indicate the crystalline nature of the nanoparticles. The prominent peaks at 2-theta values of 38.38°, 44.4°, 64.6° and 77.6° correspond to {111),

{200}, {220} and {311} Bragg reflections from face-centered cubic (fcc) gold (JCPDS# 4-784).

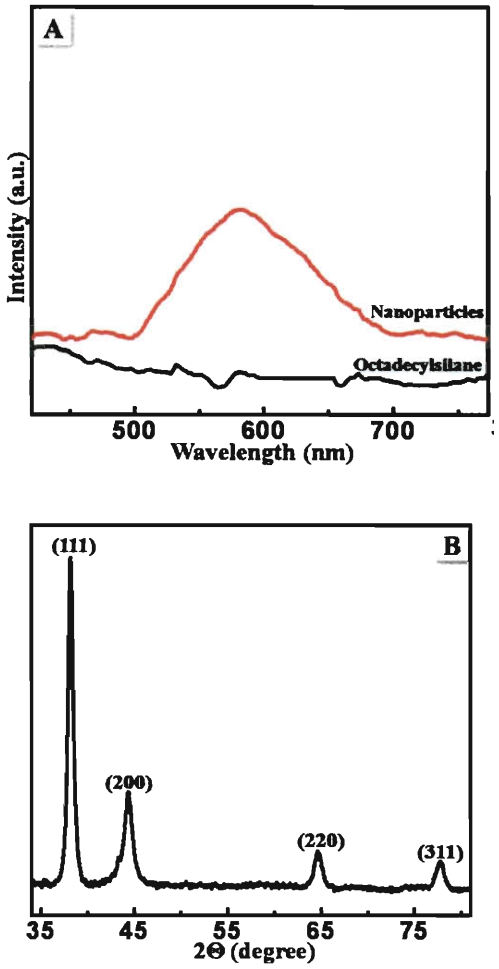

Figure 4.1 (A) UV-Vis spectra of pure octadecylsilane and gold-siloxane nanoparticle solution in pentanone. A characteristic gold nanoparticle peak can be seen at ~ 577 nm. (B) XRD pattern of the nanoparticles showing peaks from fcc crystalline gold.

The size and morphology of the nanoparticles were determined using SEM and TEM. A drop-coated film of the nanoparticle solution was cast on copper foil and on 300 mesh-size carbon-coated copper grid for SEM and TEM studies respectively. As

observed from the SEM images in Figures 4.2(A) and (B), the nanoparticles have a distorted spherical shape. The zoomed-in image shows that they are discrete with very little agglomeration.

A representative TEM image of the nanoparticles is shown in Figure 4.2(C). The image reveals isolated nanoparticles with a distinctive core-shell structure. There is an evident variation in the contrast between the dark gold core and the lighter siloxane shell, indicating that the gold nanoparticles are stabilized by a siloxane shell. The thickness of the shell varies across particles and often exhibits morphology that is different from that of the core. As discussed previously, XRD had confirmed gold to be present in the crystalline state and there were no other peaks present besides those of gold. In conjunction with these XRD results, the TEM data suggests that the nanoparticles have a crystalline metal core coated with an amorphous siloxane layer.

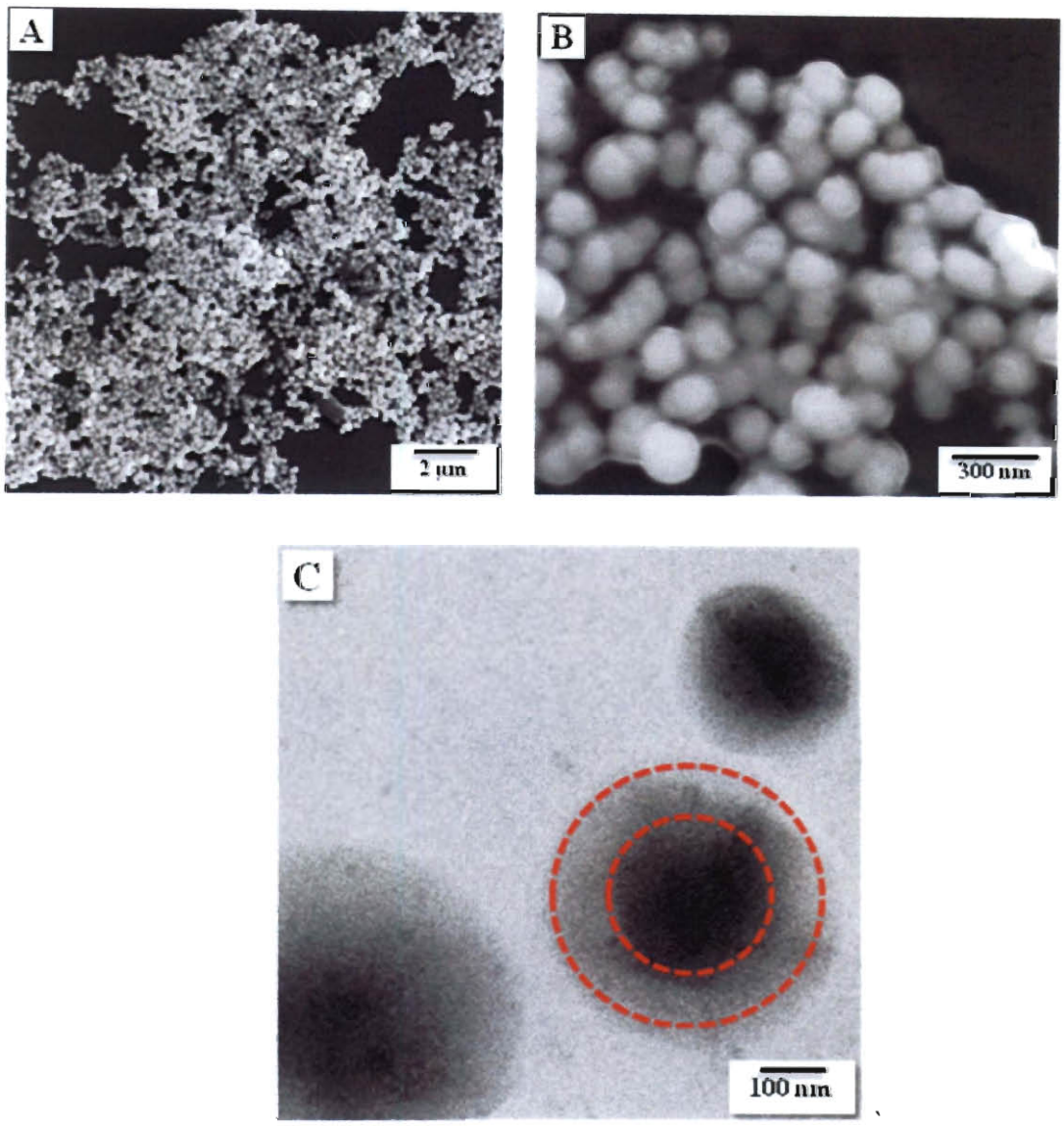

Figure 4.2 (A) and (B) SEM images of gold-siloxane nanoparticles. (C) High magnification TEM image revealing their spherical core-shell structure.

As seen from these microscopy studies, there is a polydispersity in the size of the nanoparticles. Size distribution of the nanoparticles was calculated using these SEM images and other similar micrographs. It can be seen in Figure 4.3(A) that there is a wide distribution in the size of the nanoparticles, ranging from 100 to 260 nm. EDS analysis was carried out to obtain the elemental composition of the nanoparticles. For EDS, the

sample was prepared on a copper foil to avoid any interfering signal from the substrate. Figure 4.3(B) shows the EDS spectrum obtained from the nanoparticles, containing Au(M), Si(K), C(K), Cu(L) and O(K) peaks, which confirms the presence of both gold and silicon these nanoparticles. The copper signal in the spectrum originates from the substrate.

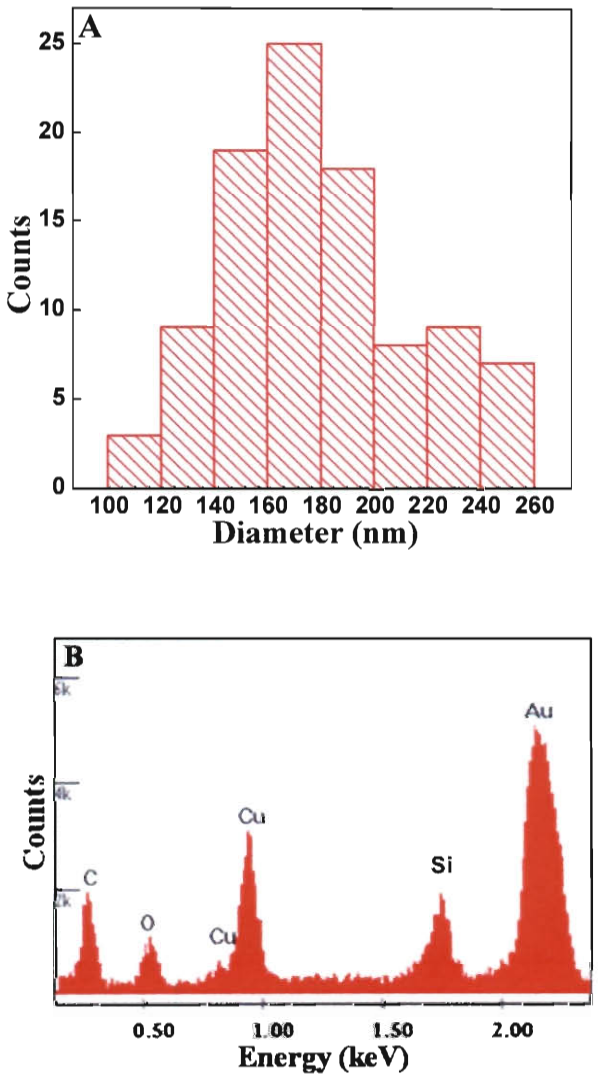

Figure 4.3 (A) Diameter distribution of the nanoparticles (B) EDS spectrum obtained from the nanoparticles confirming the presence of both gold and silicon.

4.3.2 Silver Core-Siloxane Shell Nanoparticles

To bring forth the generic nature of this synthesis approach, nanoparticles with cores other than gold were also synthesized. Silver-siloxane core shell nanoparticles were formed using silver nitrate as the metal precursor while maintaining all experimental conditions identical to those used for gold-siloxane nanoparticles. On mixing the silver nitrate and ODS solutions, the resulting solution spontaneously turned yellow in color and subsequently transformed to dark blue. The color change to yellow indicates the formation of colloidal silver nanoparticles, and color change to dark blue suggests particle aggregation.[115]

As anticipated, the silver-siloxane nanoparticles show characteristics which are consistent with those observed for gold-siloxane nanoparticles. Figure 4.4(A) and (B) are the SEM images of silver-siloxane nanoparticles showing their size and morphology. Silver-siloxane nanoparticles are polydispersed and discrete spheres with diameters between 80-240 nm (Figure 4.4(C)) which is close to the 100-260 nm diameter distribution of gold-siloxane nanoparticles. The results for UV-Vis spectroscopy and EDS analysis are shown in Figure 4.5 (A) and (B) respectively. For the UV-Vis studies, the nanoparticle solution gives a pronounced absorbance peak, centered at ~ 420 nm in the visible region, which strongly suggests the formation of silver nanoparticles.[115] EDS pattern reveals the presence of both silver and silicon in the nanoparticles. The copper peak in the spectrum is from the copper foil which has been used as the substrate. The XRD pattern of nanoparticles (Figure 4.6) shows well-defined peaks corresponding to the fcc structure of silver (JCPDS# 01-071-3762). Thus it can be inferred that similar to gold nanoparticles, silver nanoparticles are also crystalline.

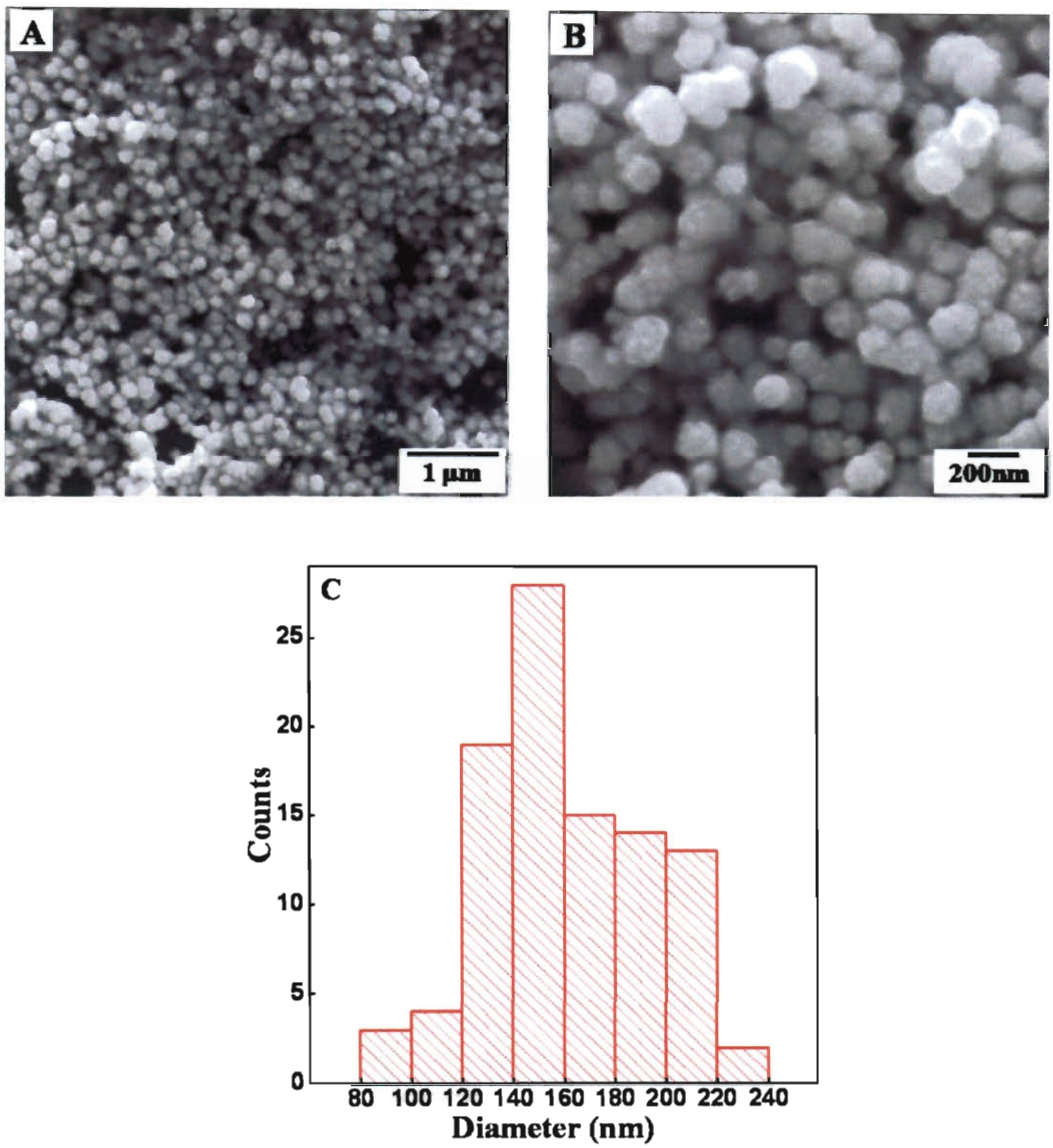

Figure 4.4 (A) and (B) SEM images of the silver-siloxane nanoparticles. (C) Particle size distribution of the nanoparticles.

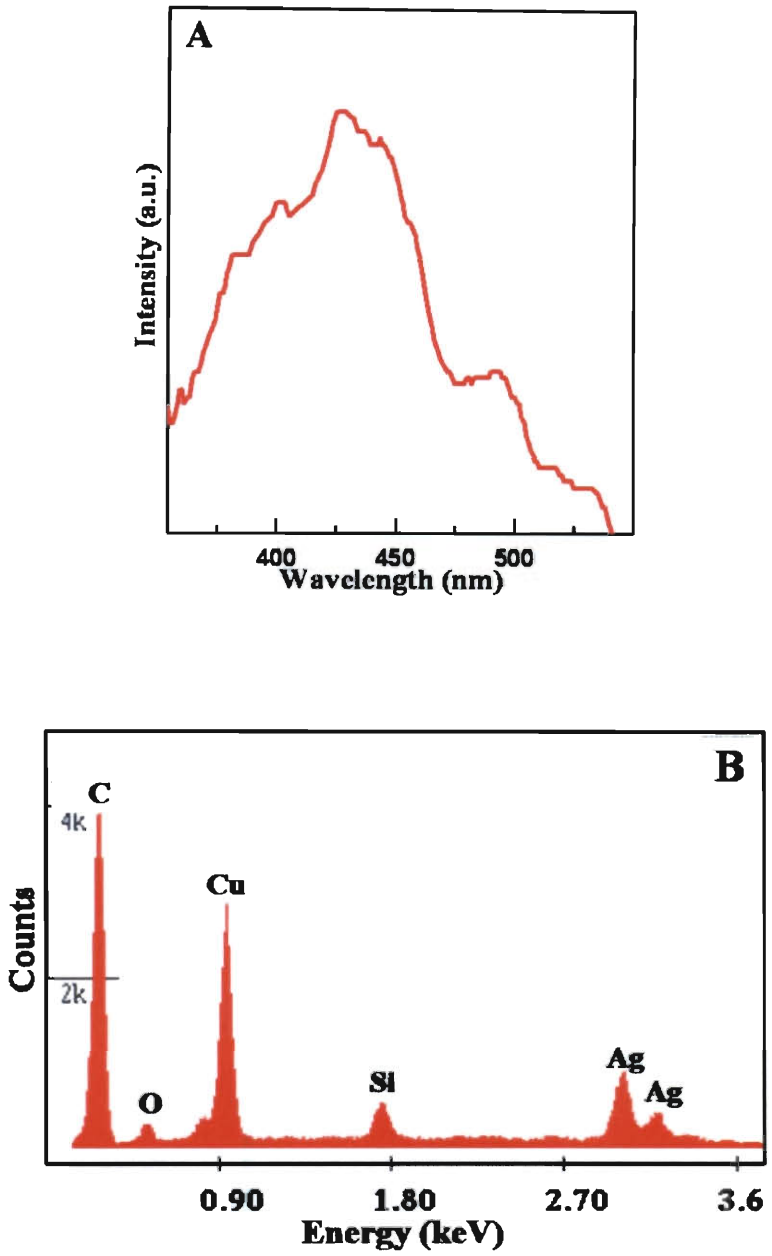

Figure 4.5 (A) UV-Vis spectrum of silver nanoparticles. The peak at 420 nm originates from the surface-plasmon resonance of the nanoparticles (B) EDS spectrum of the nanoparticles showing the presence of both silicon and silver.

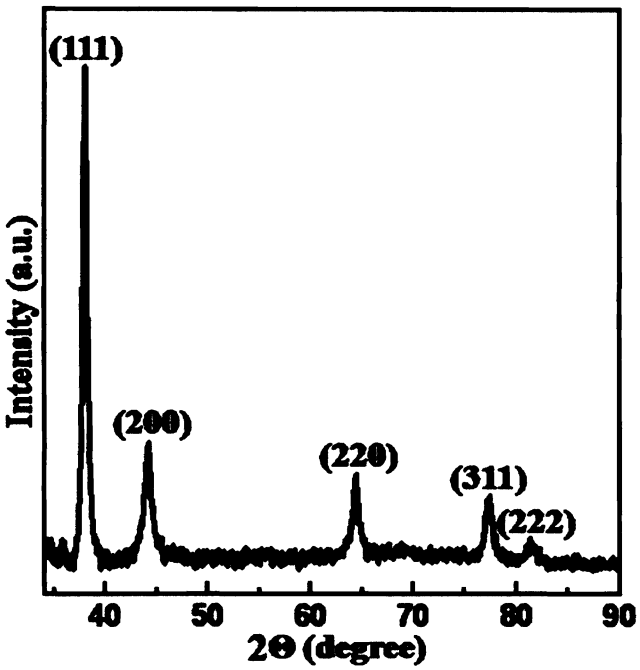

Figure 4.6 XRD pattern of the nanoparticles corresponding to crystalline fcc silver

4.3.3 Hybrid Nanowires

The same synthesis protocol, as that used for nanoparticle synthesis was modified to facilitate the formation of nanowires by increasing the ratio of ODS to metal salt. In contrast to the spherical nanoparticles, the presence of excess ODS in the solution favors the continued growth of core-shell nanoparticles laterally, resulting in long, one- dimensional nanostructures. The nanowires are discrete with a pronounced irregular and bent geometry. Some of them also exhibit highly helical, noodle-like structures as seen in Figure 4.7(A) and (B). The nanowires grow up to 160 nm in diameter and a few microns in length. Their diameter distribution is in the range of 50-160 nm as observed in the histogram in Figure 4.8.

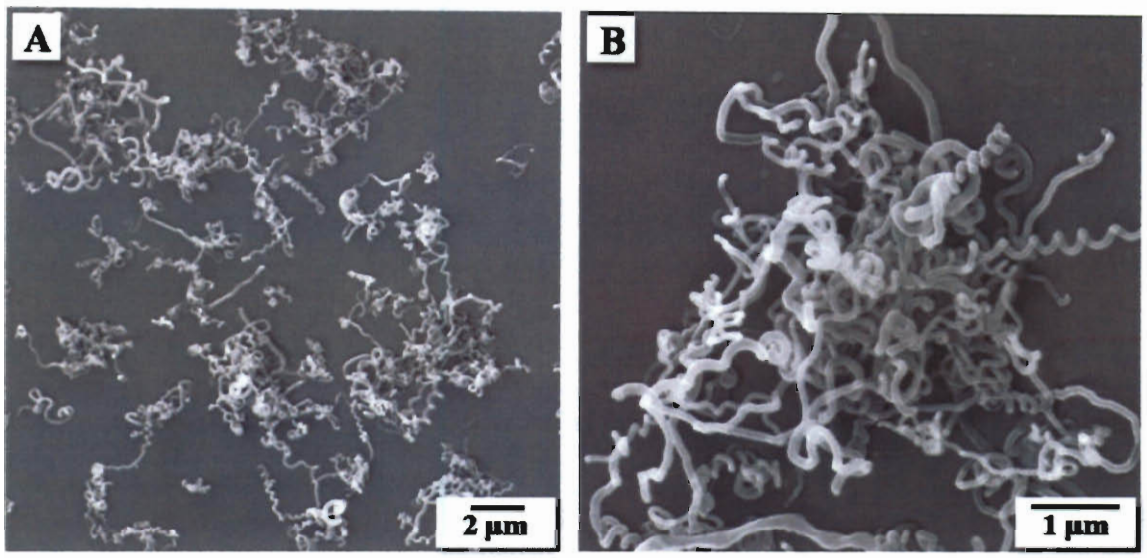

Figure 4.7 (A) and (B) SEM images showing micron-long, irregular and helical nanowires.

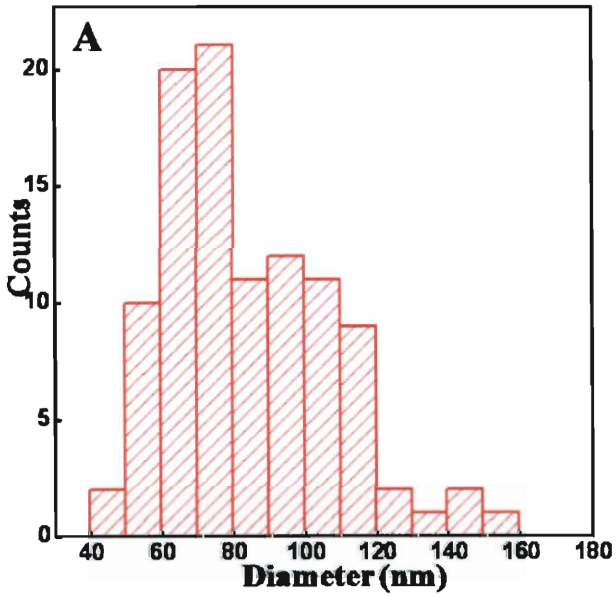

Figure 4.8 Diameter distribution of the nanowires.

SEM images were also recorded in the back-scattered electron mode to obtain the compositional information and the spatial distribution of different elements in the

nanowires. The stark contrast in Figure 4.9(A) effectively highlights the finding that the higher atomic number gold nanoparticles are present as bright spots on the tip of the nanowires and the rest of the nanowire body is composed of siloxane. The presence of gold nanoparticle at the tip of each individual nanowire is further corroborated by TEM micrograph in Figure 4.9(B). This observation is in agreement with those reported by Prasad et al.[65] who have also shown similar 1-D nanostructures and have attributed the gold nanoparticles at the tip to drive the formation of nanowires.

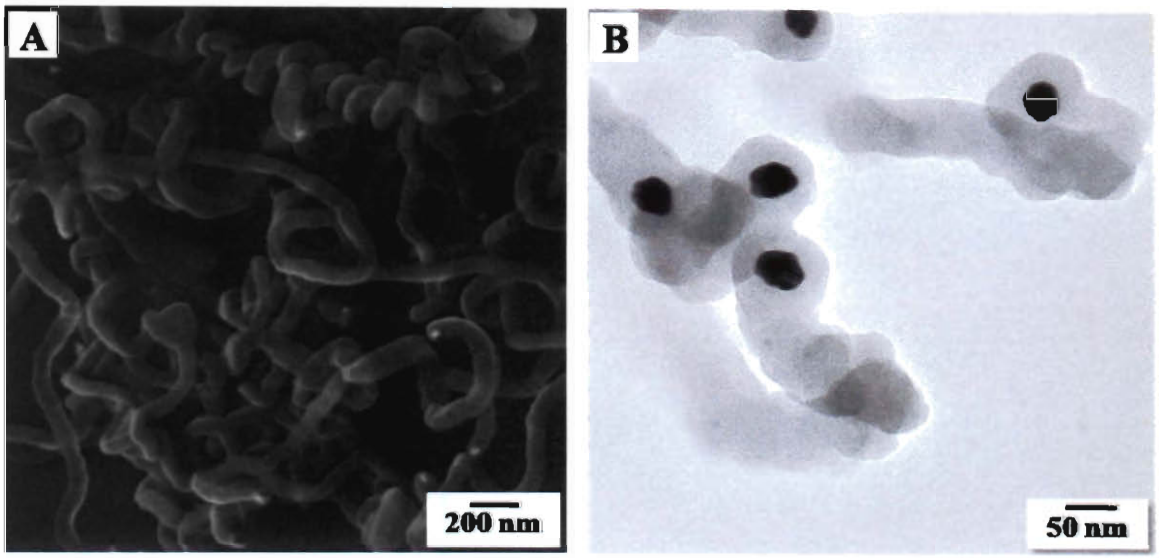

Figure 4.9 (A) Back-scattered SEM image and (B) TEM image of the nanowires revealing the presence of gold nanoparticles at their tips.

Controlled SEM studies were performed using only pure ODS solution in the absence of metal salt. A significantly different morphology was seen as shown in Figure 4.10. Contrary to the well-defined shapes obtained with the metal salt, only a thick coating was formed with pure ODS which is compelling evidence that the metal nanoparticles are essential for the reaction to take place and that they act as a template for the formation of nanostructures.

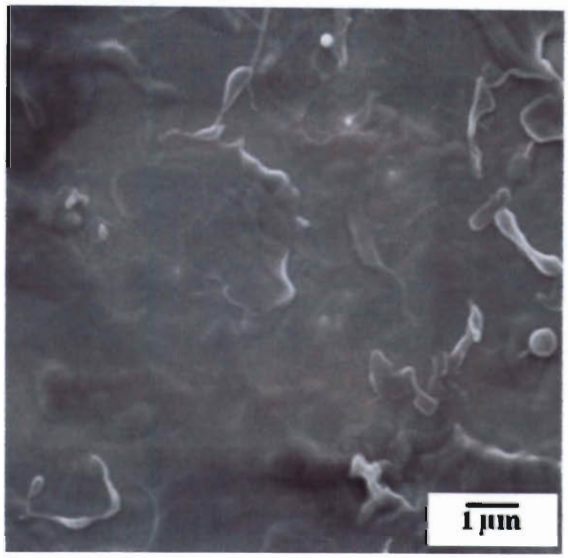

Figure 4.10 Controlled experiment showing the formation of a thick siloxane layer with pure ODS in the absence of metal salt.

4.3.4 Synthesis Mechanism

To understand the mechanism of formation, XPS and FTIR studies were carried out. Indium foil was used as a substrate for XPS measurements. The XPS scan of the gold-siloxane nanoparticles revealed the presence of C1s, Si2p, O1s and Au4f core levels with no evidence of impurities. The binding energy of 284.5 eV for adventitious carbon (C1s) was used as the internal standard. Figures 4.11 (A) and (B) are the Au4f and Si2p core level spectra obtained from the nanoparticles. The Au4f peak can be resolved in one spin-orbit pair coupling (splitting ~3.7 eV) centered at 84.3 eV and 88.1 eV corresponding to $4f_{7/2}$ and $4f_{5/2}$ core levels. The binding energy of Au4f core level is in good agreement with Au(0) oxidation state.[116] The Si2p spectrum has a broad peak that could be split into multiple peaks. These peaks could be distributed between three different components centered at ~ 100.5, 101.7 and 103.2 eV, corresponding to the

binding energy of Si in Si-H, Si-C and Si-O-Si respectively. As deduced from the relative intensity of the components, the major contribution is from the Si-O-Si peak indicating the prominence of siloxane in the nanostructure composition.

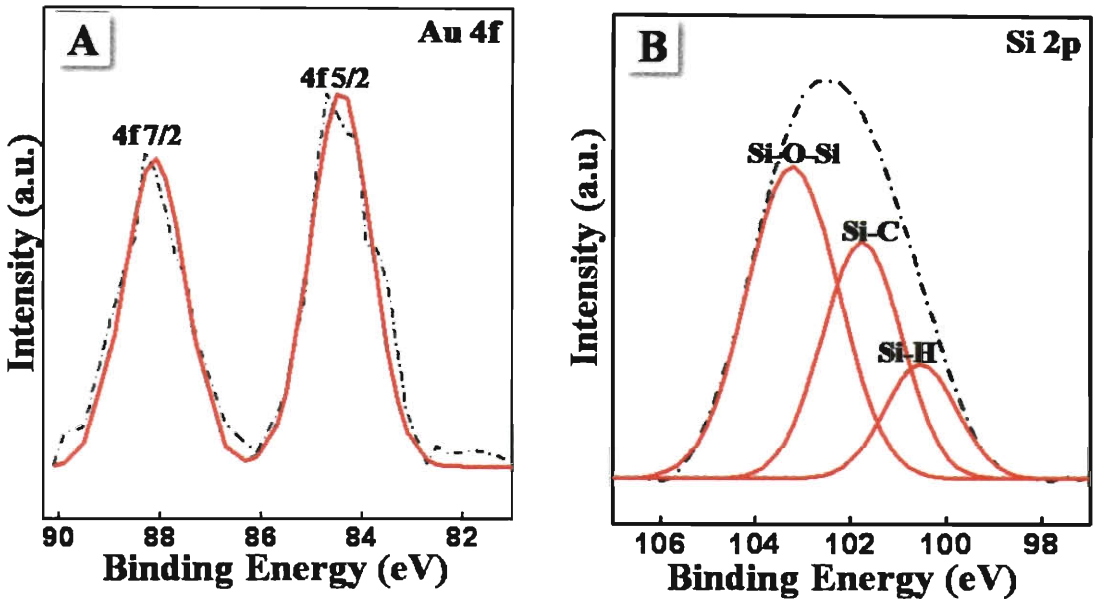

Figure 4.11 XPS spectra of the nanoparticles showing the binding energies of (A) Au4f and (B) Si2p core levels. The peak positions indicate that gold is present in metallic state. The fitting of Si2p spectrum reveals siloxane to be the major component.

Figure 4.12 is the FTIR spectra of pure ODS solution and of the same solution with gold nanoparticles after the reaction. The pure ODS spectrum showed prominent peaks at ~ 2150 cm^{-1}, 2927 cm^{-1} and 2858 cm^{-1} corresponding to Si-H stretching, CH_2 asymmetric and CH_2 symmetric stretching vibrations of the groups present in CH_3-$(CH_2)_{17}$-SiH_3, ODS molecules. Another peak centered at ~928 cm^{-1} could be assigned to the Si-O stretch of the silanol group, arising due to the partial hydrolysis of the Si-H group on exposure to the atmosphere. The Si-H and Si-OH peaks at 2150 cm^{-1} and 928 cm^{-1} from ODS disappear after the reaction with gold chloride, and instead a new

peak appears at 1020 cm^{-1}. This peak originates from the stretching mode of the Si-O-Si group.[117] This alteration in the peaks suggests that during the reaction, the Si-H group in ODS oxidized to Si-O-Si. The transformation takes place by hydrolysis of silane to form silanol, followed by the polycondensation of these silanol groups to form siloxane (Figure 4.13).

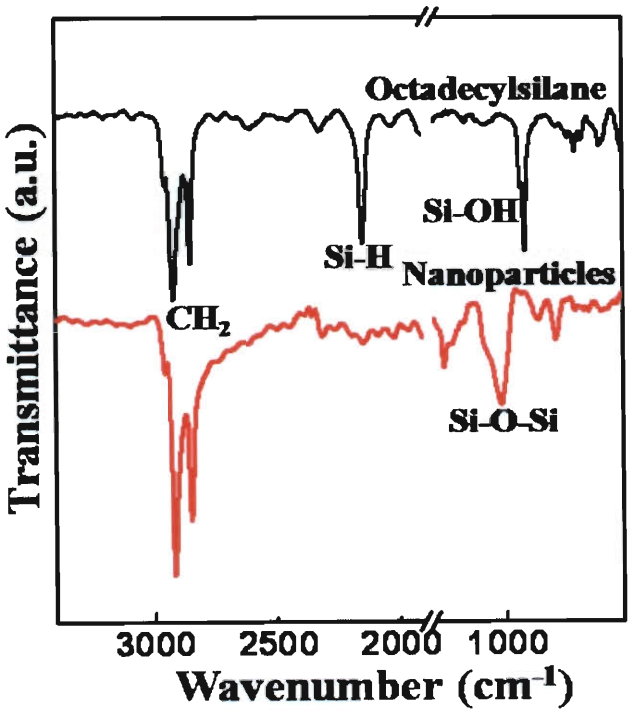

Figure 4.12 FTIR spectra obtained from pure ODS and the nanoparticles indicating the transformation of Si-H and Si-OH groups in ODS to Si-O-Si after the reaction.

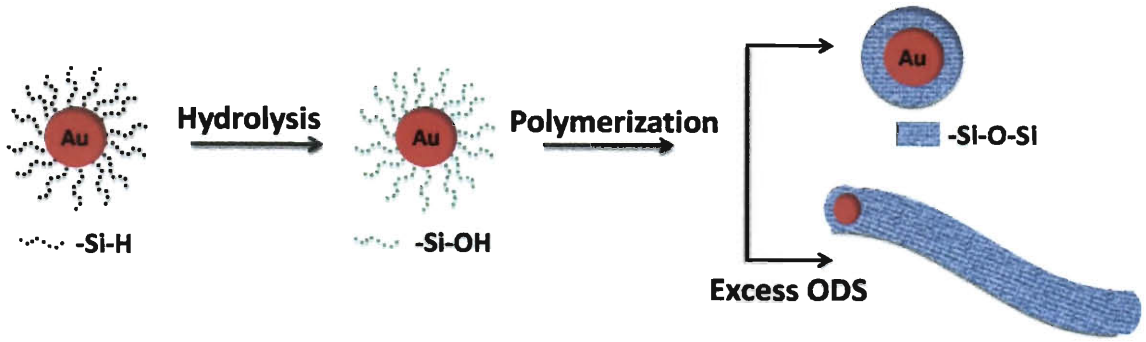

Figure 4.13 Schematic of the synthesis mechanism.

It is evident from the XPS and FTIR studies that the Si-H group present in ODS reduces the gold ions to metallic nanoparticles and concurrently, itself undergoes oxidation, followed by polymerization to form Si-O-Si. This polymerization mechanism has been pursued previously to form super hydrophobic siloxane sheets using octadecyltrichlorosilane,[64] silicone naofilaments using trichloromethylsilane[62] and siloxane nanofilaments and microspheres using ocadecylsilane.[65, 66] The reduction of metal salts by hydrosilanes is also well-studied in literature. Fukushima et al. have used polysilanes (poly-methylphenylsilane) to reduce silver, gold and palladium salts dissolved in alcohol.[109] They have further supported this mechanism by the relative reduction potentials of metal salts and silanes. They have calculated the reduction potential of polysilanes to range between 0.34 to 0.54 V.[109] Thus, it can easily reduce gold (1.50 V) and silver (0.80 V) both of which have a higher reduction potential. It is also well-established that during the metal-catalyzed hydrosilylation of alkenes, the hydrosilanes reduce the metal catalysts to colloidal metal particles.[110] After the reduction of metal ions by ODS, the further formation of a siloxane shell around these as-reduced nanoparticles involves the formation of weak Au-Si bonds between the metal nanoparticle surface and the free, unattached silane groups. These bonds easily get

hydrolyzed to silanol groups which undergo polycondensation to form a siloxane coating around the nanoparticles.[65] Thus, the metal nanoparticles act as both a catalyst for the polymerization of silane and as a template for the formation of the nanostructures. As confirmed by the TEM and SEM studies, the siloxane coating sterically stabilizes the metal nanoparticles, thereby preventing aggregation and leading to the formation the nanostructures.

4.4 Conclusions

The simultaneous utilization of silane properties, its ability to reduce metal salts and its propensity to polymerize to siloxane, has opened a new one-step route for synthesizing various metal-siloxane nanostructures. The synthesis takes place at room temperature and furthermore does not require pre-formed nanoparticles to catalyze the polymerization of alkysilanes. In-situ formed metal nanoparticles act a template for the formation of metal core-siloxane shell nanoparticles and siloxane nanowires, depending upon the relative concentration of octadecylsilane and metal salt. These hybrid nanostructures are potential candidates for catalysis, surface enhanced Raman spectroscopy and various other optoelectronic applications.

Chapter 5

In-situ synthesis of catalytic metal nanoparticle-PDMS membranes by thermal decomposition process

5.1 Introduction

This chapter pursues an alternative methodology, different from that reported in Chapter 2, to form metal nanoparticle embedded composites. Nanoparticles of various transition elements such as palladium, iron, and nickel were synthesized in-situ in the PDMS matrix by thermal decomposition of their corresponding acetylacetonate salts. PDMS membranes with palladium nanoparticles can be used as catalytic membrane reactors and have been tested for catalytic activity in ethylene hydrogenation.

Though a variety of polymer nanocomposites can be formed by thermal decomposition process, a major impediment is the degradation of polymers at high temperatures. Further constraints can be posed by the limited solubility of the metal salt in the polymer, the low solubility of the metal salt and polymer in the common solvent and the inability of the polymer to polymerize in the presence of metal salt. The good thermal and mechanical stability of PDMS (~ 400°C) and its ability to dissolve in organic solvents helps in overcoming these detriments.

5.2 Materials and Methods

To synthesize the nanocomposites, PDMS elastomer (Sylgard 184, Dow Corning) was used as received. The polymer kit contains the PDMS elastomer and the curing agent which were mixed in the weight ratio of 10:1 and then degassed under vacuum to remove entrapped air bubbles. All the other chemicals were purchased from Sigma Aldrich.

Metal acetylacetonates were the chosen precursors; they were preferred over carbonyls or fatty acids due to their lower decomposition temperature. 0.1M solution of palladium acetylacetonate [$Pd(acac)_2$] was prepared in methylene chloride. 10 ml was this solution was added to 5 g PDMS which would finally result in 2 wt% palladium content after decomposition. The amount of salt solution added was varied to give films with different metal content. The solution concentration was kept at $5x10^{-3}$M and 10^{-3}M for iron acetylacetonate [$Fe(acac)_2$] and nickel acetylacetonate [$Ni(acac)_2$] respectively. These concentrations are lower than that used for palladium due the limited solubility of the metal salts in the solvent. 5ml of each of these solutions was added to 10g PDMS, which was then cast on glass slides and cured at room temperature under vacuum. The solvent was allowed to completely evaporate from the films. The as-cured films were then heated at 350°C for an hour. An inert atmosphere (argon-15% hydrogen) was maintained during heating to prevent the oxidation of metal. A visible color change was seen in all the films indicating the formation of nanoparticles and further characterization was carried out.

Detailed morphological analysis was carried out using transmission electron microscopy (JEOL 2010). Imaging was done at 100 kV on drop casted samples prepared on carbon coated copper grids. The crystalline nature of the products was determined by X-ray diffractometer (Rigaku D/Max Ultima II) operated at 40 kV and equipped with a CuKα radiation source. X-ray photoelectron spectroscopy (XPS) studies ware performed by a spectrophotometer (PHI Quantera SXM) using a monochromatic Al Kα radiation (1486.6 eV). Thermogravimetric (TGA, Seteram Labsys TG–DTA) analysis of the membranes was carried out from room temperature to 800°C in nitrogen atmosphere at a

heating rate of 10 °C·min-1. The catalytic activity was studied through a continuous flow, fixed-bed microreactor system equipped with an on-line GC-MS product analysis.

5.3 Results and Discussion

This section pertains to the characterization results of the nanocomposites using various analysis techniques. After a detailed discussion of these results, the chapter proceeds towards the application of the Pd-PDMS nanocomposites for catalysis with ethylene hydrogenation as a model reaction.

5.3.1 Palladium-PDMS Nanocomposite

Figure 5.1 is the photograph of a pure PDMS film and PDMS film containing $[Pd(acac)_2]$ before and after the heat treatment. Pure PDMS film is transparent but after the addition of metal salt, it takes the color of the salt and turns yellow. There is an evident color change (to black) after heating, a strong visual indication of the formation of palladium particles in the film.

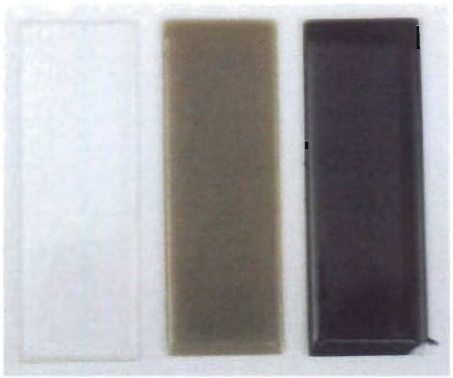

Figure 5.1 Photograph of pure transparent PDMS film, Pd-PDMS film before heating and Pd-PDMS film after heating with evident color changes.

The nanoparticles were extracted from the film by swelling the film using diisopropylamine. The polymer film was immersed in the solvent after cutting into very small pieces using a blade. PDMS tends to swell in diisopropylamine and after extended time, disintegrates completely. At this stage, the mixture of solvent and polymer was centrifuged repeatedly in excess of diisopropylamine, leading to the separation of nanoparticles at the bottom which were then analyzed using TEM to determine their shape and size. TEM micrographs (Figure 5.2) reveal non-aggregated nanoparticles which are spherical in nature with the shape and size being widely uniform. The size distribution histogram obtained from the TEM images shows the average particle diameter to lie in the range of 3-6nm (Figure 5.3). The formation of nanoparticles is agreement with the report by Esumi et al., where in the course of a detailed study on the decomposition of $Pd(acac)_2$ in various organic solvents, they have shown the successful synthesis palladium nanoparticles in the diameter range of 8-10 nm.[118] The crystalline nature of the nanoparticles formed was determined by XRD studies of the Pd-PDMS films. The peaks in the XRD pattern (Figure 5.4) can be indexed corresponding to the {111}, {200} and {220} reflections from fcc palladium (JCPD #00-005-0681), thereby conclusively showing the formation of crystalline palladium nanoparticles.

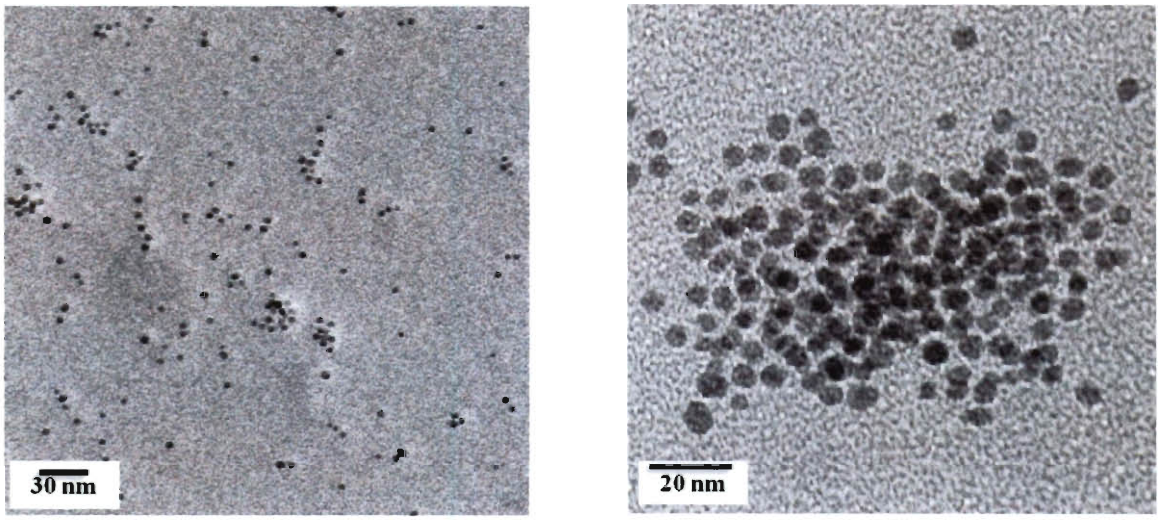

Figure 5.2 TEM images of palladium nanoparticles formed in the PDMS matrix.

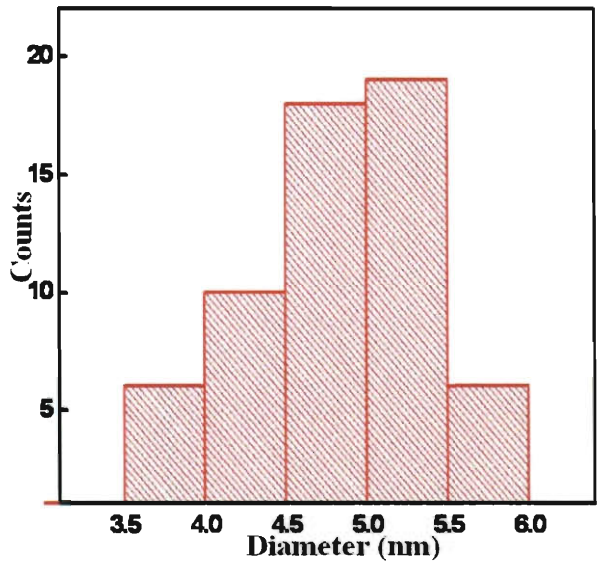

Figure 5.3 Size distribution obtained using TEM micrographs of palladium nanoparticles.

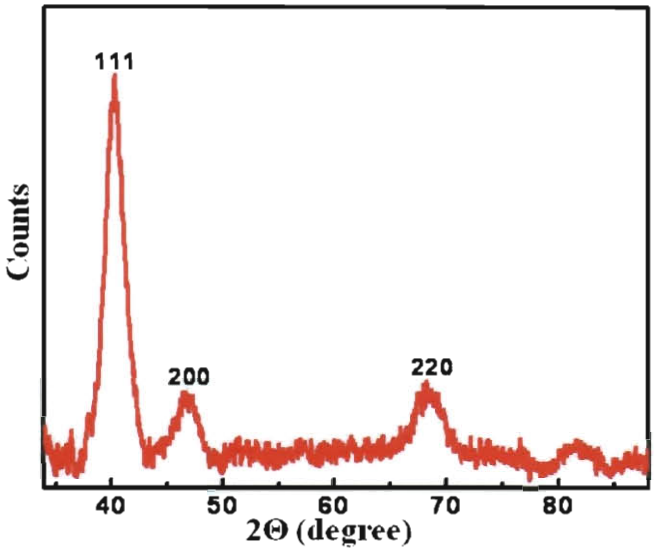

Figure 5.4 XRD pattern confirming the formation of crystalline fcc palladium nanoparticles.

The chemical state of the metal and its interaction with the matrix were analyzed using XPS. The general survey scan showed the presence of C1s, Si2p, O1s and Pd3d core levels. The Gaussian-fitted XPS spectrum for palladium is shown Figure 5.5(A). Binding energy of 284.5eV for adventitious carbon (C1s) was used as the internal standard. Spin-orbital coupling effect results in the splitting of the 3d emission from palladium into two discrete peaks centered at 336 eV and 341.4 eV, which correspond to $3d_{5/2}$ and $3d_{3/2}$ core levels of metallic palladium.[119] As seen in Figure 5.5(B), the Si2p peak originating from PDMS is centered at 102.2 eV which is same as that for pure PDMS.[120] This observation eliminates the possibility of any significant chemical interaction between the palladium nanoparticles and the surrounding PDMS matrix.

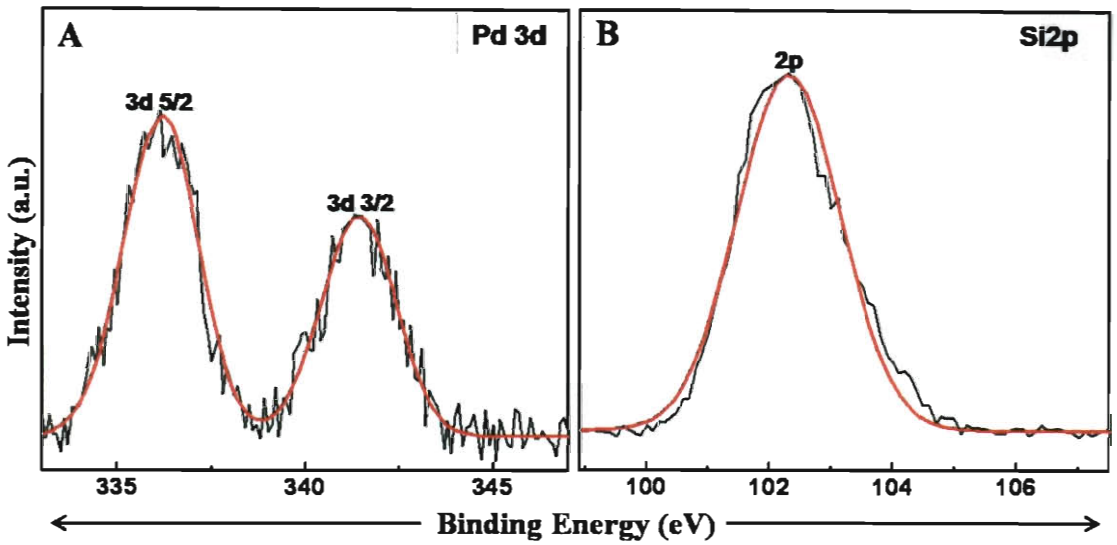

Figure 5.5 XPS spectra showing the binding energies of (A) Pd3d and (B) Si2p core levels. The peak positions in Pd spectrum correspond to that of its metallic state.

5.3.2 Nickel-PDMS Nanocomposite

Similar to palladium nanoparticles, nickel nanoparticles were also formed in the PDMS matrix. The unheated film has a light green color due to the presence of $[Ni(acac)_2]$. The color transforms to light brown after the formation of nickel nanoparticles on annealing the film (Figure 5.6). The extracted nanoparticles were imaged using TEM. TEM results confirm the formation of discrete nanoparticles in the polymer matrix as seen in Figure 5.7. Due to the low concentration of nanoparticles and because of the fact that they are embedded in the matrix, it was not possible to obtain the information on their crystalline nature using XRD. But as a support, EDS spectrum was obtained from these extracted nanoparticles (Figure 5.8). The peaks in the spectrum confirm the presence of nickel in the nanoparticles.

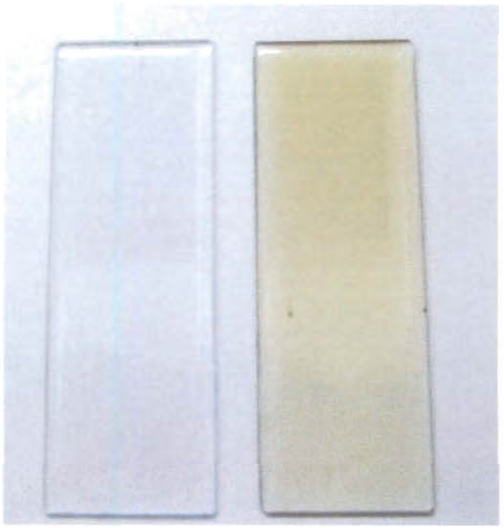

Figure 5.6 Photograph of Ni-PDMS film before and after the heat treatment. The color changes on the formation of nickel nanoparticles.

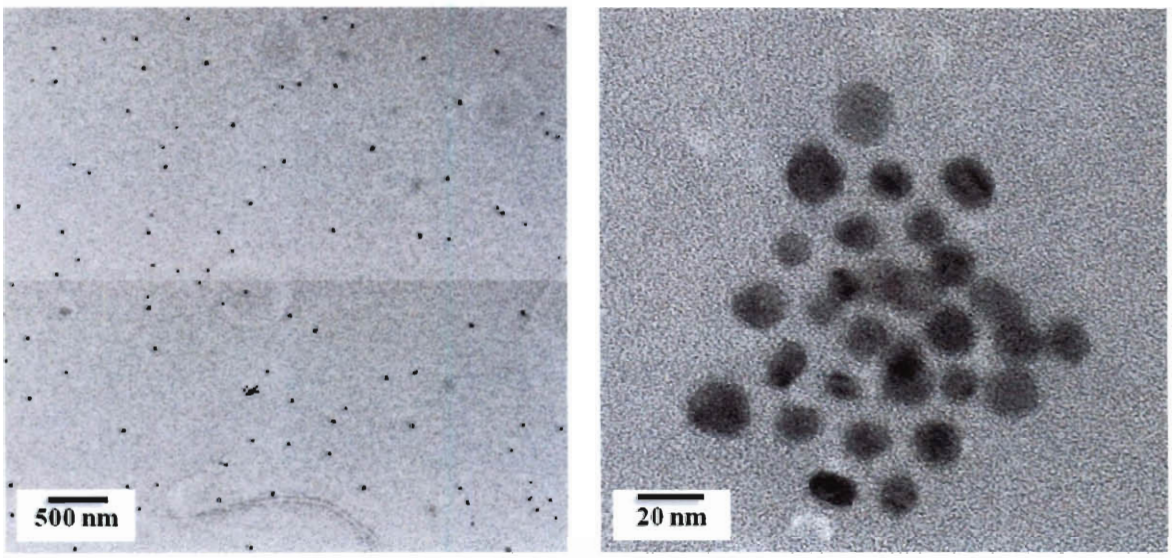

Figure 5.7 TEM images of nickel nanoparticles formed in the PDMS matrix.

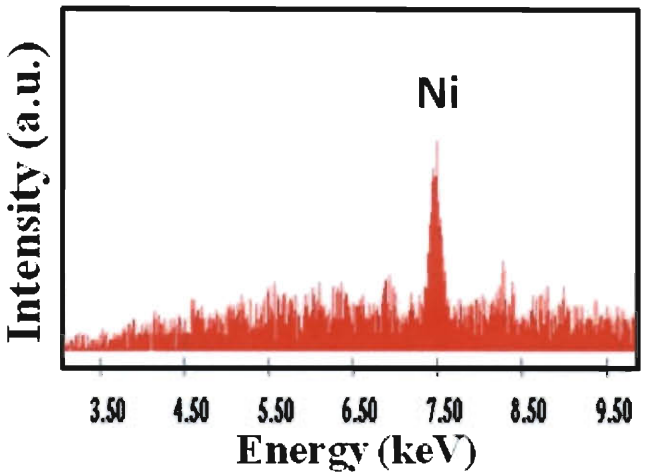

Figure 5.8 EDS spectrum confirming the presence of nickel.

5.3.3 Iron-PDMS Nanocomposite

On heating the films containing [$Fe(acac)_2$], the color changes to dark brown as shown in Figure 5.9. Unlike palladium and nickel, iron nanoparticles did not appear as discrete particles under TEM studies. Instead, the iron nanoparticles were agglomerated in clusters sizing more than 100 nm (Figure 5.10). This agglomeration is possibly caused by the magnetic nature of iron nanoparticles which tends to bring them closer. EDS studies were carried out on these extracted nanoparticles. A strong iron signal can be seen in Figure 5.11 which confirms that the particles are composed of iron.

Figure 5.9 Photograph of Fe-PDMS film before and after the heat treatment. The color change indicates the formation of iron nanoparticles.

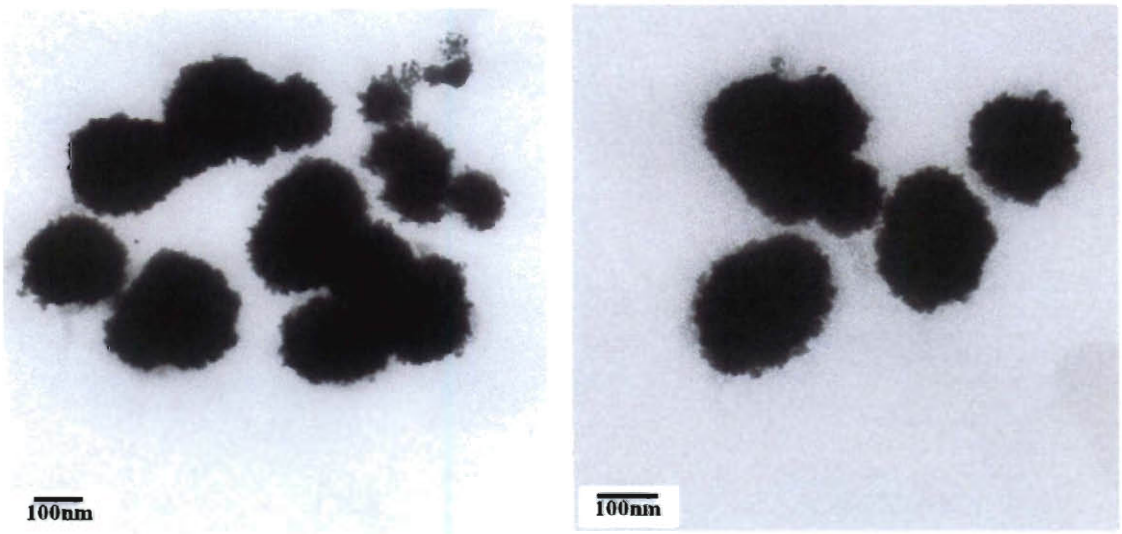

Figure 5.10 TEM images of iron nanoparticles formed in the PDMS matrix.

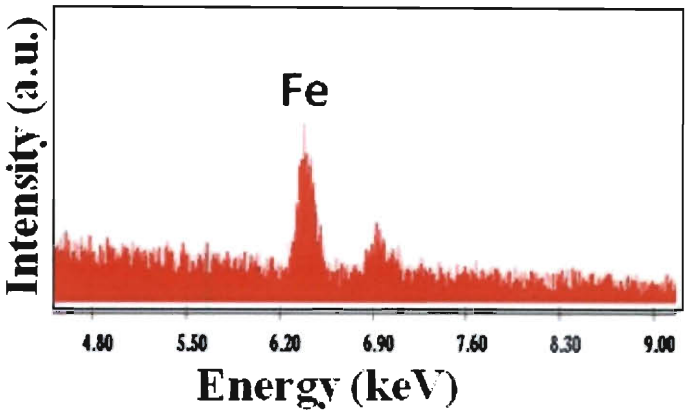

Figure 5.11 EDS spectrum confirming the presence of iron.

5.3.4 Catalytic Properties

As palladium nanoparticles are well-established for hydrogenation activity, the Pd-PDMS membranes were tested for the hydrogenation reaction of ethylene. To determine the activation temperature, thermogravimetric analysis was carried out. The starting sample weight was 10mg and final weight loss was found to be 45 % as inferred by the data in Figure 5.12. In agreement with the previously reported studies, the decomposition started just below 400 °C. For example, Jana et al. found the initial decomposition temperature for pure PDMS to be 363 °C.[121] Consequently, the activation of membrane catalysts was carried out at 350 °C in hydrogen atmosphere. In all experiments, 10 mg of membrane (cut to ~1 mm^2 pieces) was mixed with 1 g of inert Stober silica, yielding a catalyst bed volume large enough to ensure adequate contact between the gaseous reactants and the catalyst. The catalytically inactive, monodispersed silica particles (170nm) were synthesized using the well-known Stober procedure.[122] Blank experiments were done with pure SiO_2 nanoparticles and pure PDMS membranes to determine the presence of any background reaction. No activity was observed in these control experiments, thereby making silica nanoparticles an appropriate diluting matrix

for the PDMS membranes. Membranes mixed with silica were placed into an 8 mm internal diameter glass tube and tested at atmospheric pressure. The tubular reactor was placed in a furnace equipped with a temperature controller and the catalyst was subjected to reductive treatment prior to the hydrogenation reaction by annealing it at 623 K in N_2 atmosphere and exposing it to a 30 cm^3 min^{-1} hydrogen flow for one hour at 760 Torr. Figure 5.13 shows a schematic diagram of the set-up used for catalytic measurements. The reactant gas used was a dry mixture of high-purity hydrogen, nitrogen and ethylene, set to 292.3 Torr, 438.5 Torr and 29.2 Torr at the flow rates of 20 $cm^3 \cdot min^{-1}$, 30 $cm^3 \cdot min^{-1}$ and 2 $cm^3 \cdot min^{-1}$ respectively. The flow rates were converted into volumes for room temperature (299 K) and standard pressure (760 Torr). All measurements were evaluated based on data obtained after a steady rate of 3% was achieved for ethylene to ethane conversion (not less than 30 min). All catalytic measurements were repeated at least five times and showed similar conversion rates. The turnover rate (TOR) of both pure PDMS and Pd-PDMS membranes increased with temperature in the studied ~40 K (264-305 K) temperature range. The turnover rates (TOR) were normalized to the number of surface atoms. The calculation of the turnover rates shown in Figure 5.14 was based on the surface Pd atom calculations found in the literature ($1.53 \cdot 10^{15}$ atoms$\cdot cm^{-2}$),[123] assuming that each Pd surface atom is an active site in the membrane and has a spherical geometry with 78.5 nm^2 of surface area accessible to the reactants.

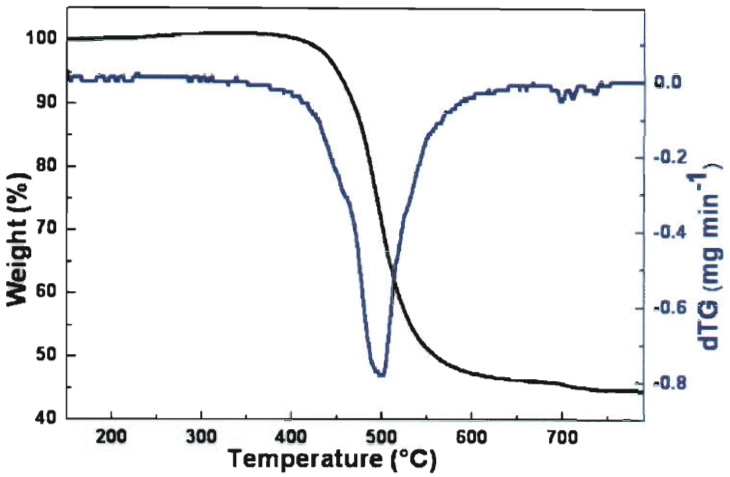

Figure 5.12 TGA measurement of PDMS membrane containing 2 wt% palladium. The degradation starts at about 400°C.

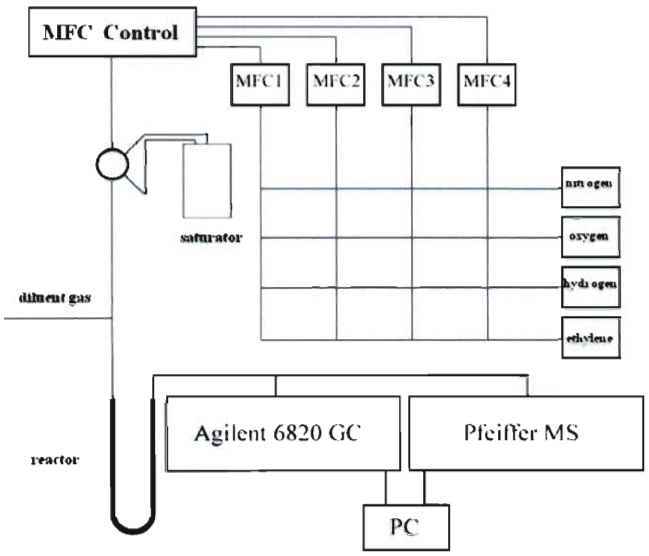

Figure 5.13 Schematic of the catalytic experiment set-up. (Courtesy: Robert Remias)

For the reaction kinetics, the apparent activation energy for 1 wt% Pd-PDMS and 2 wt% Pd-PDMS membranes was found to be 2.4 kcal·mol^{-1} and 2.3 kcal·mol^{-1} (Figure 5.14). The ethylene conversion on membranes containing 2 wt% palladium proved to be ~1.3 times higher relative to that of membranes loaded with 1 wt% Pd. This

effect could originate from the possible aggregation of Pd nanoparticles, leading to a non-proportional increase of the total catalyst surface available for reaction.

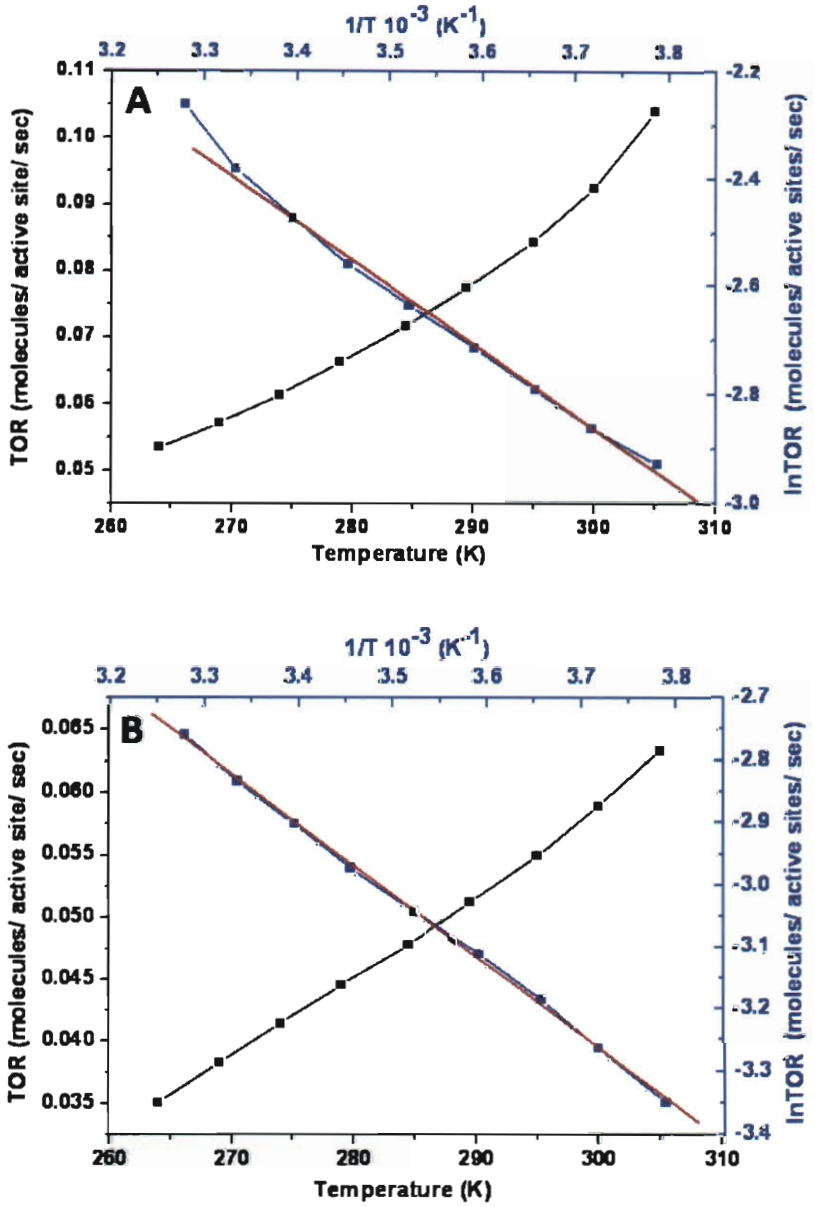

Figure 5.14 TOR and Activation energy of ethylene on (A) 1% Pd-PDMS and (B) 2% Pd-PDMS.

5.4 Conclusions

Metal nanoparticles were synthesized in the PDMS matrix by taking advantage of the low decomposition temperature of metal acetylacetonate salts and the good thermal stability of polydimethylsiloxane (PDMS). Using this thermal decomposition technique, various metal nanoparticles such as palladium, iron and nickel can be synthesized in-situ in the polymeric membrane. This synthesis route results in relatively monodisperse nanoparticles with a narrow particle size distribution. In addition, the composite films are robust and mechanically stable, making them attractive for a range of applications; palladium nanoparticles make the membranes catalytically active towards ethylene hydrogenation.

Chapter 6

Flexible CNT-Cu_2O hybrid electrodes for Li-ion batteries

6.1 Introduction

Improvements in Li-ion battery technology have been driven strongly by microelectronics that require lighter, thinner and higher capacity batteries, particularly for portable devices.[67-69] There is a particular interest in fabricating thin, flexible batteries with widespread applications in rolled-up displays, implantable devices and smart cards.[97, 124] One of the major challenges in the development of these flexible batteries is to achieve a mechanically robust, light-weight system without compromising on electrochemical characteristics. This necessitates improvements in structural, electrochemical and design aspects of the battery through innovations in constituent electrode, electrolyte and separator materials.[125, 126]

Motivated by these challenges, a novel strategy has been developed for fabricating flexible, high capacity anodes for Li-ion batteries. Cu_2O was electrodeposited on aligned CVD grown-CNTs which were on a stainless steel substrate. After drying, the oxide-coated CNTs were embedded in a porous PVDF-HFP (Poly(vinylidene fluoride-hexafluoropropylene))-SiO_2 polymer electrolyte membrane prepared by phase inversion technique and peeled from the substrate. PVDF-HFP is a widely chosen polymer-electrolyte due to its good electrochemical and mechanical stability and high ionic conductivity.[127] Nanosized inorganic inclusions can enhance the mechanical strength and ionic conductivity of the polymer membrane besides improving its cycling ability and interfacial lithium stability.[128] The membrane was made porous to increase its uptake of the liquid electrolyte which consequently enhances its ionic conductivity.[129]

This configuration -electrode embedded in polymer separator- obviates the need of a binder and external current collector, resulting in a highly desirable lightweight flexible geometry. CNTs provide a highly conductive physical framework for the deposition of high capacity copper oxide. Introduction of copper oxide helps in mitigating the issue of low capacity observed in pure CNTs, and the hybrid shows an improvement in discharge capacity over pure CNTs.

6.2 Materials and Methods

Stainless steel (Alfa Aesar Type 304, Fe:Cr:Ni: 70:19:11 wt%) was used a substrate for the growth of CNTs. Li metal foil (99.9%, Sigma Aldrich) was used as a counter electrode. PVDF-HFP (Kynar 2801) was the chosen polymer electrolyte and fumed silica (CAB-O-SIL TS 530, Cabot Corporation) was used as the filler for the polymer electrolyte composite. Fumed silica is pre-treated with hexamethyldisilazane making the particle surface hydrophobic and thereby increasing its compatibility with PVDF which itself is a hydrophobic polymer.

The flexible electrode-electrolyte system was fabricated using a combination of CVD and electrodeposition techniques. The schematic in Figure 6.1 delineates the synthesis procedure. Aligned CNTs were obtained on a steel substrate by the chemical vapor deposition (CVD) process and were then coated with Cu_2O using electrodeposition. The as-formed hybrid structure was embedded in a SiO_2-PVDF-HFP polymer electrolyte matrix in which porosity was introduced by phase inversion. The composite film was then peeled from the substrate to obtain the free-standing, flexible electrode. After sputter-coating a 100nm gold current collector, the films were tested against Li-metal foil for electrochemical activity.

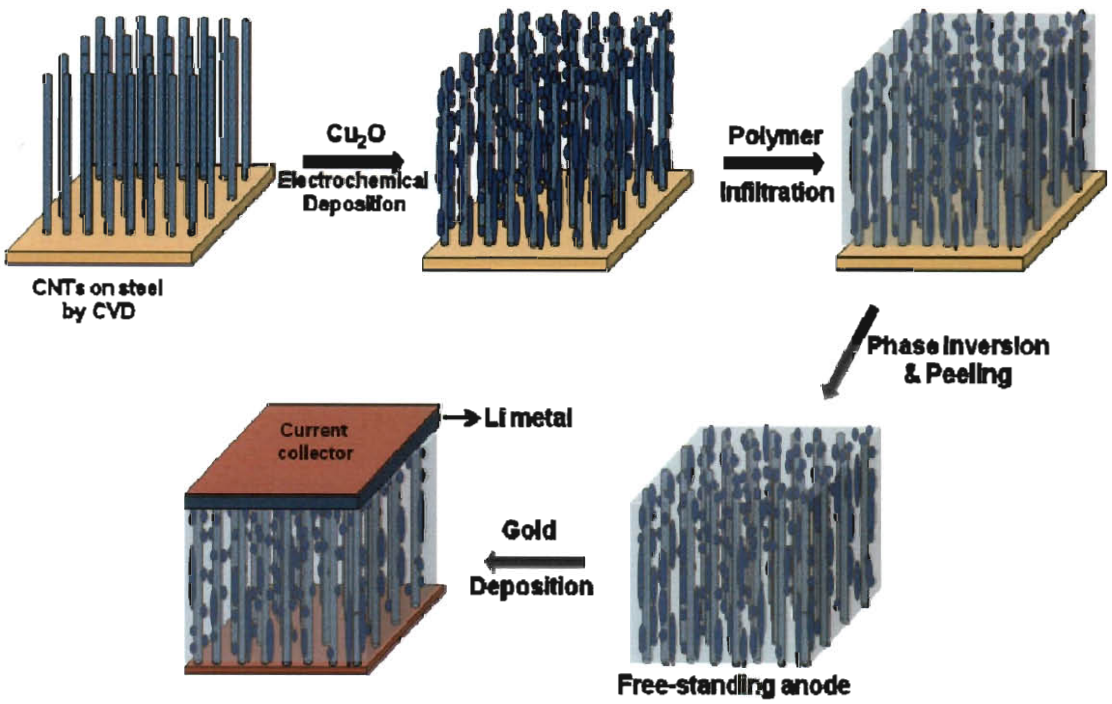

Figure 6.1 Fabrication schematic for Cu_2O coated CNT electrodes. The CVD-grown CNTs were coated with copper oxide using electrodeposition. After polymer infiltration, the CNTs were peeled off the substrate to obtain free-standing electrodes on which a thin layer of gold was sputter-coated.

6.2.1 CNT Synthesis

Multi-walled CNTs were grown by the CVD process on a steel substrate having pre-deposited catalyst.[86] The steel substrate (1.8 cm diameter) was coated with 10 nm aluminum followed by 1.5 nm iron using an e-beam evaporator. A temperature-controlled furnace with a 3 inch quartz tube was used for the growth. Aligned CNTs~200 μm were obtained through the decomposition of ethylene (100sccm) at 775°C for 15 min, in the presence of a trace amount of water vapor. An inert atmosphere was maintained in the furnace throughout by a constant flow (1.3 slm) of Ar/15%H_2.

6.2.2 Copper Oxide Electrodeposition

The as-grown CNTs were used for cathodic electrodeposition of copper oxide using 0.05M $CuSO_4$ solution complexed with equimolar citric acid.[130] The pH of the solution was maintained at 9 by using 1M NaOH. The electrodeposition was carried out at room temperature using a potentiostat (Autolab PGSTAT302N) and a conventional three electrode set-up consisting of a saturated Ag/AgCl reference electrode and a platinum counter electrode as shown in Figure 6.2. Forty deposition cycles were carried out at a potential of 1.05V (SCE) with a 4 second pulse width at an interval of 10 seconds between pulses. Figure 6.3 shows a representative current vs. time profile of the electrodeposition process. The CNTs were washed well with DI water after deposition and dried in a vacuum oven for a day.

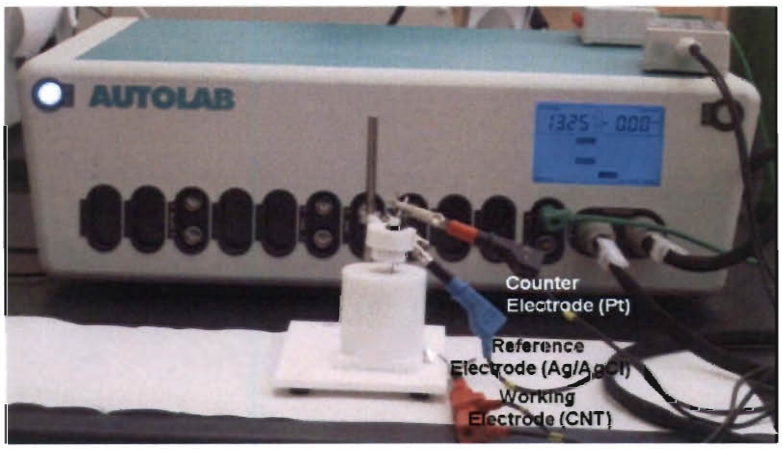

Figure 6.2 Photograph of the three electrode instrumental set-up used for electrodeposition.

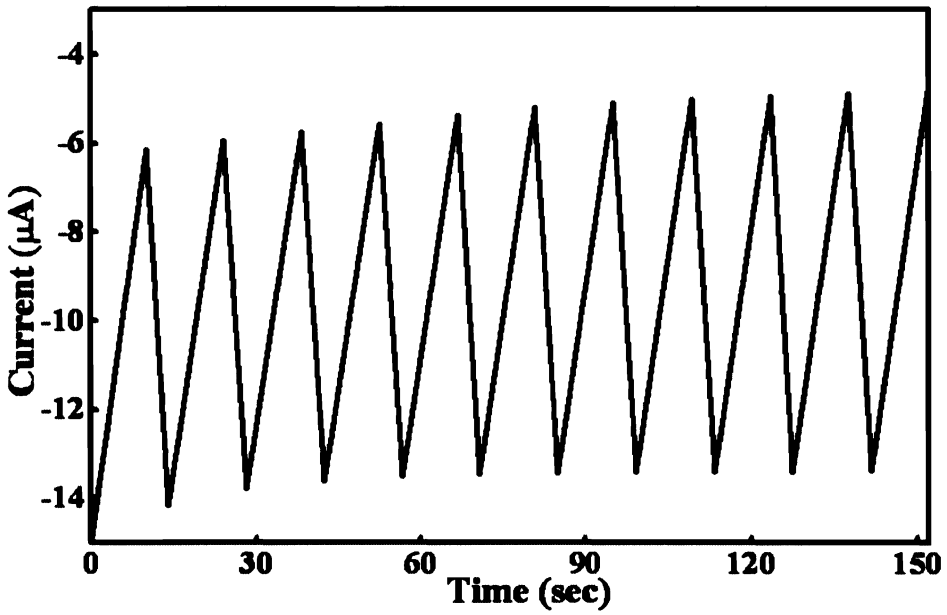

Figure 6.3 Current vs. Time curve for the cathodic deposition of Cu_2O. The deposition is done in pulses of 4 sec followed by 10 sec of open circuit.

6.2.3 Fabrication of CNT-Cu_2O-PVDF electrode-electrolyte

To prepare the flexible electrode, PVDF-HFP and SiO_2 were dissolved in 4:1 weight ratio in a 10% by weight PVDF-HFP solution in acetone.[128] Porous membranes were obtained by dipping the polymer composite with the embedded CNT-copper oxide in a water bath and drying it under vacuum for 24 hours.[131] The polymer membranes embedded with CNT-copper oxide were peeled from the substrate to obtain free-standing films which were characterized and then tested as an anode material after sputter-coating with 100 nm of gold for good electrical contact.

6.2.4 Characterization and Testing Techniques

The phase and crystalline nature of the electrodeposited copper oxide were determined using X-ray diffractometer (XRD - Rigaku D/Max Ultima II) operated at 40kV. Morphological analysis was carried out using a scanning electron microscope

6.3.1 Characterization

CNTs grown on the steel substrate were analyzed by SEM and HRTEM. Figures 6.5 (A) and (B) are the SEM images of pure CNTs grown on steel by the CVD process. The as-grown CNTs are well-aligned with a length of up to 300 μm. The high magnification image of CNTs shows ample free volume present in between the CNTs. High-resolution TEM images reveal the nanotubes to be multi-walled as seen in Figures 6.5 (C) and (D). Figures 6.6 (A) and (B) show the changes to the surfaces of CNTs upon electrodeposition with copper oxide. From these SEM images it can be seen that the alignment of CNTs was evidently maintained post-electrodeposition. The high magnification image reveals the formation of a uniform and almost continuous conformal coating of copper oxide on the CNTs. The EDS spectrum obtained from the coated CNTs clearly indicates the presence of copper on them (Figure 6.7).

XPS studies were conducted to further confirm the oxidation state of copper and to verify the formation of Cu_2O. Figure 6.9 shows the Cu2p core level spectrum recorded from the coated CNTs. The peak positions in the spectrum correspond to the binding energy of cuprous oxide. The spin-orbit coupling in copper results in two peaks centered at 933.1 and 953eV from the $2p_{3/2}$ and $2p_{1/2}$ core levels.[133] These XPS results, in conjunction with the XRD studies firmly establish the formation of a pure Cu_2O coating on the CNTs. After the detailed analysis of the as-formed coating, both pure CNTs and coated CNTs were embedded in the porous PVDF-HFP-SiO_2 membrane prepared by phase inversion.

Figure 6.10(A) shows the photographs of the pristine as-grown CNTs on the steel substrate with a very uniform growth all over the substrate and of the CNTs embedded in the porous polymer electrolyte membrane. Phase inversion results in a well-connected porous membrane after solvent extraction as seen from the SEM image in Figure 6.10(B). The polymer film embedded with CNTs was peeled from the substrate. The film possesses very good flexibility as evident from the photograph in Figure 6.10(C). Due to their excellent flexibility, the membranes remain mechanically robust even on bending and thereby result in structurally strong, free-standing electrodes. The presence of the polymer film also makes an external separator redundant and contributes towards weight reduction of the electrode.

performance. It gives a reversible specific capacity of 0.23 $mAhcm^{-2}$ in contrast to a significantly lower 0.11 $mAhcm^{-2}$ capacity achieved through pure CNTs. On a gravimetric basis, the hybrid and pure CNTs have a capacity of 305 $mAhg^{-1}$ and 115 $mAhg^{-1}$ respectively after 15 cycles. This three times enhancement in capacity can be attributed to the dual mechanism in operation: the contributions from both the CNTs and Cu_2O. The highly conductive core of the CNTs gives a good electrical contact and a better conductivity, and their high aspect ratio helps in achieving the percolation threshold at much lower weights. Also, their aligned structure provides an easily accessible, regular and porous path for the ions to diffuse and unlike traditional carbon materials used as binder like activated carbon, CNTs themselves act as active material. Although the good alignment assists in providing a high surface area for the Li-ion insertion/deinsertion in CNTs, they are limited by low capacity. The presence of copper oxide on the CNTs significantly improves their capacity by adding to the Li storage in the system. Unlike the classical Li-ion alloying and de-alloying mechanism present in CNTs, the reaction of Li-ion with copper oxide proceeds through Li insertion during the metal reduction, followed by its de-insertion during the oxidation process.[135] This conversion reaction can be represented as:

$$Cu_2O + 2Li^+ + 2e^- \longleftrightarrow 2Cu + Li_2O$$

Chapter 7

Conclusions and Future work

The focus of this thesis has been on the development of novel synthesis routes to fabricate nanoparticle-polymer composites and hybrids, tailored towards various applications such as antibacterial and catalytic membranes and advanced battery electrodes.

In chapter 3 the conception of a simple one-step method is discussed, wherein free-standing and flexible metal nanoparticle-PDMS films are formed. The dual functionality of the silane-containing curing agent in cross-linking PDMS while simultaneously reducing the metal salt eliminates the requirements for the use of external reducing agents. This method is found to be generic across several metal nanoparticles (Au, Ag, Pt). For the case of silver-PDMS nanocomposites, enhancements in mechanical and antibacterial properties are observed. Upon 1 day exposure, the nanocomposites inactivate 80% *E. coli* and 52% *B. subtilis* while no activity is seen for pure PDMS. Silver-PDMS also has a three times higher Young's modulus (1.7±0.2 MPa) as compared to the pure polymer (0.5±0.1 MPa). A recommended research direction would thus be to investigate the effect of filler content on the nanocomposite properties, through a unified approach of theoretical modeling and experimental measurements. Specifically, the response of optical and spectral properties of Au-PDMS nanocomposites to Au nanoparticle content and catalytic properties of Pt-PDMS nanocomposite membranes to Pt content would constitute important cases for metal-content property-relationship studies. Furthermore, there is a possibility to utilize this synthesis scheme towards synthesizing metal alloy nanoparticles in the polymer matrix. Therefore, co-reduction of

binary/ternary systems of metal salts to result in metal alloy nanocomposites is another recommended avenue for research.

In chapter 4, the synthesis scheme used in forming metal-PDMS nanocomposite has been extended to form metal-siloxane nanostructures. In this scheme, reduction of metal salts by silanes and the tendency of silanes to polymerize to siloxanes, results in metal (gold, silver) core-siloxane shell nanoparticles and siloxane nanowires. When the silane concentration is limited, core-shell structures emerge, whereas siloxane nanowires are formed when silane is in excess. As recommended future work, the core-shell nanoparticles could be transformed to hollow siloxane capsules by etching out the metal core. The benefits of a siloxane-based capsule are several fold, because siloxanes are biocompatible polymers they could be used to store enzymes, proteins and actives and used for drug-delivery applications *in vivo*. Hollow capsules with thin shells could be designed for selective diffusion of small molecules to the capsule interiors, thus making it feasible for the capsules to be used as micro reactors. Further investigations are recommended on the transition from zero-dimensional core-shell nanoparticles to one-dimensional nanowires, which can be carried out by systematically varying the relative concentration of metal-salts to silanes.

Chapter 5 discusses an alternative approach to synthesize PDMS nanocomposites embedded with transition metal nanoparticles (platinum, iron, nickel) by thermal decomposition of metal acetylacetonates in the polymer matrix. The synthesis of composite membranes containing two or more nanoparticles with multiple functionalities could bring out several commercially attractive applications and is another possible area of interest for future research.

Finally, Chapter 6 demonstrates the fabrication of flexible and free-standing CNT-Cu_2O-PVDF nanocomposites and their application as an electrode-electrolyte material for Li-ion batteries. Binder-free hybrid electrodes are obtained by coating CNTs conformally with Cu_2O via electrodeposition and subsequently embedding the resulting architecture into a porous PVDF-HFP-SiO_2 polymer-electrolyte membrane. The synergistic presence of high capacity transition metal oxides and conductive CNTs results in significant enhancements in reversible areal and gravimetric capacity over pure CNTs. Several parameters such as CNT length, areal density and electronic conductivity could have a significant impact on battery performance. Variation in these parameters can lead to a better performing electrode. As a future research initiative, it would be worthwhile to explore the effects of different filler types on the ionic conductivity of the resulting polymer separator. It would also be possible to surpass the state-of-art design and performance by depositing on the existing anode films a counter cathode such as $LiCoO_2$ that would result in a flexible battery with much coveted applications in areas such as microelectronics, defense and smart cards.

It is possible to develop other systems also using the same methodology as that adopted for CNT-Cu_2O hybrids. In one such initiative, tin sulfide has been electrodeposited on CNTs. Figure 7.1 shows the SEM images of SnS coated CNT and Figure 7.2 shows the XRD pattern which confirms the formation of crystalline SnS. This hybrid system can be tested and used for potential battery applications.

References

1. Ajayan, P. M.; Schadler, L. S.; Braun, P. V., Nanocomposite science and technology. **2003**.

2. Sulak, M. T.; Gokdogan, O.; Gulce, A.; Gulce, H., Amperometric glucose biosensor based on gold-deposited polyvinylferrocene film on pt electrode. *Biosensors & Bioelectronics* **2006,** 21, (9), 1719-1726.

3. Dire, S.; Babonneau, F.; Sanchez, C.; Livage, J., Sol-gel synthesis of siloxane oxide hybrid coatings [si(ch3)2o.Mox - m = si, ti, zr, al] with luminescent properties. *Journal of Materials Chemistry* **1992,** 2, (2), 239-244.

4. Chen, H.; Liu, X.; Muthuraman, H.; Zou, J. H.; Wang, J. H.; Dai, Q.; Huo, Q., Direct laser writing of microtunnels and reservoirs on nanocomposite materials. *Advanced Materials* **2006,** 18, (21), 2876-2879.

5. Ozdemir, S. S.; Buonomenna, M. G.; Drioli, E., Catalytic polymeric membranes: Preparation and application. *Applied Catalysis a-General* **2006,** 307, (2), 167-183.

6. Bozlar, M.; He, D. L.; Bai, J. B.; Chalopin, Y.; Mingo, N.; Volz, S., Carbon nanotube microarchitectures for enhanced thermal conduction at ultra low mass fraction in polymer composites. *Advanced Materials* 22, (14), 1654-1958

7. Ci, L.; Suhr, J.; Pushparaj, V.; Zhang, X.; Ajayan, P. M., Continuous carbon nanotube reinforced composites. *Nano Letters* **2008,** 8, (9), 2762-2766.

8. Schlemmer, D.; Angelica, R. S.; Sales, M. J. A., Morphological and thermomechanical characterization of thermoplastic starch/montmorillonite nanocomposites. *Composite Structures* 92, (9), 2066-2070.

9. Kim, I. H.; Jeong, Y. G., Polylactide/exfoliated graphite nanocomposites with enhanced thermal stability, mechanical modulus, and electrical conductivity. *Journal of*

Polymer Science Part B-Polymer Physics 48, (8), 850-858.

10. Kim, H.; Abdala, A. A.; Macosko, C. W., Graphene/polymer nanocomposites. *Macromolecules* 43, (16), 6515-6530.

11. Coleman, J. N.; Khan, U.; Gun'ko, Y. K., Mechanical reinforcement of polymers using carbon nanotubes. *Advanced Materials* **2006,** 18, (6), 689-706.

12. Brandao, L.; Madeira, L. M.; Mendes, A. M., Mass transport on composite dense pdms membranes with palladium nanoclusters. *Journal of Membrane Science* **2007,** 288, (1-2), 112-122.

13. Uhlenhaut, D. I.; Smith, P.; Caseri, W., Color switching in gold - polysiloxane elastomeric nanocomposites. *Advanced Materials* **2006,** 18, (13), 1653-1956

14. Lee, K. S.; El-Sayed, M. A., Gold and silver nanoparticles in sensing and imaging: Sensitivity of plasmon response to size, shape, and metal composition. *Journal of Physical Chemistry B* **2006,** 110, 19220-19225.

15. Zhao, Y.; Jiang, Y. J.; Fang, Y., Spectroscopy property of ag nanoparticles. *Spectrochimica Acta Part a-Molecular and Biomolecular Spectroscopy* **2006,** 65, (5), 1003-1006.

16. Khlebtsov, B. N.; Khlebtsov, N. G., Multipole plasmons in metal nanorods: Scaling properties and dependence on particle size, shape, orientation, and dielectric environment. *Journal of Physical Chemistry C* **2007,** 111, (31), 11516-11527.

17. Shipway, A. N.; Katz, E.; Willner, I., Nanoparticle arrays on surfaces for electronic, optical, and sensor applications. *Chemphyschem* **2000,** 1, (1), 18-52.

18. Caruso, F., Nanoengineering of particle surfaces. *Advanced Materials* **2001,** 13, (1), 11-22.

19. Fritsch, D.; Kuhr, K.; Mackenzie, K.; Kopinke, F. D., Hydrodechlorination of chloroorganic compounds in ground water by palladium catalysts - part 1. Development of polymer-based catalysts and membrane reactor tests. *Catalysis Today* **2003,** 82, (1-4), 105-118.

20. Perez-Juste, J.; Pastoriza-Santos, I.; Liz-Marzan, L. M.; Mulvaney, P., Gold nanorods: Synthesis, characterization and applications. *Coordination Chemistry Reviews* **2005,** 249, (17-18), 1870-1901.

21. Joshi, R. K.; Krishnan, S.; Yoshimura, M.; Kumar, A., Pd nanoparticles and thin films for room temperature hydrogen sensor. *Nanoscale Research Letters* **2009,** 4, (10), 1191-1196.

22. Yuan, Y. Y.; Liu, X. Q.; Wang, Y. C.; Wang, J., Gold nanoparticles stabilized by thermosensitive diblock copolymers of poly(ethylene glycol) and polyphosphoester. *Langmuir* **2009,** 25, (17), 10298-10304.

23. Thanh, N. T. K.; Green, L. A. W., Functionalisation of nanoparticles for biomedical applications. *Nano Today* 5, (3), 213-230.

24. Mittal, K. L.; Pizzi, A., Handbook of sealant technology. *CRC Press* **2009**, 13-14.

25. Colas, A., Silicones: Preparation, properties and performance. www.dowcorning.com **2005**.

26. McDonald, J. C.; Whitesides, G. M., Poly(dimethylsiloxane) as a material for fabricating microfluidic devices. *Accounts of Chemical Research* **2002,** 35, (7), 491-499.

27. Whitesides, G. M., The origins and the future of microfluidics. *Nature* **2006,** 442, (7101), 368-373.

28. Lee, J. N.; Park, C.; Whitesides, G. M., Solvent compatibility of poly(dimethylsiloxane)-based microfluidic devices. *Analytical Chemistry* **2003,** 75, (23), 6544-6554.

29. Zhang, Q.; Xu, J. J.; Liu, Y.; Chen, H. Y., In-situ synthesis of poly(dimethylsiloxane)-gold nanoparticles composite films and its application in microfluidic systems. *Lab on a Chip* **2008,** 8, (2), 352-357.

30. Luo, C. X.; Fu, Q.; Li, H.; Xu, L. P.; Sun, M. H.; Ouyang, Q.; Chen, Y.; Ji, H., Pdms microfludic device for optical detection of protein immunoassay using gold nanoparticles. *Lab on a Chip* **2005,** 5, (7), 726-729.

31. Kim, J. H.; Won, J.; Kang, Y. S., Olefin-induced dissolution of silver salts physically dispersed in inert polymers and their application to olefin/paraffin separation. *Journal of Membrane Science* **2004,** 241, (2), 403-407.

32. Park, J. H.; Lim, Y. T.; Park, O. O.; Kim, J. K.; Yu, J. W.; Kim, Y. C., Polymer/gold nanoparticle nanocomposite light-emitting diodes: Enhancement of electroluminescence stability and quantum efficiency of blue-light-emitting polymers. *Chemistry of Materials* **2004,** 16, (4), 688-692.

33. Kim, J. A.; Lee, S. H.; Park, H.; Kim, J. H.; Park, T. H., Microheater based on magnetic nanoparticle embedded pdms. *Nanotechnology* 21, (16), 165102.

34. Giesfeldt, K. S.; Connatser, R. M.; De Jesus, M. A.; Lavrik, N. V.; Dutta, P.; Sepaniak, M. J., Studies of the optical properties of metal-pliable polymer composite materials. *Applied Spectroscopy* **2003,** 57, (11), 1346-1352.

35. Kreutz, E. W.; Frerichs, H.; Stricker, J.; Wesner, D. A., Processing of polymer surfaces by laser radiation. *Nuclear Instruments & Methods in Physics Research Section*

(SEM - FEI Quanta 400) operated at 20 kV and a high-resolution transmission electron microscope (JEOL 2100) operated at 200 kV. X-ray photoelectron spectroscopy measurements (XPS - PHI Quantera SXM) were carried out using Al K_α radiation (1486.6 eV) incident at an angle of 45° to the sample. For electrochemical measurements a Swagelok-type test cell (Figure 6.4) was assembled in an argon-filled glove box, with CNT/PVDF-HFP as the working electrode/separator, lithium metal foil as the counter/reference electrode and 1M $LiPF_6$ in 1:1 (v/v) solution of ethylene carbonate and dimethyl carbonate as the electrolyte. Galvanostatic charge-discharge testing was performed 45μA/cm^2 within a voltage window of 0.02 to 3 V using a battery analyzer (Arbin Instruments BT2010).

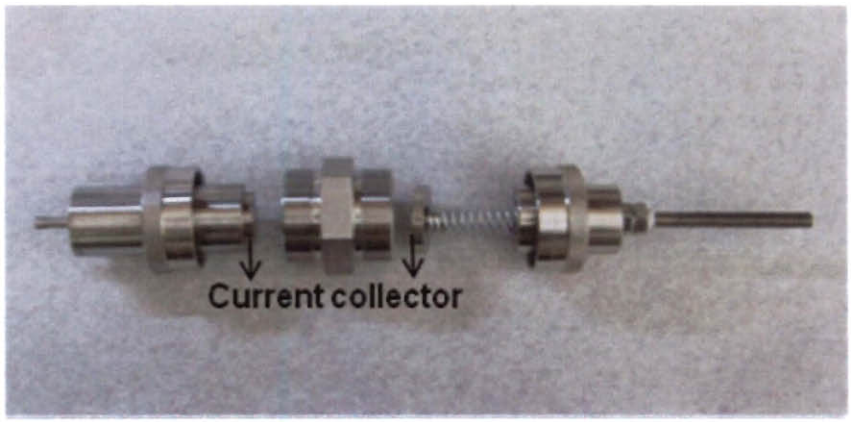

Figure 6.4 The custom-fabricated Swagelok-type cell for battery testing.

6.3 Results and Discussion

The following section discusses the morphology and physical attributes of the as-synthesized material. It also reports the results of electrochemical testing performed on pure CNT and the CNT-Cu_2O hybrid.

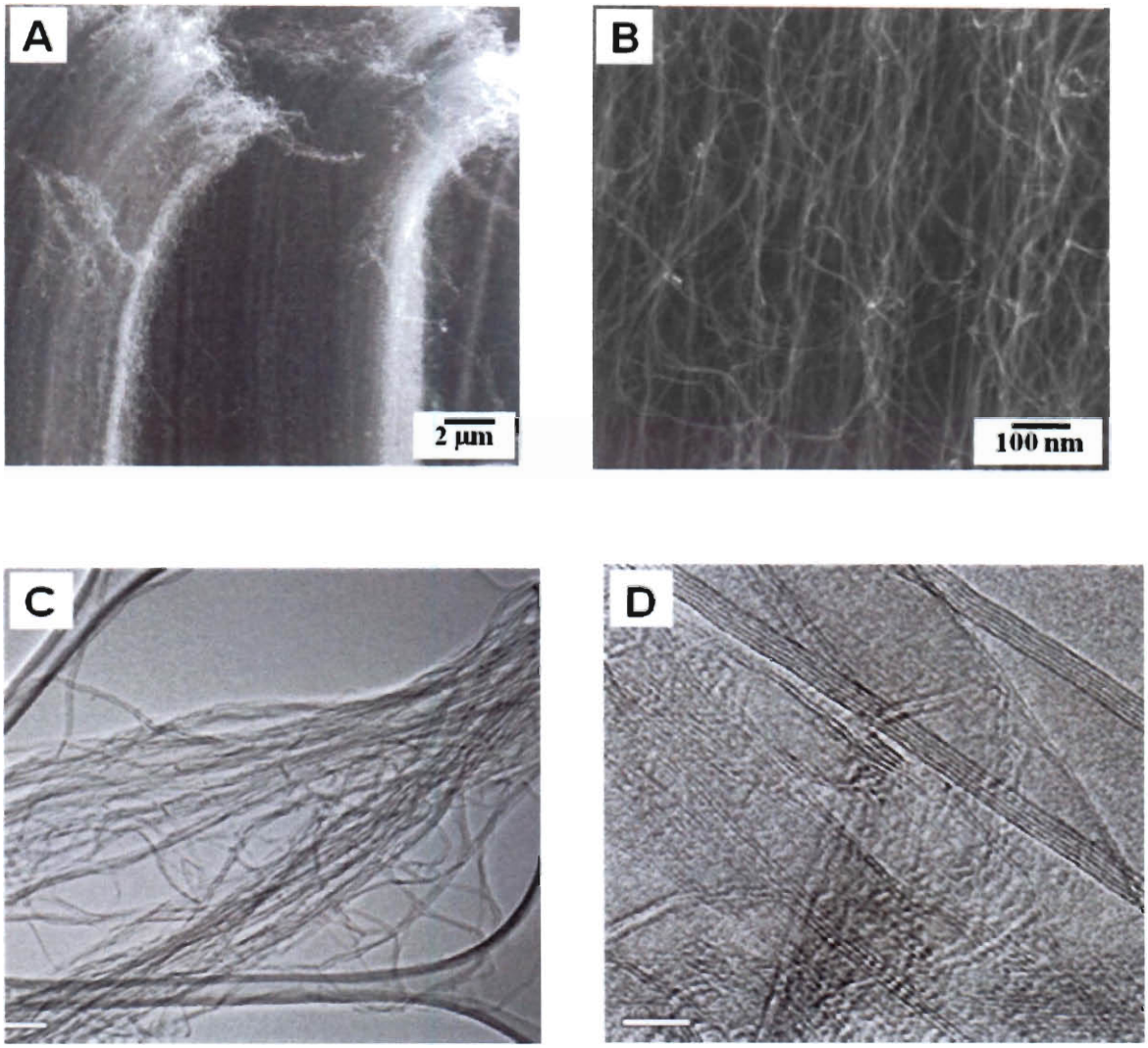

Figure 6.5 (A) and (B) SEM images of as-grown aligned CNTs. (C) and (D) HRTEM images confirming the multi-wall nature of the tubes.

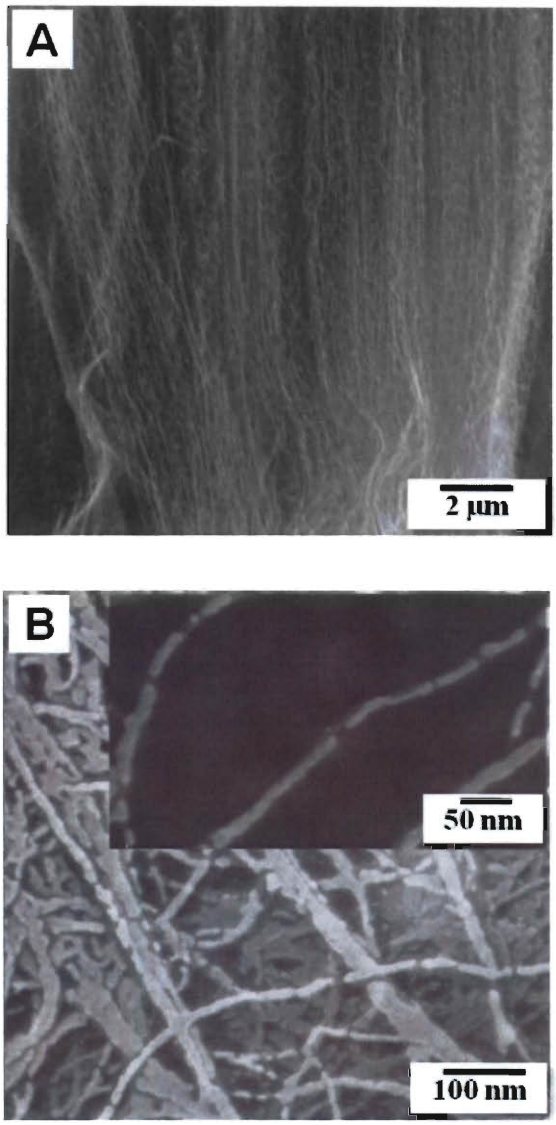

Figure 6.6 (A) and (B) SEM images of copper oxide coated CNTs. The inset shows a good conformal coverage of copper oxide on CNTs.

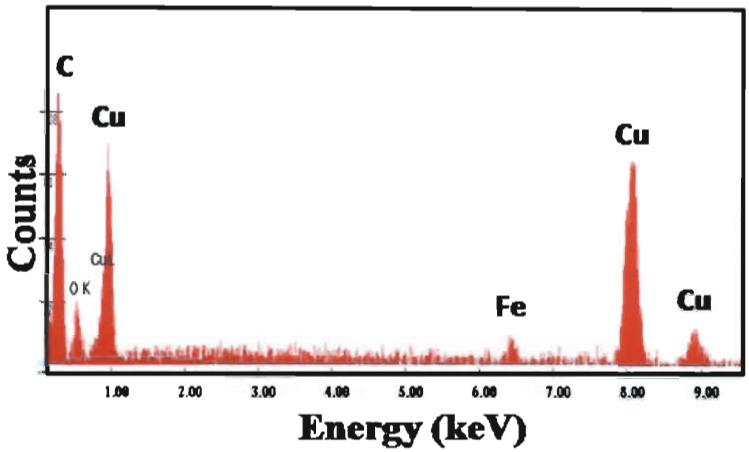

Figure 6.7 EDS spectrum obtained from coated CNTs after electrodeposition that confirms the presence of copper on CNTs. The weak iron signal is from the iron catalyst used for CNT growth.

Crystallinity of the coating was determined using XRD. The peaks in the XRD pattern (Figure 6.8) of copper oxide coated CNTs at 29.5°, 36.7°, 42.5°, 61.5° and 73.4° correspond to {110}, {111}, {200}, {220} and {311} Bragg reflections from the cubic cuprite phase (JCPDS # 005-0667), thereby confirming the formation of crystalline Cu_2O on the CNTs.[132] The other high-intensity peaks in the pattern at 44°, 50.9° and 74.7° originate from the steel substrate and match with the control pattern obtained from a pure steel substrate. Cu_2O is also the expected phase in accordance with the reaction mechanism explained by Joo and co-workers who proposed that electrodeposition proceeds through the formation of $Cu(OH)_2$ in the medium.[130] The hydroxide decomposes to form CuO followed by its subsequent conversion to Cu_2O.

$$Cu(OH)_2 \longrightarrow CuO + H_2O$$

$$2Cu^{2+} + 2OH^- + 2e^- \longrightarrow Cu_2O + H_2O$$

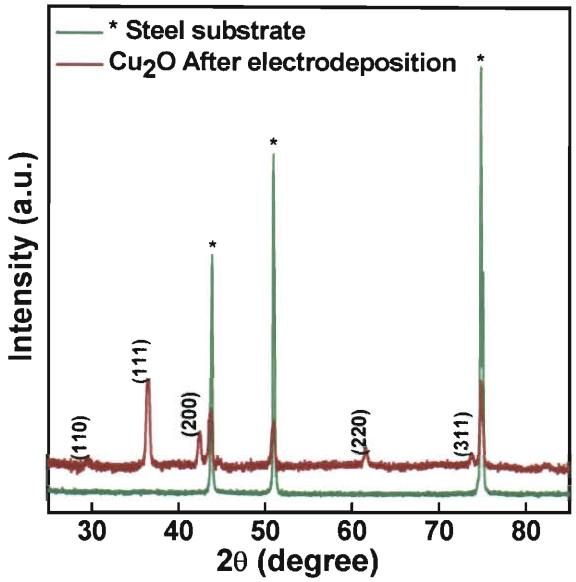

Figure 6.8 XRD pattern obtained from Cu_2O-CNT hybrids showing the crystalline nature of Cu_2O coating. Peaks at 2Θ values of 44°, 50.9° & 74.7° originate from the steel substrate used for CNT growth.

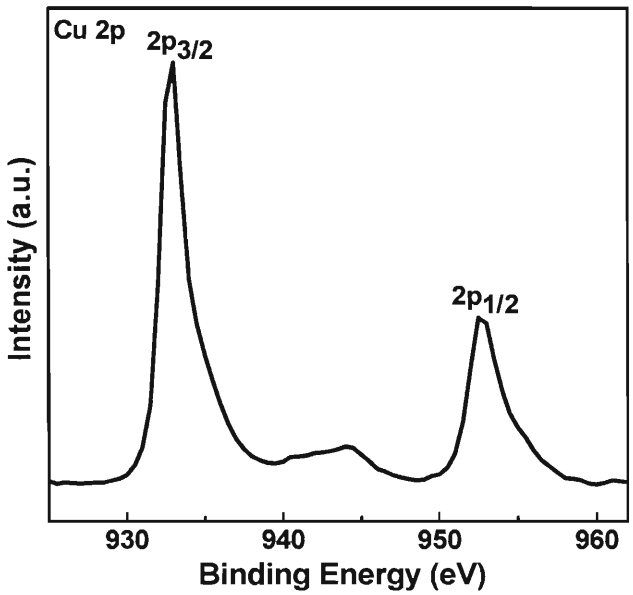

Figure 6.9 XPS spectrum of Cu_2O-CNT hybrid. The peak positions establish the presence of copper as Cu_2O.

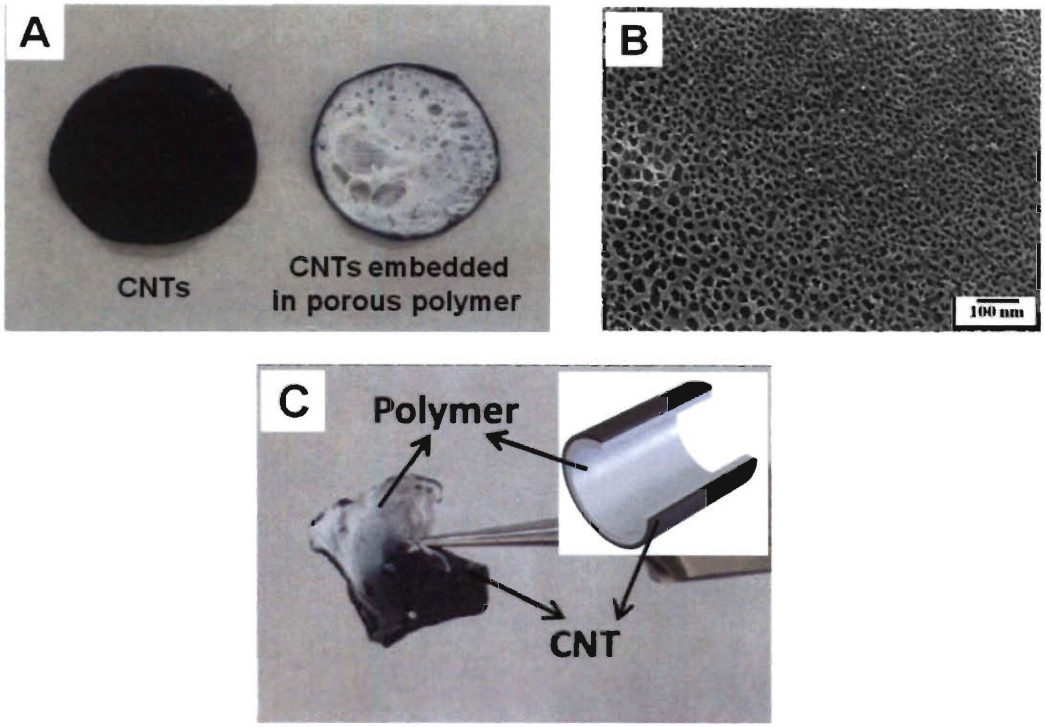

Figure 6.10 (A) Photographs of pure CNTs and CNTs after polymer infiltration. (B) SEM image revealing the porous nature of the PVDF-HFP-SiO_2 film after phase inversion (C) The photograph emphasizing the good flexibility of the peeled films.

6.3.2 Electrochemical Testing

These free-standing electrodes were tested against Li-metal for application in batteries as an anode material. Figures 6.11 (A) and (B) show the galvanostatic charge-discharge curves for the pure CNTs and the CNT-Cu_2O hybrid electrodes. The capacity for the first discharge is 2.3 $mAhcm^{-2}$ for the hybrid as compared to 1.2 $mAhcm^{-2}$ for pure CNTs. The decay in the capacity between the first and the second cycle is due to the formation of the solid electrolyte interphase (SEI) layer on the electrodes.[134] The capacity variation was recorded for a number of cycles; the comparison between the hybrid electrode and pure CNTs is shown in Figure 6.12. The capacity subsequently saturates, and even after 15 cycles the hybrid retains its good capacity and exhibits a better

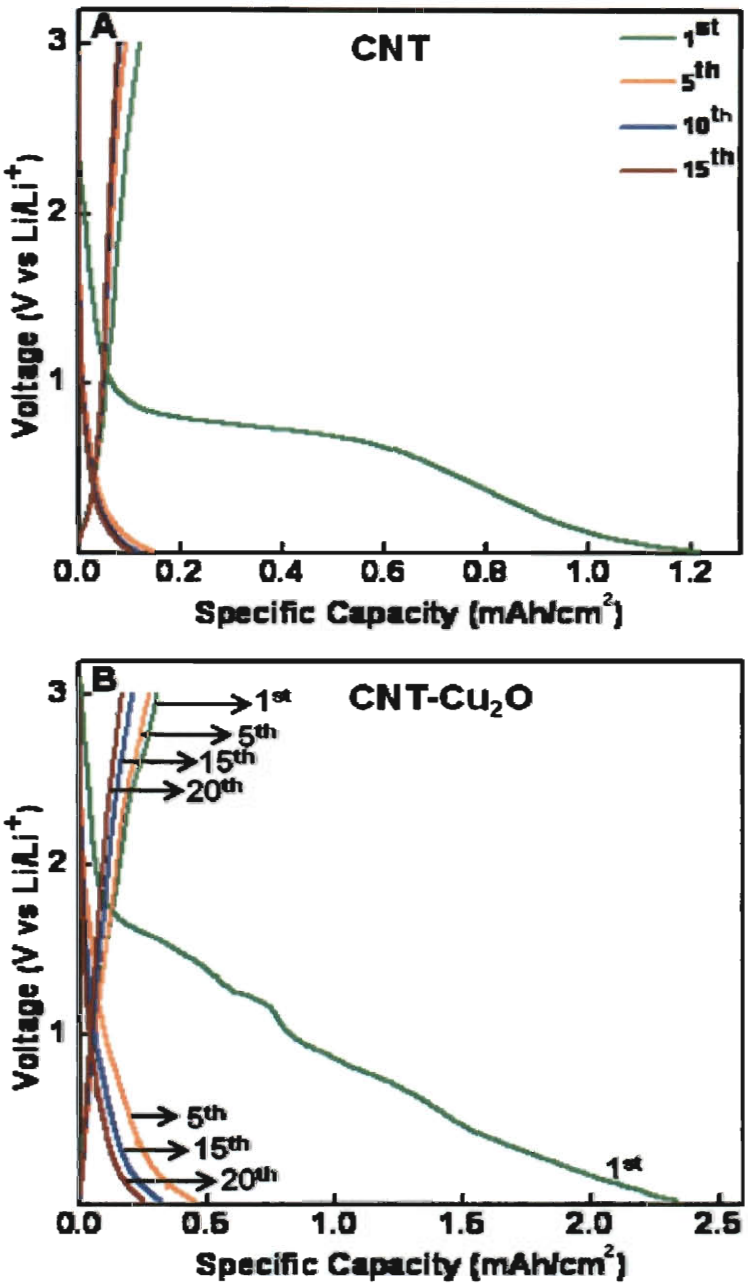

Figure 6.11 Charge-discharge voltage profiles of (A) pure CNTs and (B) CNT-Copper oxide hybrid between 0.02 and 3V vs Li/Li+

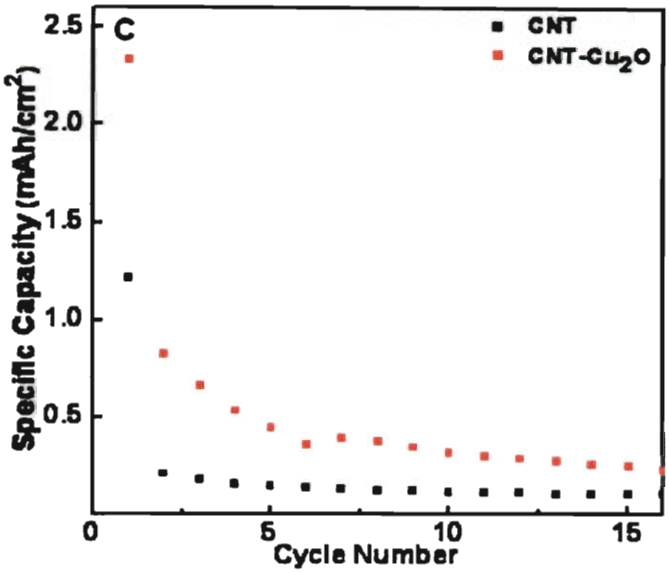

Figure 6.12 Comparison of the electrochemical performance of pure CNTs and CNT-Cu_2O hybrids. The hybrid shows a two times better capacity as compared to pure CNTs.

6.4 Conclusions

Cu_2O-CNT hybrid structures have been fabricated towards application as an anode material for lithium-ion batteries. The electrodeposition process used for coating Cu_2O on aligned CNTs results in a good conformal coverage of the oxide over CNTs. Embedding the hybrid material in a porous PVDF-HFP-SiO_2 membrane gives an additional advantage by resulting in a flexible, free-standing electrode. The CNT-Cu_2O composite anode exhibits a two times higher capacity as compared to pure CNTs. This innovative methodology provides a new design and a better performing material, thereby opening avenues for advanced applications that require flexible electrodes. This design is particularly useful for applications requiring lightweight and miniaturized batteries.

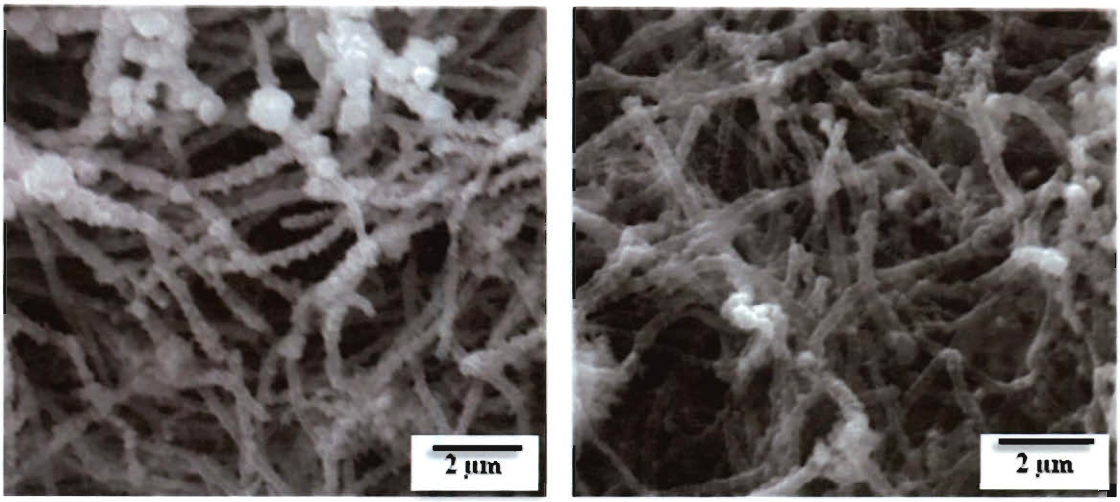

Figure 7.1 SEM images of SnS coated CNTs

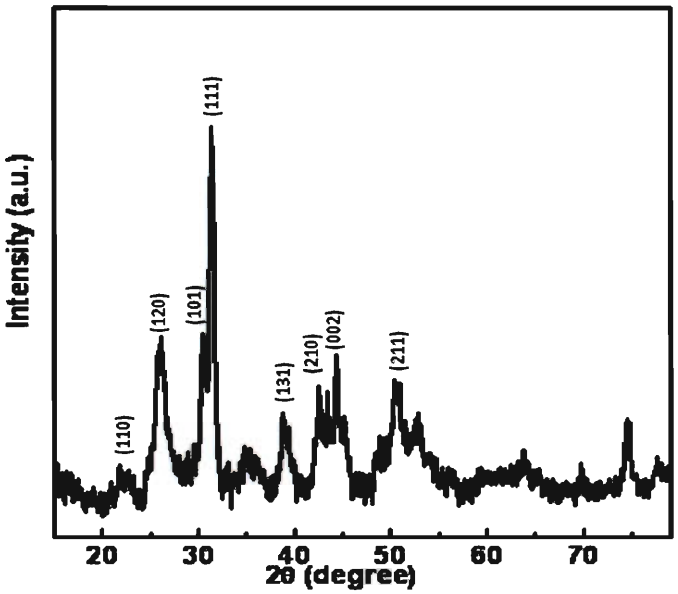

Figure 7.2 XRD spectrum confirming the formation of crystalline orthorhombic SnS

B-Beam Interactions with Materials and Atoms **1995,** 105, (1-4), 245-249.

36. Okamoto, T.; Nakamura, S., Thermal endurance, electrical insulating, and mechanical properties of hybrid made with poly(dimethylsiloxane) and tetraethoxysilane. *Japanese Journal of Applied Physics* **2008,** 47, (1), 521-526.

37. Yoshinaga, I.; Yamada, N.; Katayama, S., Effect of inorganic components on thermal stability of methylsiloxane-based inorganic/orgnaic hybrids. *Journal of Sol-Gel Science and Technology* **2005,** 35, (1), 21-26.

38. Wang, B.; Chen, K.; Jiang, S.; Reincke, F.; Tong, W. J.; Wang, D. Y.; Gao, C. Y., Chitosan-mediated synthesis of gold nanoparticles on patterned poly(dimethylsiloxane) surfaces. *Biomacromolecules* **2006,** 7, (4), 1203-1209.

39. Antolini, F.; Di Luccio, T.; Laera, A. M.; Mirenghi, L.; Piscopiello, E.; Re, M.; Tapfer, L., Direct synthesis of ii-vi compound nanocrystals in polymer matrix. *Physica Status Solidi B-Basic Solid State Physics* **2007,** 244, (8), 2768-2781.

40. Deshmukh, R. D.; Composto, R. J., Surface segregation and formation of silver nanoparticles created in situ in poly(methyl methacrylate) films. *Chemistry of Materials* **2007,** 19, (4), 745-754.

41. Yurkov, G. Y.; Baranov, D. A.; Kozinkin, A. V.; Nedoseikina, T. I.; Koksharov, Y. A.; Gubin, S. P., Copper nanoparticles on the surface of ultradispersed polytetrafluoroethylene nanograins. *Russian Journal of Inorganic Chemistry* **2006,** 51, (2),170-176.

42. Rutnakornpituk, M.; Thompson, M. S.; Harris, L. A.; Farmer, K. E.; Esker, A. R.; Riffle, J. S.; Connolly, J.; St Pierre, T. G., Formation of cobalt nanoparticle dispersions in the presence of polysiloxane block copolymers. *Polymer* **2002,** 43, (8), 2337-2348.

43. Abbasi, F.; Mirzadeh, H.; Katbab, A. A., Modification of polysiloxane polymers for biomedical applications: A review. *Polymer International* **2001,** 50, (12), 1279-1287.

44. Paul, D. R.; Mark, J. E., Fillers for polysiloxane ("Silicone") elastomers. *Progress in Polymer Science* 35, (7), 893-901.

45. Ciprari, D.; Jacob, K.; Tannenbaum, R., Characterization of polymer nanocomposite interphase and its impact on mechanical properties. *Macromolecules* **2006,** 39, (19), 6565-6573.

46. Fitzgerald, J. J.; Martellock, A. C.; Nielsen, P. L.; Schillace, R. V., The effect of cyclic stress on the physical-properties of a poly(dimethylsiloxane) elastomer. *Polymer Engineering and Science* **1992,** 32, (18), 1350-1357.

47. Kaully, T.; Siegmann, A.; Shacham, D., Mechanical behavior of highly filled natural caco3 composites: Effect of particle size distribution and interface interactions. *Polymer Composites* **2008,** 29, (4), 396-408.

48. Gee, R. H.; Maxwell, R. S.; Balazs, B., Molecular dynamics studies on the effects of water speciation on interfacial structure and dynamics in silica-filled pdms composites. *Polymer* **2004,** 45, (11), 3885-3891.

49. Huang, X.; Fang, X. L.; Lu, Z.; Chen, S., Reinforcement of polysiloxane with superhydrophobic nanosilica. *Journal of Materials Science* **2009,** 44, (17), 4522-4530.

50. LeBaron, P. C.; Pinnavaia, T. J., Clay nanolayer reinforcement of a silicone elastomer. *Chemistry of Materials* **2001,** 13, (10), 3760-3765.

51. Pu, Z. C.; Mark, J. E.; Beaucage, G., Some attempts to force poly(dimethylsiloxane) chains through zeolite cavities to improve elastomer reinforcement. *Rubber Chemistry and Technology* **1999,** 72, (1), 138-151.

52. Vankelecom, I. F. J.; Jacobs, P. A., Dense organic catalytic membranes for fine chemical synthesis. *Catalysis Today* **2000,** 56, (1-3), 147-157.

53. Brandao, L.; Fritsch, D.; Mendes, A. M.; Madeira, L. M., Propylene hydrogenation in a continuous polymeric catalytic membrane reactor. *Industrial & Engineering Chemistry Research* **2007,** 46, (16), 5278-5285.

54. Rogach, A.; Susha, A.; Caruso, F.; Sukhorukov, G.; Kornowski, A.; Kershaw, S.; Mohwald, H.; Eychmuller, A.; Weller, H., Nano- and microengineering: Three-dimensional colloidal photonic crystals prepared from submicrometer-sized polystyrene latex spheres pre-coated with luminescent polyelectrolyte/nanocrystal shells. *Advanced Materials* **2000,** 12, (5), 333-337

55. Chen, C. W.; Serizawa, T.; Akashi, M., Preparation of platinum colloids on polystyrene nanospheres and their catalytic properties in hydrogenation. *Chemistry of Materials* **1999,** 11, (5), 1381-1389.

56. Arshady, R., Microspheres for biomedical applications - preparation of reactive and labeled microspheres. *Biomaterials* **1993,** 14, (1), 5-15.

57. Sprycha, R.; Oyama, H. T.; Zelenev, A.; Matijevic, E., Characterization of polymer-coated silica particles by microelectrophoresis. *Colloid and Polymer Science* **1995,** 273, (7), 693-700.

58. Quaroni, L.; Chumanov, G., Preparation of polymer-coated functionalized silver nanoparticles. *Journal of the American Chemical Society* **1999,** 121, (45), 10642-10643.

59. Hall, S. R.; Davis, S. A.; Mann, S., Cocondensation of organosilica hybrid shells on nanoparticle templates: A direct synthetic route to functionalized core-shell colloids. *Langmuir* **2000,** 16, (3), 1454-1456.

60. Caruso, F.; Lichtenfeld, H.; Donath, E.; Mohwald, H., Investigation of electrostatic interactions in polyelectrolyte multilayer films: Binding of anionic fluorescent probes to layers assembled onto colloids. *Macromolecules* **1999,** 32, (7), 2317-2328.

61. Zhu, M. Q.; Wang, L. Q.; Exarhos, G. J.; Li, A. D. Q., Thermosensitive gold nanoparticles. *Journal of the American Chemical Society* **2004,** 126, (9), 2656-2657.

62. Artus, G. R. J.; Jung, S.; Zimmermann, J.; Gautschi, H. P.; Marquardt, K.; Seeger, S., Silicone nanofilaments and their application as superhydrophobic coating. *Advanced Materials* **2006,** 18, (20), 2758-2762.

63. Olson, L. G.; Lo, Y. S.; Beebe, T. P.; Harris, J. M., Characterization of silane-modified immobilized gold colloids as a substrate for surface-enhanced raman spectroscopy. *Analytical Chemistry* **2001,** 73, (17), 4268-4276.

64. Ke, Q. P.; Li, G. L.; Liu, Y.; He, T.; Li, X. M., Formation of superhydrophobic polymerized n-octadecylsiloxane nanosheets. *Langmuir* 26, (5), 3579-3584.

65. Prasad, B. L. V.; Stoeva, S. I.; Sorensen, C. M.; Zaikovski, V.; Klabunde, K. J., Gold nanoparticles as catalysts for polymerization of alkylsilanes to siloxane nanowires, filaments, and tubes. *Journal of the American Chemical Society* **2003,** 125, (35), 10488-10489.

66. Wei, Q. Y.; Li, B.; Li, C.; Wang, J. Q.; Wang, W.; Yang, X. J., Pvp-capped silver nanoparticles as catalysts for polymerization of alkylsilanes to siloxane composite microspheres. *Journal of Materials Chemistry* **2006,** 16, (36), 3606-3608.

67. Tarascon, J. M.; Armand, M., Issues and challenges facing rechargeable lithium batteries. *Nature* **2001,** 414, (6861), 359-367.

68. Megahed, S.; Scrosati, B., Lithium-ion rechargeable batteries. *Journal of Power Sources* **1994,** 51, (1-2), 79-104.

69. Schalkwijk, W. A. V.; Scrosati, B., Advances in lithium-ion batteries. *Kluwer Academic* **2002**.

70. Ikeda, H.; Saito, T.; Tamura, H., Proc. Manganese dioxide symp., vol 1 *IC Sample office, Cleaveland OH* **1975**.

71. Whittingham, M. S., Electrical energy-storage and intercalation chemistry. *Science* **1976,** 192, (4244), 1126-1127.

72. Rao, B. M. L.; Francis, R. W.; Christopher, H. A., Lithium-aluminum electrode. *Journal of the Electrochemical Society* **1977,** 124, (10), 1490-1492.

73. Mizushima, K.; Jones, P. C.; Wiseman, P. J.; Goodenough, J. B., Lixcoo2 "(oless-thanxless-than-or-equal-to1) - a new cathode material for batteries of high-energy density. *Materials Research Bulletin* **1980,** 15, (6), 783-789.

74. Thackeray, M. M.; David, W. I. F.; Bruce, P. G.; Goodenough, J. B., Lithium insertion into manganese spinels. *Materials Research Bulletin* **1983,** 18, (4), 461-472.

75. Nagaura, T.; Tozawa, K., Lithium ion rechargeable battery. *Prog. Batteries Solar Cells* **1990,** 9, 209.

76. Armand, M., Polymer solid electrolytes - an overview. *Solid State Ionics* **1983,** 9-10, (DEC), 745-754.

77. Tarascon, J. M.; Gozdz, A. S.; Schmutz, C.; Shokoohi, F.; Warren, P. C., Performance of bellcore's plastic rechargeable li-ion batteries. *Solid State Ionics* **1996,** 86-8, 49-54.

78. Stolarska, M.; Niedzicki, L.; Borkowska, R.; Zalewska, A.; Wieczorek, W.,

Structure, transport properties and interfacial stability of pvdf/hfp electrolytes containing modified inorganic filler. *Electrochimica Acta* **2007,** 53, (4), 1512-1517.

79. Kim, K. M.; Park, N. G.; Ryu, K. S.; Chang, S. H., Characterization of poly(vinylidenefluoride-co-hexafluoropropylene)-based polymer electrolyte filled with tio2 nanoparticles. *Polymer* **2002,** 43, (14), 3951-3957.

80. Li, Z. H.; Su, G. Y.; Wang, X. Y.; Gao, D. S., Micro-porous p(vdf-hfp)-based polymer electrolyte filled with al2o3 nanoparticles. *Solid State Ionics* **2005,** 176, (23-24), 1903-1908.

81. Landi, B. J.; Ganter, M. J.; Cress, C. D.; DiLeo, R. A.; Raffaelle, R. P., Carbon nanotubes for lithium ion batteries. *Energy & Environmental Science* **2009,** 2, (6), 638-654.

82. Su, D. S.; Schlogl, R., Nanostructured carbon and carbon nanocomposites for electrochemical energy storage applications. *Chemsuschem* 3, (2), 136-168.

83. Iijima, S., Helical microtubules of graphitic carbon. *Nature* **1991,** 354, (6348), 56-58.

84. Qin, L. C.; Iijima, S., Structure and formation of raft-like bundles of single-walled helical carbon nanotubes produced by laser evaporation. *Chemical Physics Letters* **1997,** 269, (1-2), 65-71.

85. Ebbesen, T. W.; Ajayan, P. M., Large-scale synthesis of carbon nanotubes. *Nature* **1992,** 358, (6383), 220-222.

86. Ci, L. J.; Manikoth, S. M.; Li, X. S.; Vajtai, R.; Ajayan, P. M., Ultrathick freestanding aligned carbon nanotube films. *Advanced Materials* **2007,** 19, 3300-3303.

87. Kumar, M.; Ando, Y., Chemical vapor deposition of carbon nanotubes: A review

on growth mechanism and mass production. *Journal of Nanoscience and Nanotechnology* 10, (6), 3739-3758.

88. Talapatra, S.; Kar, S.; Pal, S. K.; Vajtai, R.; Ci, L.; Victor, P.; Shaijumon, M. M.; Kaur, S.; Nalamasu, O.; Ajayan, P. M., Direct growth of aligned carbon nanotubes on bulk metals. *Nature Nanotechnology* **2006,** 1, (2), 112-116.

89. Masarapu, C.; Wei, B. Q., Direct growth of aligned multiwalled carbon nanotubes on treated stainless steel substrates. *Langmuir* **2007,** 23, (17), 9046-9049.

90. Jung, M.; Eun, K. Y.; Lee, J. K.; Baik, Y. J.; Lee, K. R.; Park, J. W., Growth of carbon nanotubes by chemical vapor deposition. *Diamond and Related Materials* **2001,** 10, (3-7), 1235-1240.

91. Ervin, M. H.; Nichols, B. M., Electron beam induced deposition of cobalt for use as single- and multiwalled carbon nanotube growth catalyst. *Journal of Vacuum Science & Technology B* **2009,** 27, (6), 2982-2985.

92. Hiraoka, T.; Yamada, T.; Hata, K.; Futaba, D. N.; Kurachi, H.; Uemura, S.; Yumura, M.; Iijima, S., Synthesis of single- and double-walled carbon nanotube forests on conducting metal foils. *Journal of the American Chemical Society* **2006,** 128, (41), 13338-13339.

93. Kim, B.; Chung, H.; Chu, K. S.; Yoon, H. G.; Lee, C. J.; Kim, W., Synthesis of vertically-aligned carbon nanotubes on stainless steel by water-assisted chemical vapor deposition and characterization of their electrochemical properties. *Synthetic Metals* 160, (7-8), 584-587.

94. Ajayan, P. M.; Ebbesen, T. W., Nanometre-size tubes of carbon. *Reports on Progress in Physics* **1997,** 60, (10), 1025-1062.

95. Treacy, M. M. J.; Ebbesen, T. W.; Gibson, J. M., Exceptionally high young's modulus observed for individual carbon nanotubes. *Nature* **1996,** 381, (6584), 678-680.

96. Kim, P.; Shi, L.; Majumdar, A.; McEuen, P. L., Thermal transport measurements of individual multiwalled nanotubes. *Physical Review Letters* **2001,** 87, (21).

97. Pushparaj, V. L.; Shaijumon, M. M.; Kumar, A.; Murugesan, S.; Ci, L.; Vajtai, R.; Linhardt, R. J.; Nalamasu, O.; Ajayan, P. M., Flexible energy storage devices based on nanocomposite paper. *Proceedings of the National Academy of Sciences of the United States of America* **2007,** 104, 13574-13577.

98. Li, W. Z.; Wang, X.; Chen, Z. W.; Waje, M.; Yan, Y. S., Carbon nanotube film by filtration as cathode catalyst support for proton-exchange membrane fuel cell. *Langmuir* **2005,** 21, (21), 9386-9389.

99. Centi, G.; Perathoner, S., Problems and perspectives in nanostructured carbon-based electrodes for clean and sustainable energy. *Catalysis Today* 150, (1-2), 151-162.

100. Emmenegger, C.; Mauron, P.; Sudan, P.; Wenger, P.; Hermann, V.; Gallay, R.; Zuttel, A., Investigation of electrochemical double-layer (ecdl) capacitors electrodes based on carbon nanotubes and activated carbon materials. *Journal of Power Sources* **2003,** 124, (1), 321-329.

101. Honda, K.; Yoshimura, M.; Kawakita, K.; Fujishima, A.; Sakamoto, Y.; Yasui, K.; Nishio, N.; Masuda, H., Electrochemical characterization of carbon nanotube/nanohoneycomb diamond composite electrodes for a hybrid anode of li-ion battery and super capacitor. *Journal of the Electrochemical Society* **2004,** 151, (4), A532-A541.

102. Zhang, H.; Cao, G. P.; Yang, Y. S.; Gu, Z. N., Comparison between electrochemical properties of aligned carbon nanotube array and entangled carbon nanotube electrodes. *Journal of the Electrochemical Society* **2008,** 155, (2), K19-K22.

103. Mahendra, S.; Zhu, H.; Colvin, V. L.; Alvarez, P. J. J., Quantum dot weathering results in microbial toxicity. *Environmental Science and Technology* **2008,** 42, 9424.

104. Yamaguchi, T.; Baertsch, C.; Koval, C. A.; Noble, R. D.; Bowman, C. N., Olefin separation using silver impregnated ion-exchange membranes and silver salt/polymer blend membranes. *Journal of Membrane Science* **1996,** 117, (1-2), 151-161.

105. Kuila, B. K.; Garai, A.; Nandi, A. K., Synthesis, optical, and electrical characterization of organically soluble silver nanoparticles and their poly(3-hexylthiophene) nanocomposites: Enhanced luminescence property in the nanocomposite thin films. *Chemistry of Materials* **2007,** 19, (22), 5443-5452.

106. Kumar, A.; Joshi, H.; Pasricha, R.; Mandale, A. B.; Sastry, M., Phase transfer of silver nanoparticles from aqueous to organic solutions using fatty amine molecules. *Journal of Colloid and Interface Science* **2003,** 264, (2), 396-401.

107. Dane, A.; Demirok, U. K.; Aydinli, A.; Suzer, S., X-ray photoelectron spectroscopic analysis of si nanoclusters in sio2 matrix. *Journal of Physical Chemistry B* **2006,**110,(3),1137-1140.

108. Maddams, W. F., A review of fourier-transform raman-spectroscopic studies on polymers. *Spectrochimica Acta Part a-Molecular and Biomolecular Spectroscopy* **1994,** 50, (11), 1967-1986.

109. Fukushima, M.; Noguchi, N.; Aramata, M.; Hamada, Y.; Tabei, E.; Mori, S.; Yamamoto, Y., Polysilanes as conducting material producers and their application to

metal pattern formation by uv light and electroless metallization. *Synthetic Metals* **1998,** 97, (3), 273-280.

110. Lewis, L. N., Chemical catalysis by colloids and clusters. *Chemical Reviews* **1993,** 93, (8), 2693-2730.

111. Stafie, N.; Stamatialis, D. F.; Wessling, M., Effect of pdms cross-linking degree on the permeation performance of pan/pdms composite nanofiltration membranes. *Separation and Purification Technology* **2005,** 45, (3), 220-231.

112. Choi, O.; Deng, K. K.; Kim, N. J.; Ross, L.; Surampalli, R. Y.; Hu, Z. Q., The inhibitory effects of silver nanoparticles, silver ions, and silver chloride colloids on microbial growth. *Water Research* **2008,** 42, (12), 3066-3074.

113. Gogoi, S. K.; Gopinath, P.; Paul, A.; Ramesh, A.; Ghosh, S. S.; Chattopadhyay, A., Green fluorescent protein-expressing escherichia coli as a model system for investigating the antimicrobial activities of silver nanoparticles. *Langmuir* **2006,** 22, (22), 9322-9328.

114. Creighton, J. A.; Eadon, D. G., Ultraviolet visible absorption-spectra of the colloidal metallic elements. *Journal of the Chemical Society-Faraday Transactions* **1991,** 87, (24), 3881-3891.

115. Schofield, C. L.; Haines, A. H.; Field, R. A.; Russell, D. A., Silver and gold glyconanoparticles for colorimetric bioassays. *Langmuir* **2006,** 22, (15), 6707-6711.

116. Colas, A., Silicones: Preparation, properties and performance. www.dowcorning.com **2005**.

117. Fukushima, M.; Hamada, Y.; Tabei, E.; Aramata, M.; Mori, S.; Yamamoto, Y., Conductive circuit formation on organosilicon films by patterning with uv. *Chemistry*

Letters **1998**, (4), 347-348.

118. Esumi, K.; Tano, T.; Meguro, K., Preparation of organopalladium particles from thermal-decomposition of its organic-complex in organic-solvents. *Langmuir* **1989,** 5, (1), 268-270.

119. Owens, M. J., Why silicones behave funny. www.dowcorning.com **2005**.

120. Owens, T. M.; Ludwig, B. J.; Schneider, K. S.; Fosnacht, D. R.; Orr, B. G.; Holl, M. M. B., Oxidation of alkylsilane-based monolayers on gold. *Langmuir* **2004,** 20, (22), 9636-9645.

121. Jana, R. N.; Mukunda, P. G.; Nando, G. B., Thermogravimetric analysis of compatibilized blends of low density polyethylene and poly(dimethyl siloxane) rubber. *Polymer Degradation and Stability* **2003,** 80, (1), 75-82.

122. Stober, W.; Fink, A.; Bohn, E., Controlled growth of monodisperse silica spheres in micron size range. *Journal of Colloid and Interface Science* **1968,** 26, (1), 62-69.

123. Piccolo, L.; Becker, C.; Henry, C. R., Reaction between co and a pre-adsorbed oxygen layer on supported palladium clusters. *Applied Surface Science* **2000,** 164, 156-162.

124. Nam, K. T.; Kim, D. W.; Yoo, P. J.; Chiang, C. Y.; Meethong, N.; Hammond, P. T.; Chiang, Y. M.; Belcher, A. M., Virus-enabled synthesis and assembly of nanowires for lithium ion battery electrodes. *Science* **2006,** 312, (5775), 885-888.

125. Scrosati, B., Battery technology - challenge of portable power. *Nature* **1995,** 373, (6515), 557-558.

126. Armand, M.; Tarascon, J. M., Building better batteries. *Nature* **2008,** 451, (7179), 652-657.

127. Song, J. Y.; Wang, Y. Y.; Wan, C. C., Conductivity study of porous plasticized polymer electrolytes based on poly(vinylidene fluoride) - a comparison with polypropylene separators. *Journal of the Electrochemical Society* **2000,** 147, (9), 3219-3225.

128. He, X. M.; Shi, Q.; Zhou, X.; Wan, C. R.; Jiang, C. Y., In situ composite of nano sio2-p(vdf-hfp) porous polymer electrolytes for li-ion batteries. *Electrochimica Acta* **2005,** 51, (6), 1069-1075.

129. Subramania, A.; Sundaram, N. T. K.; Priya, A. R. S.; Kumar, G. V., Preparation of a novel composite micro-porous polymer electrolyte membrane for high performance li-ion battery. *Journal of Membrane Science* **2007,** 294, (1-2), 8-15.

130. Patake, V. D.; Joshi, S. S.; Lokhande, C. D.; Joo, O. S., Electrodeposited porous and amorphous copper oxide film for application in supercapacitor. *Materials Chemistry and Physics* **2009,** 114, (1), 6-9.

131. Kim, K. M.; Park, N. G.; Ryu, K. S.; Chang, S. H., Characteristics of pvdf-hfp/tio2 composite membrane electrolytes prepared by phase inversion and conventional casting methods. *Electrochimica Acta* **2006,** 51, (26), 5636-5644.

132. Fu, L.; Gao, J.; Zhang, T.; Cao, Q.; Yang, L. C.; Wu, Y. P.; Holze, R., Effect of cu2o coating on graphite as lithium ion battery in pc-based anode material of electrolyte. *Journal of Power Sources* **2007,** 171, (2), 904-907.

133. Freeman, B.; Pinnau, I., Separation of gases using solubility-selective polymers. *Trends in Polymer Science* **1997,** 5, (5), 167-173.

134. Edstrom, K.; Gustafsson, T.; Thomas, J. O., The cathode-electrolyte interface in the li-ion battery. *Electrochimica Acta* **2004,** 50, (2-3), 397-403.

135. Grugeon, S.; Laruelle, S.; Herrera-Urbina, R.; Dupont, L.; Poizot, P.; Tarascon, J. M., Particle size effects on the electrochemical performance of copper oxides toward lithium. *Journal of the Electrochemical Society* **2001,** 148, (4), A285-A292.

Appendix A

Gecko-inspired, CNT-based synthetic adhesives

1. Introduction

The diverse, well-evolved mechanisms behind locomotion in nature have always been intriguing to the human mind. In the last decade, as the understanding of the field developed, there has been a spur in activities to extrapolate these mechanisms to artificial systems. One such system is carbon nanotubes (CNTs) that have been used in the present study to fabricate synthetic adhesive tapes based on the hierarchical hair structure found in geckos. In this study, adhesion experiments were carried out on patterned CNTs and the high shear forces obtained were attributed to the extensive contact obtained through CNT side-walls.

Geckos have been a focus of interest due to their extraordinary ability to climb vertical surfaces at speeds of over 1m/sec.[1-6] The dry adhesion present in geckos' feet overcomes many of the limitations of conventional pressure-sensitive adhesives (PSAs). PSAs are generally based on soft-viscolelastic polymers (Young's modulus < 100kPa) that are extremely prone to degradation due to self entanglement or contamination. In contrast, the hair on a gecko toe have been shown to self-clean and be functional for long durations without grooming, a property rarely seen in adhesives.[7] The adhesion forces in PSAs can drop with time but those geckos are known to sustain long and constant adhesion to a surface. While a gecko has a strong attachment ~ 0.09 N/mm^2, it also has a built-in release mechanism that helps in rapidly detaching the toe in about 15 milliseconds.[1, 8] The extraordinary adhesion force arises from the fibrillar structure

present in a gecko's toe. In animals, the density of hair increases with body weight and geckos are known to have the highest hair density (Figure A.1).[9]

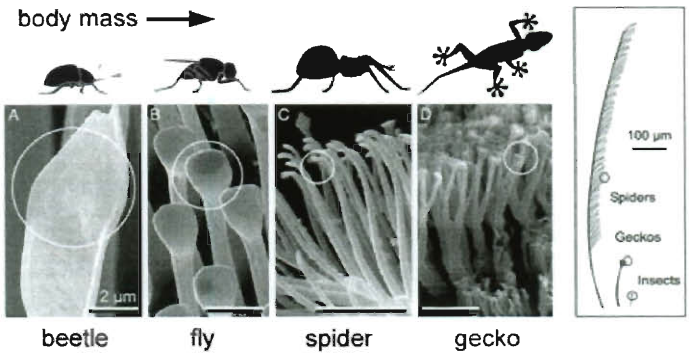

Figure A.1 The fibrillar structures found in various species. The density of hair increases with body weight and heavier animals have finer hair. (Arzt et al. *PNAS* 2003, 100, (19))

2. Morphology and Mechanism

The key to gecko's motion is the hierarchical structure of its hairy pads. These consist of 100µm long × 5µm thick fibrils called setae which further branch out to 200nm long and 15nm thick structures called spatulas as seen from Figure A.2.[7, 10, 11] The fibrils are uniformly oriented and distributed in a lamellar pattern on the toe with a density of about 14,400 per mm^2. The high aspect ratio and nanoscale geometry of spatulas provide a large-area intimate contact with the surface. The cumulative effects of these multiple contacts generate large frictional forces through intermolecular van der Waals adhesion. It was initially postulated that gecko adhesion could be based on suction, glue or capillary forces but Autumn et al.'s seminal work established conclusively that van der Waal's attraction was the key operating force.[12] Therefore, the compliant fibrillar structure becomes important in adhesion as van der Waals forces depend mainly on the distance between the two surfaces. Additionally, Autumn et al. have shown adhesion to be

independent of surface hydrophobicity. While they had attributed adhesion solely to van der Waals forces, some recent studies have noticed the adhesion to increase under the effects of humidity and temperature, though the exact dependence was found to be too complex to define. [13, 14]

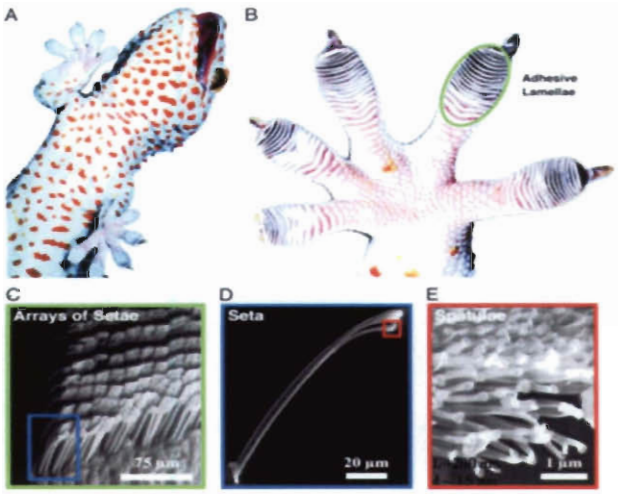

Figure A.2 Hierarchical structure of a gecko foot hair. The lamella is composed of well-oriented and densely packed micron-long setae which branch out at the tip into finer nanoscale spatulas. (Hansen et al. *PNAS* 2005, 102, (2))

The adhesion mechanism of geckos is mechanically controlled and involves a particular orientation of the hair and a small preload perpendicular to the surface followed by a drag along the direction of surface, all of which ensure maximum engagement of hair with the surface (Figure A.3).[15] The setae have a slight curvature at the tips and are oriented at an angle of 45° which helps in providing good contact.[16] For easy detachment, the gecko uncurls its toe above a critical angle (> 30°) which rapidly reduces the friction and facilitates an easy peeling of the spatula perpendicular to the surface.

It is the patterning present in the fibrillar structures and the splitting of the thick setae to finer spatulas that is the source of large adhesive forces observed in geckos. This

phenomenon known as "Contact Splitting" based on the theory of contact mechanics by Johnson, Kendell and Roberts (JKR) explains how a patterned surface results in better adhesion when compared to a continuous surface.[9, 17, 18] If the interfacial adhesion is Gc and the width of the interface is Ws, then the applied force Ps[19] is given by: Ps = Ws.Gc

From the illustration shown in Figure A.4, it can be seen how this force scales with patterning as the interfacial width (perimeter) increases on splitting the area in "n" small regions. "Contact Splitting" has been the major principle behind the design of effective artificial adhesives.

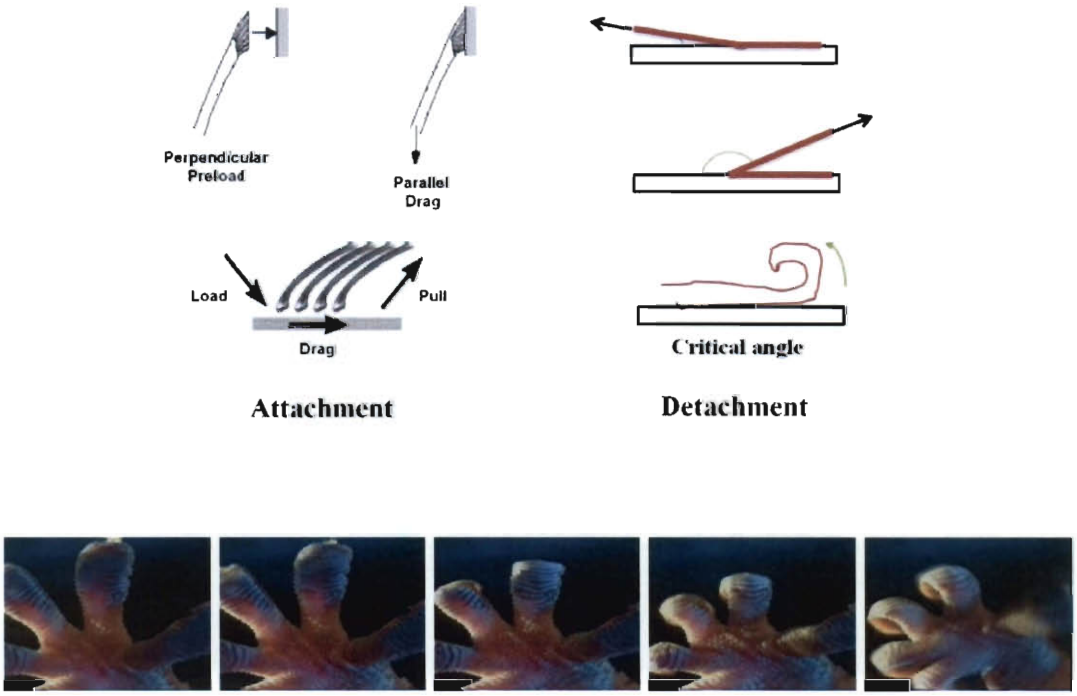

Figure A.3 Schematic and photographs of various phases of a gecko's attachment and detachment motion. Attachment requires a small preload and a shear movement while detachment proceeds by uncurling of the toe. (Autumn et al. *Nature* 2000, 405, (6787), Chan at al. *Mrs Bulletin* 2007, 32, (6), http://robotics.eecs.berkeley.edu/~ronf/Gecko)

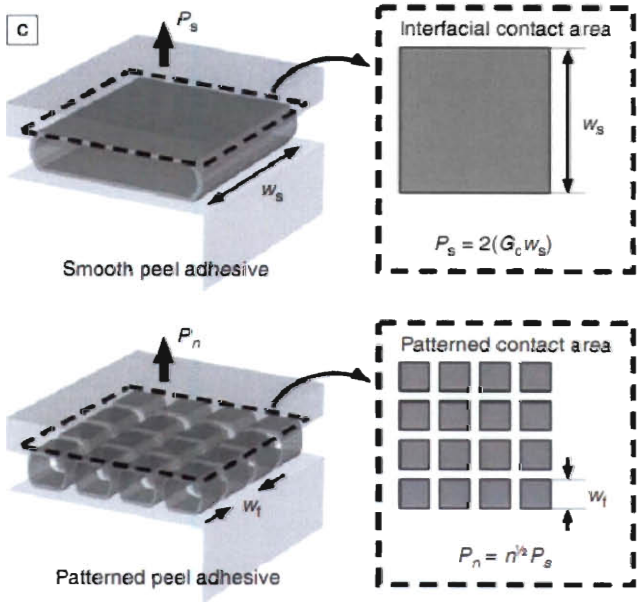

Figure A.4 An illustrative example of contact splitting. Dividing the pattern in smaller squares scales up the adhesive forces. (Chan et al. *Mrs Bulletin* 2007, 32, (6))

3. Synthetic Adhesives

Developing a synthetic adhesives based on the mechanism find in geckos calls for a judicious selection of both the materials and design parameters.[20,21] The orientation, aspect ratio and density of fibrils are important criteria for effective adhesion. The fibers are required to be adequately stiff to avoid mechanical collapse under their own weight. Further, it should be resistant to clustering while having flexibility for good contact. In obtaining ideal contact area, the shape of the fiber tips also plays an important role.

Polymers being flexible and easily moldable in different shapes were the first materials to be used for synthetic adhesives.[4, 5, 22-24] Sitti et al. fabricated silicone and polyimide hair using nano-indentation and template approaches[4] while Giem et al. formed polyimide hairs using electron-beam lithography and dry etching.[3] These hair were able to sustain forces of 70 nN per hair. Carbon nanotubes (CNTs) is another class

of material which has been explored due to the unparalleled advantages it offers as compared to polymers.[25-29] CNTs are highly flexible while at the same time are mechanically very strong.[30] They can be grown into controlled geometries with specified dimensions and aspect ratios and most importantly can be grown in a patterned manner to replicate natural designs based on "contact splitting".

Using patterned CNTs of various heights and widths (Figure A.5), Dhinojwala and co-workers have shown the formation of a CNT tape which can sustain four times higher shear stresses ($36N/m^2$) as compared to a gecko ($10N/m^2$).[25] They have also shown the CNT tape to maintain adhesion on surfaces with a range of hydrophobicity (Figure A.6). Additionally, unlike a conventional viscolelastic tape, the CNT tape is able to maintain the forces for long durations. In an extension of this study, these CNT pillars were shown to possess self-cleaning properties as those observed in nature.[26] CNTs inherently are super-hydrophobic and their self-cleaning property was probed using micron-size silica particles. CNTs retained 60 and 90% of their adhesion after cleaning the tape using water and vibrations respectively. The following section discusses the synthesis of patterned CNTs for forming the synthetic tape and further elaborates on studies undertaken to understand the mechanism behind the good adhesion obtained through CNTs.

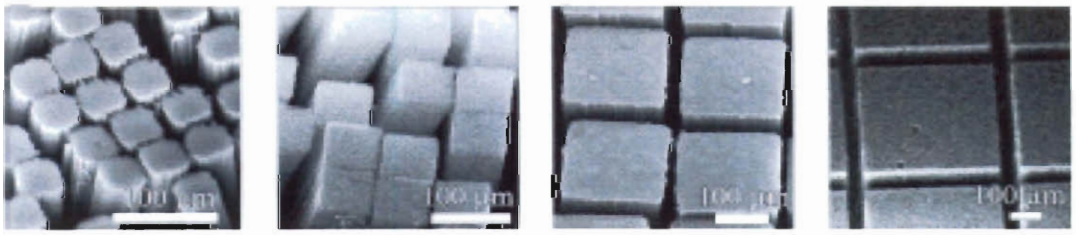

Figure A.5 SEM images of CNTs in different micron-sized patterns
(Ge et al. PNAS 2007, 104, (26))

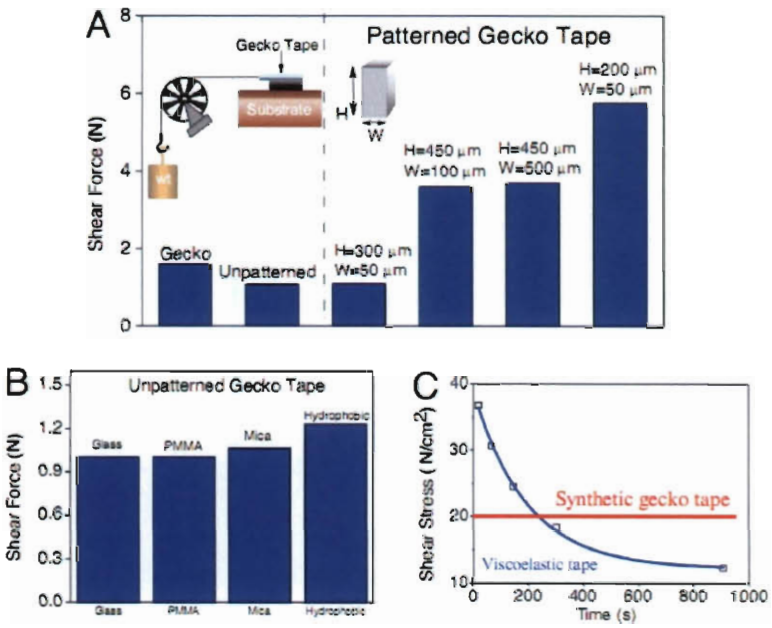

Figure A.6 (A) Shear force measurements using patterned and un-patterned CNTs. (B) Force measurements on different hydrophobicity surfaces. (C) The variation of adhesion force with time for CNT-based tape and a viscolelastic tape. (Ge et al. PNAS 2007, 104, (26))

4. Experimental

Multi-walled CNTs were grown by using a combination of photolithography and chemical vapor deposition technique (CVD).[31] A silicon wafer with a 500nm thick oxide layer was patterned using photolithography. Subsequently, the wafer was sequentially coated with 10 nm aluminum and 1.5 nm iron using an e-beam evaporator. The wafer was used as a substrate for CNT growth in a quartz tube at 775°C using ethylene (100sccm) as a carbon source (Figure A.7). An inert atmosphere was maintained in the furnace using a mixture of Ar/15%H_2 gases that were flowed at 1.3 slm. Figure A.8 shows the SEM image of patterned CNTs. The growth times were varied to obtain CNTs of different lengths.

In a collaborative work, the adhesion measurements were performed on these CNT patches at University of Akron. For adhesion measurements, the CNT pillars (500μm x 500μm, 280μm long) were transferred to a glass slide by pressing them lightly against a plasma-cleaned slide coated with uncured PDMS (Sylgard 184). After curing at 100°C for 1 hour, the CNTs were embedded in the polymer and the glass slide was peeled off the wafer. A custom-built friction cell was used to carry out the adhesion and friction tests.

Figure A.7 Photograph of the CVD system used for CNT growth

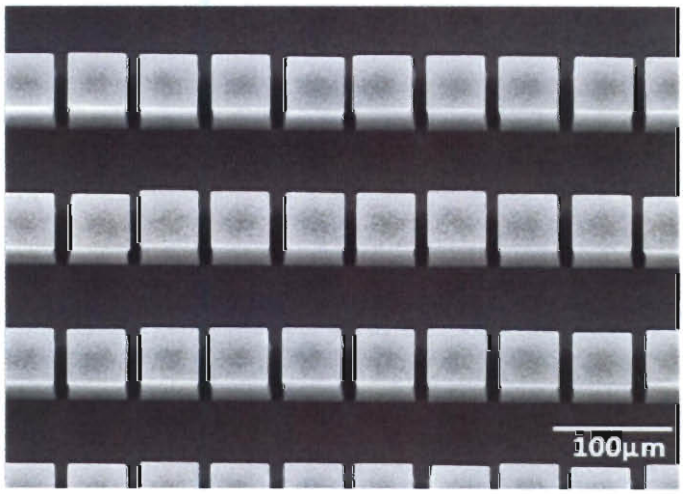

Figure A.8 A representative SEM image of the patterned CNTs

5. Results and Discussion

The CNT pillars transferred onto the glass slide were pressed against a silicon wafer at a rate of 1μm/sec and examined under SEM. Figure A.9(A) shows the SEM images at the various stages of compression. The nanotubes start bending under compression and if the pressure is high, the tubes do not revert to their original length after the force has been removed. A permanent deformation is created mainly in the form of buckling as seen in Figure A.9(B).

The buckling of CNTs also causes a significant enhancement in adhesion. A typical loading and un-loading curve is shown in Figure A.10(A). During un-loading a pull-off force is recorded and this forces varies with the applied pre-load as seen in Figure A.10(B). An increase in preload causes an increase in the pull-off force/area. This originated from the increase in the CNT contact area on increasing the pre-load as evident from the SEM images shown previously in Figure A.9. Under compression, the CNT side-walls come into contact with the surface and cause an increase in the pull-off force.

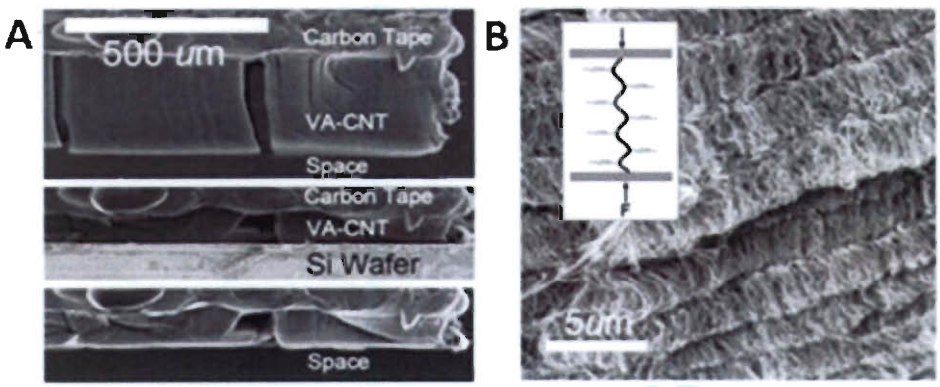

Figure A.9 (A) SEM images of CNT at various stages of compression, top panel: before compression, middle panel: during compression, bottom panel: after compression.
(B) SEM image showing the buckling created in nanotubes. (Ge et al. *Nanoletters* 2010)

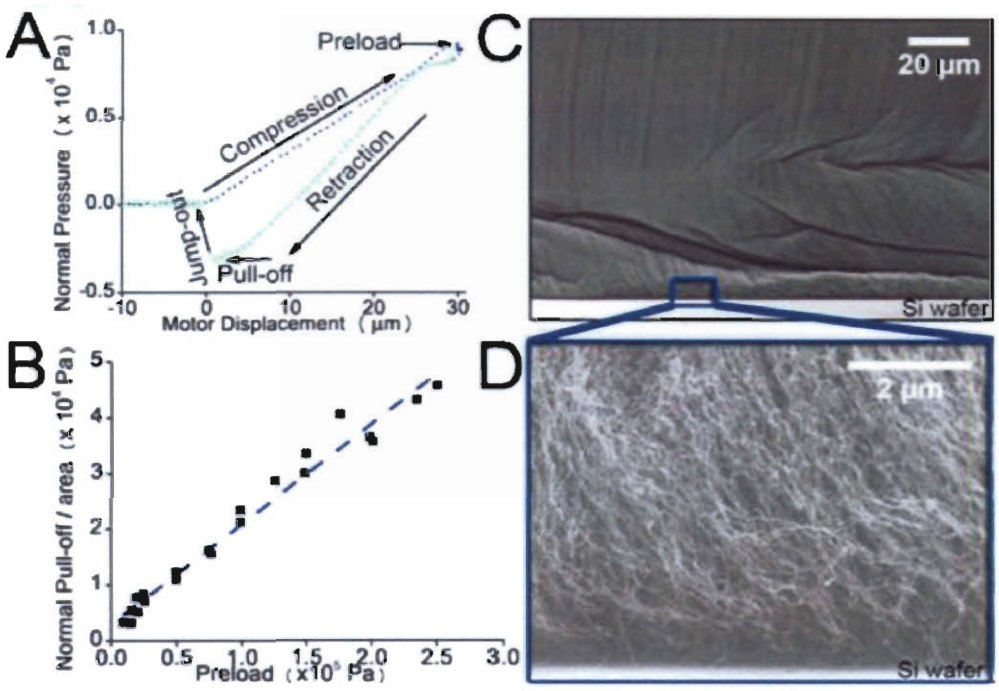

Figure A.10 (A) A typical loading and unloading cycle showing the pull-off force on retracting. (B) The normal stress increases with increasing pre-load. (C) SEM image showing the buckling under compression. (D) A zoomed-in image of the area shows the CNT side-walls in contact with the silicon surface. (Ge et al. *Nanoletters* 2010)

6. Conclusions and Future Work

The well-developed hierarchical designs found in nature can be adapted to synthetic adhesive systems such as patterned CNTs which show better adhesion than that observed in geckos in nature. This high adhesion originates from the extensive side walls contacts obtained on compressing CNTs under a preload. Development of CNT-based tapes paves the way for smart adhesives. For example, these systems can be designed to utilize unique properties of CNTs such as their high electrical and thermal conductivity in conjunction with their good flexibility and mechanical strength.

In literature, studies undertaken so far with patterned CNTs involve smooth surfaces. It would be interesting to determine the variation in forces with surface roughness as the practical applications of CNT tape will involve rough and irregular surfaces. Some of the preliminary work has been carried out towards this study where evenly spaced SU-8 pillars have been used to create rough surfaces. The roughness was varied by controlling the spacing and distance between the pillars.

The pillars were fabricated using the soft-lithography technique.[32] Following standard procedures, the pattern was created using a SU-8 50 photoresist film (Microchem Corporation). SU-8 was chosen as it is possible to fabricate near vertical walls with it and to vary the thickness of films over a large range of 1-200μm. As shown in Figure A.11, piranha-cleaned silicon wafers were coated with SU-8 using a spin-coater (Headway Research Inc.). The coating speed and durations were varied to get desired thicknesses. The resist was soft-baked before patterning it using a mask aligner (Karl SUSS-MJB4). After exposure, the hard bake was done at 65°C for 1 min and at 95°C for 9 min to further cross-link SU-8. The baked pattern was then developed to obtain the final rough surface. It is also possible to make a negative mold using SU-8 patterning and use it to form pillars with a softer material like PDMS which can help in assessing the variation in adhesion with surface hardness. SEM images of some of the micron-sized SU-8 patterns are shown in Figure A.12. Figure A.13 shows the SEM images of SU-8 mold and of the PDMS pillars obtained through these molds.

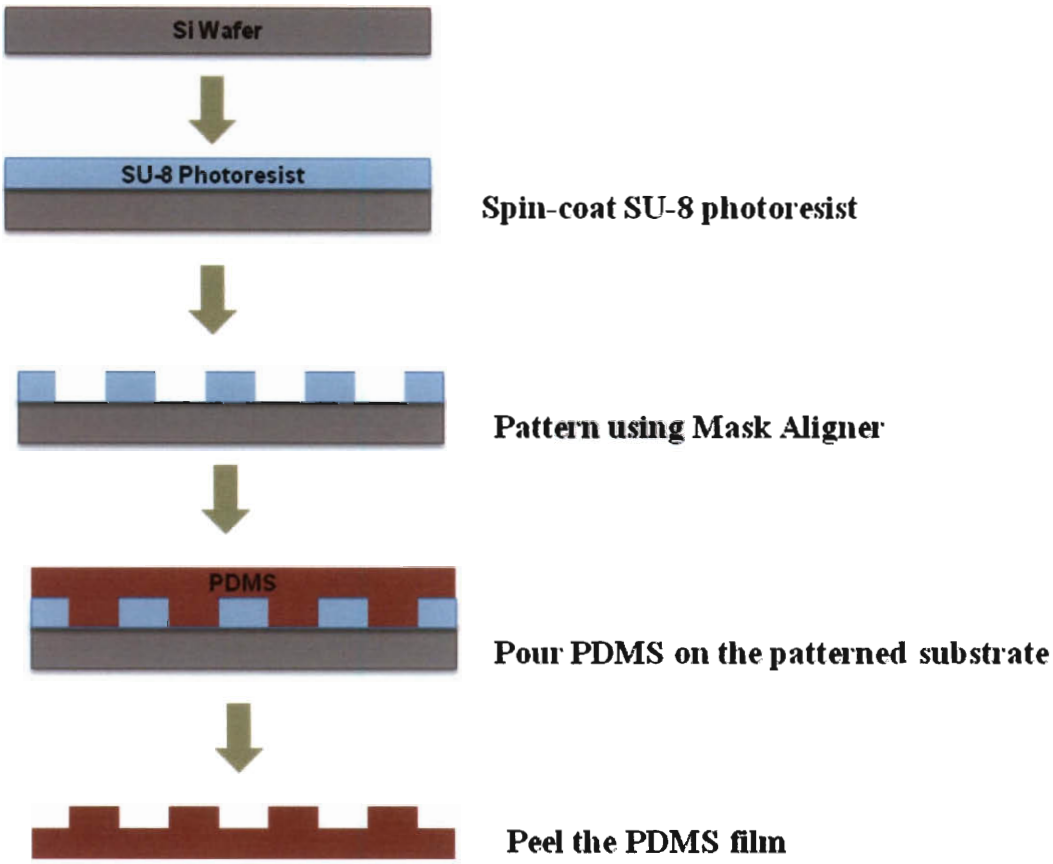

Figure A.11 Schematic of the soft-lithography process used for fabricating SU-8 and PDMS pillars

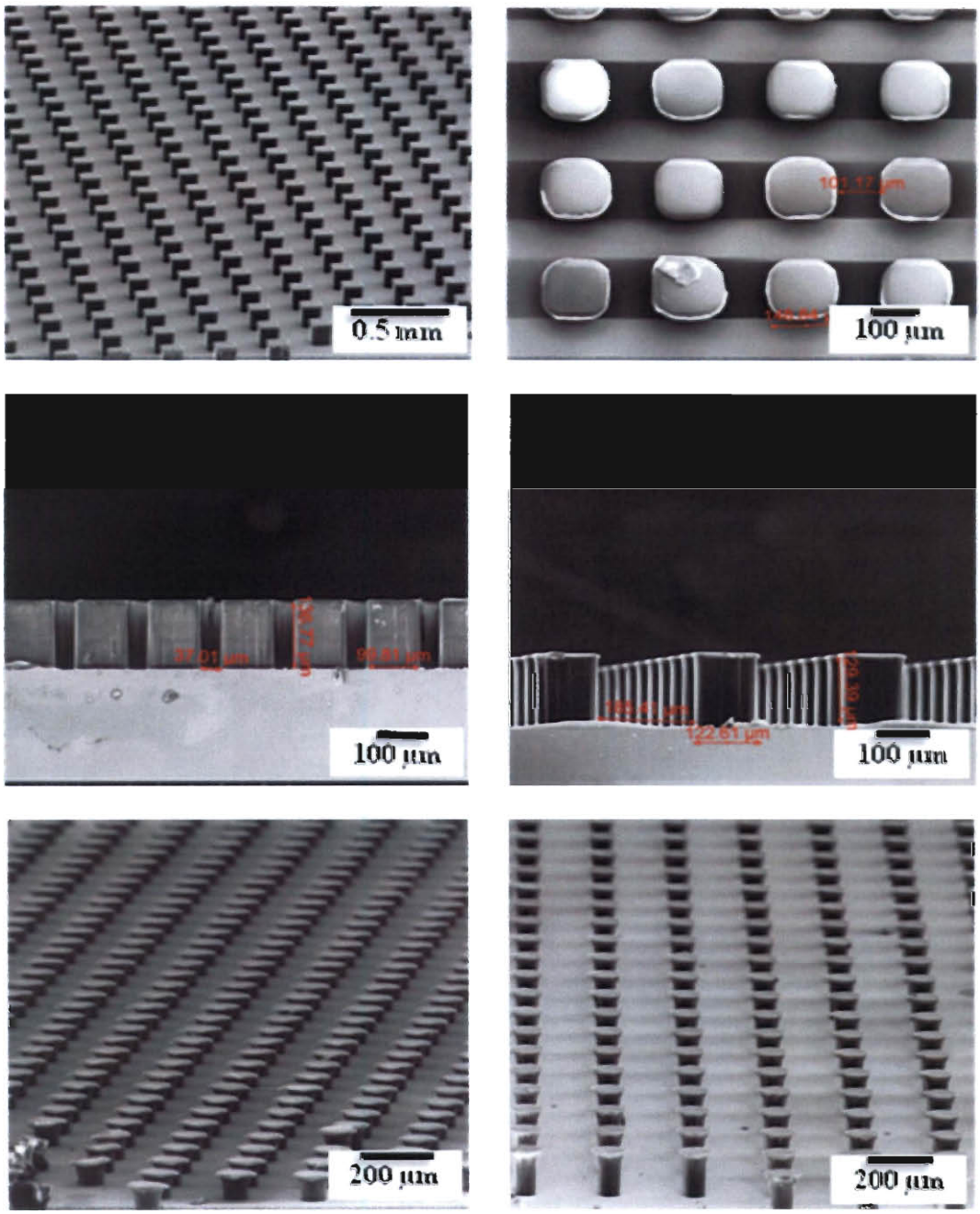

Figure A.12 SEM images of SU-8 pillars formed using soft-lithography. Pillars with different shapes and sizes were fabricated to vary the degree of roughness.

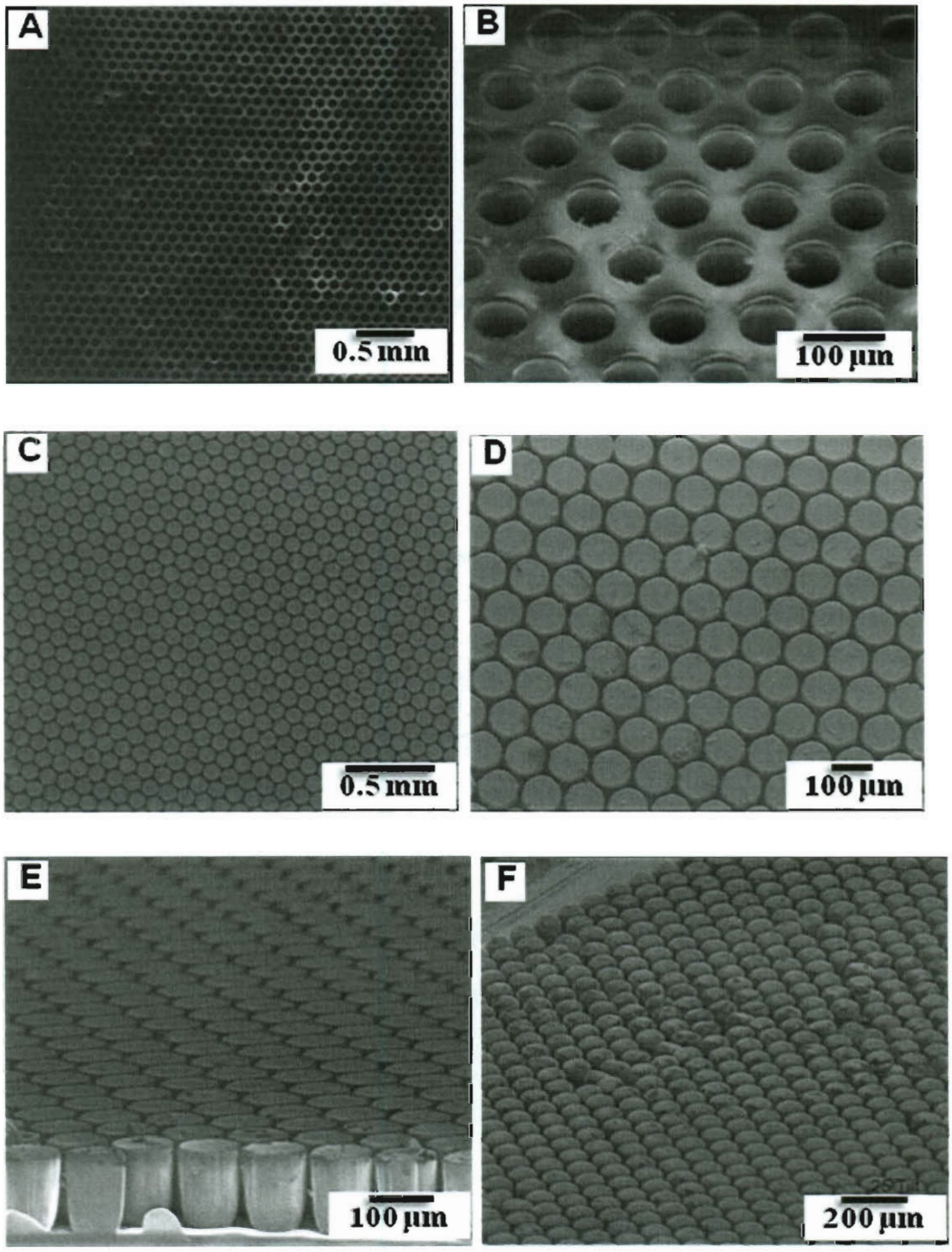

Figure A.13 SEM images of (A) and (B) SU-8 molds. (C) and (D) Top view of PDMS pillars fabricated using these molds. (C) Side view and (D) Tilted view of pillars

Using an in-house built compression device, un-patterned CNTs were pressed against the SU-8 pillars and were then imaged under SEM (Figure A.14). Preliminary results show a significant uniform buckling at the interface where CNTs come in contact with the pillars. The well-defined folds are restricted to the top part of the CNTs. Further studies are needed to examine the onset of buckling and how it progresses with increasing pressure. Detailed force measurements are required to understand how the adhesion varies with various parameters such as pillar length, diameter and spacing. This would extend the understanding of adhesion on rough surfaces and would help in designing the synthetic adhesive suited for varying surface roughness.

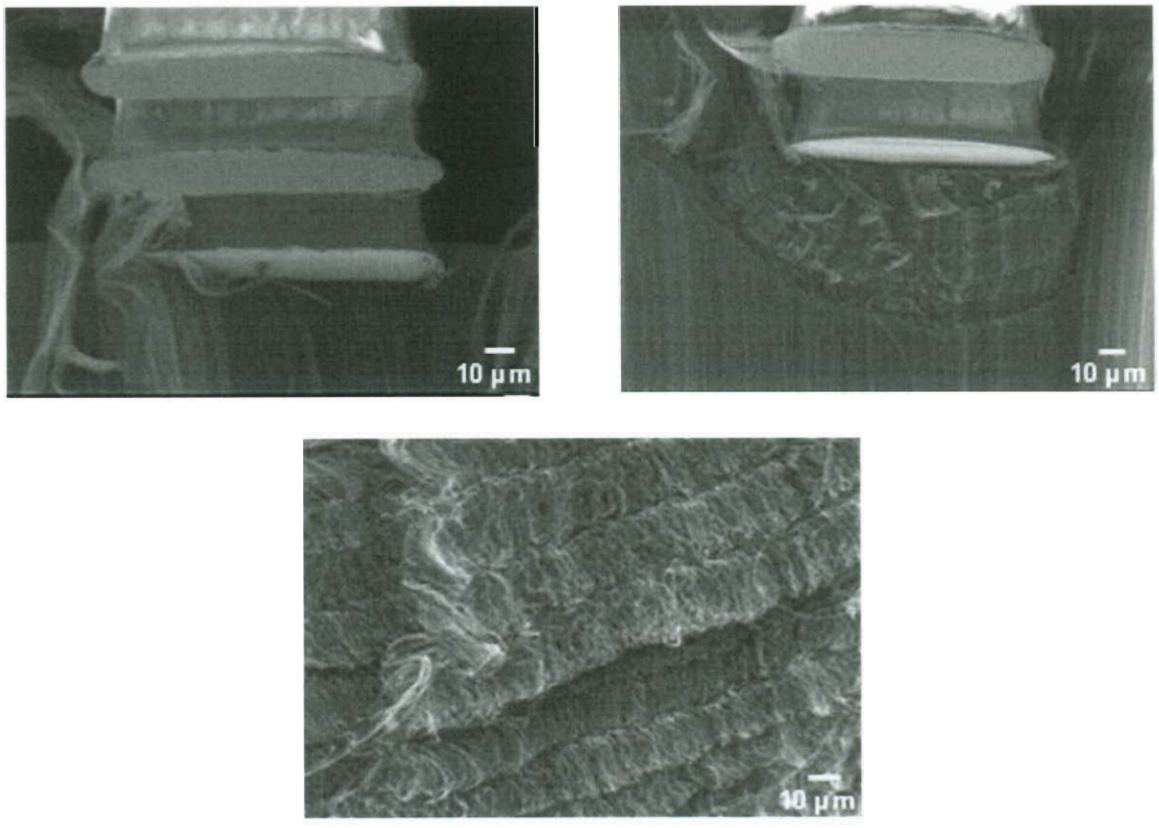

Figure A.14 SEM images showing the progressive compression of CNTs against SU-8 pillars. The top CNTs near the contact area start buckling under compression.

References

1. Autumn, K.; Hsieh, S. T.; Dudek, D. M.; Chen, J.; Chitaphan, C.; Full, R. J., Dynamics of geckos running vertically. *Journal of Experimental Biology* **2006,** 209, (2), 260-272.

2. Arzt, E., Biological and artificial attachment devices: Lessons for materials scientists from flies and geckos. *Materials Science & Engineering C-Biomimetic and Supramolecular Systems* **2006,** 26, (8), 1245-1250.

3. Geim, A. K.; Dubonos, S. V.; Grigorieva, I. V.; Novoselov, K. S.; Zhukov, A. A.; Shapoval, S. Y., Microfabricated adhesive mimicking gecko foot-hair. *Nature Materials* **2003,** 2, (7), 461-463.

4. Sitti, M.; Fearing, R. S., Synthetic gecko foot-hair micro/nano-structures as dry adhesives. *Journal of Adhesion Science and Technology* **2003,** 17, (8), 1055-1073.

5. Lee, H.; Lee, B. P.; Messersmith, P. B., A reversible wet/dry adhesive inspired by mussels and geckos. *Nature* **2007,** 448, (7151), 338-U4.

6. Northen, M. T.; Turner, K. L., A batch fabricated biomimetic dry adhesive. *Nanotechnology* **2005,** 16, (8), 1159-1166.

7. Hansen, W. R.; Autumn, K., Evidence for self-cleaning in gecko setae. *Proceedings of the National Academy of Sciences of the United States of America* **2005,** 102, (2), 385-389.

8. Irschick, D. J.; Austin, C. C.; Petren, K.; Fisher, R. N.; Losos, J. B.; Ellers, O., A comparative analysis of clinging ability among pad-bearing lizards. *Biological Journal of the Linnean Society* **1996,** 59, (1), 21-35.

9. Arzt, E.; Gorb, S.; Spolenak, R., From micro to nano contacts in biological

attachment devices. *Proceedings of the National Academy of Sciences of the United States of America* **2003,** 100, (19), 10603-10606.

10. Ruibal, R.; Ernst, V., Structure of digital setae of lizards. *Journal of Morphology* **1965,** 117, (3), 271-93

11. Williams, E. E.; Peterson, J. A., Convergent and alternative designs in the digital adhesive pads of scincid lizards. *Science* **1982,** 215, (4539), 1509-1511.

12. Autumn, K.; Sitti, M.; Liang, Y. C. A.; Peattie, A. M.; Hansen, W. R.; Sponberg, S.; Kenny, T. W.; Fearing, R.; Israelachvili, J. N.; Full, R. J., Evidence for van der waals adhesion in gecko setae. *Proceedings of the National Academy of Sciences of the United States of America* **2002,** 99, (19), 12252-12256.

13. Huber, G.; Mantz, H.; Spolenak, R.; Mecke, K.; Jacobs, K.; Gorb, S. N.; Arzt, E., Evidence for capillarity contributions to gecko adhesion from single spatula nanomechanical measurements. *Proceedings of the National Academy of Sciences of the United States of America* **2005,** 102, (45), 16293-16296.

14. Niewiarowski, P. H.; Lopez, S.; Ge, L.; Hagan, E.; Dhinojwala, A., Sticky gecko feet: The role of temperature and humidity. *PLoS One* **2008,** 3, (5), 7.

15. Autumn, K.; Liang, Y. A.; Hsieh, S. T.; Zesch, W.; Chan, W. P.; Kenny, T. W.; Fearing, R.; Full, R. J., Adhesive force of a single gecko foot-hair. *Nature* **2000,** 405, (6787), 681-685.

16. Autumn, K.; Gravish, N.; Wilkinson, M.; Santos, D.; Spenko, M.; Cutsosky, M., Frictional adhesion of natural and synthetic gecko setal arrays. *Integrative and Comparative Biology* **2006,** 46, E5-E5.

17. Chan, E. P.; Greiner, C.; Arzt, E.; Crosby, A. J., Designing model systems for enhanced adhesion. *Mrs Bulletin* **2007,** 32, (6), 496-503.

18. Kamperman, M.; Kroner, E.; del Campo, A.; McMeeking, R. M.; Arzt, E., Functional adhesive surfaces with "Gecko" Effect: The concept of contact splitting. *Advanced Engineering Materials* 12, (5), 335-348.

19. Kaelble, D. H., Theory and analysis of peel adhesion - bond stresses and distributions. *Transactions of the Society of Rheology* **1960,** 4, 45-73.

20. Creton, C.; Gorb, S., Sticky feet: From animals to materials. *Mrs Bulletin* **2007,** 32, (6), 466-472.

21. Spolenak, R.; Gorb, S.; Gao, H. J.; Arzt, E., Effects of contact shape on the scaling of biological attachments. *Proceedings of the Royal Society of London Series a-Mathematical Physical and Engineering Sciences* **2005,** 461, (2054), 305-319.

22. Aksak, B.; Murphy, M. P.; Sitti, M., Adhesion of biologically inspired vertical and angled polymer microfiber arrays. *Langmuir* **2007,** 23, (6), 3322-3332.

23. Jin, M. H.; Feng, X. J.; Feng, L.; Sun, T. L.; Zhai, J.; Li, T. J.; Jiang, L., Superhydrophobic aligned polystyrene nanotube films with high adhesive force. *Advanced Materials* **2005,** 17, (16), 1977-1981

24. Kim, S.; Sitti, M., Biologically inspired polymer microfibers with spatulate tips as repeatable fibrillar adhesives. *Applied Physics Letters* **2006,** 89, (26).

25. Ge, L.; Sethi, S.; Ci, L.; Ajayan, P. M.; Dhinojwala, A., Carbon nanotube-based synthetic gecko tapes. *Proceedings of the National Academy of Sciences of the United States of America* **2007,** 104, (26), 10792-10795.

26. Sethi, S.; Ge, L.; Ci, L.; Ajayan, P. M.; Dhinojwala, A., Gecko-inspired carbon nanotube-based self-cleaning adhesives. *Nano Letters* **2008,** 8, (3), 822-825.

27. Yurdumakan, B.; Raravikar, N. R.; Ajayan, P. M.; Dhinojwala, A., Synthetic gecko foot-hairs from multiwalled carbon nanotubes. *Chemical Communications* **2005**, (30), 3799-3801.

28. Maeno, Y.; Nakayama, Y., Geckolike high shear strength by carbon nanotube fiber adhesives. *Applied Physics Letters* **2009,** 94, (1).

29. Maeno, Y.; Ishikawa, A.; Nakayama, Y., Adhesive behavior of single carbon nanotubes. *Applied Physics Express* 3, (6).

30. Treacy, M. M. J.; Ebbesen, T. W.; Gibson, J. M., Exceptionally high young's modulus observed for individual carbon nanotubes. *Nature* **1996,** 381, (6584), 678-680.

31. Ci, L. J.; Manikoth, S. M.; Li, X. S.; Vajtai, R.; Ajayan, P. M., Ultrathick freestanding aligned carbon nanotube films. *Advanced Materials* **2007,** 19, 3300-3303.

32. Xia, Y. N.; Whitesides, G. M., Soft lithography. *Angewandte Chemie-International Edition* **1998,** 37, (5), 551-575.

Appendix B

List of Patent and Publications

PATENT: Ajayan PM, **Goyal A**, Kumar A, *Synthesis of Metal and Metal Alloy Nanoparticle Embedded Siloxane Composites*. US 2010/0120942

1. *Metal Salt Induced Synthesis of Hybrid Metal Core-Siloxane Shell Nanoparticles and Siloxane Nanowires*. Chemical Communications, **46**, 964 (2010)
   Goyal A, Kumar A, Ajayan PM

2. *In-situ Synthesis of Metal Nanoparticle Embedded Free Standing Multifunctional Polydimethylsiloxane Films.* Macromolecular Rapid Communications 30, 1116, (2009) de
   Goyal A, Kumar A, Patra P, Mahendra S, Alvarez PJJ, John G, Ajayan PM

3. *Electrical Properties of C_{60} Micro-rods Prepared by Solvent Precipitation Method*
   Journal of Applied Physics 103, 064903 (2008)
   Goyal A, Kumar A, Kar S, Soldano C, Ajayan PM

4. *Spontaneous Dissolution of Ultralong Single and Multiwalled Carbon Nanotubes*
   ACS Nano, 4, 3969 (2010)
   Parra Vesquez ANG, Behabtu N, Green MJ, Pint CL, Young CC, Schmidt J, Kesselman E, **Goyal A**, Ajayan PM, Cohen Y, Talmon Y, Hauge RH, Pasquali M

5. *Adhesion and Frictional Forces of Gecko-Inspired Caron-Nanotube Array.* (accepted Nanoletters)
   Ge L, Ci L, **Goyal A**, Shi R, Ajayan PM, Dhinojwala A

6. *In-situ Synthesis of Catalytic Metal Nanoparticle-PDMS Membranes by Thermal Decomposition Process*. (submitted)
   Goyal A, Mohl M, Kumar A, Puskas R, Kukovecz A, Konya Z, Kiricsi I, Ajayan PM

7. *Flexible CNT-Cu_2O hybrid electrodes for Li-ion batteries.* (submitted)
   Goyal A, Reddy ALM, Ajayan PM